Problems at the Nexus of Geometry and Soft Matter: Rings, Ribbons and Shells

Thesis advisor

L. Mahadevan

Author

Ee Hou Yong

Problems at the Nexus of Geometry and Soft Matter: Rings, Ribbons and Shells

Abstract

There has been an increasing appreciation of the role in which elasticity plays in soft matter. The understanding of many shapes and conformations of complex systems during equilibrium or non-equilibrium processes, ranging from the macroscopic to the microscopic, can be explained to a large extend by the theory of elasticity. We are motivated by older studies on how topology and shape couple in different novel systems and in this thesis, we present novel systems and tools for gaining fundamental insights into the wonderful world of geometry and soft matter.

We first look at how defects, topology and geometry come together in the physics of thin membranes. Topological constraint plays a fundamental role on the morphology of crumpling membranes of genus zero and suggest how different fundamental shapes, such as platonic solids, can arise through a crumpling process. We present a way of classifying disclinations using a generalized "Casper-Klug" coordination number. We show that there exist symmetry breaking during the crumpling process, which can be described using Landau theory and that thin membranes preserve the memory of their defects.

Next we consider the problem of the shapes of Bacillus spores and show how one can understand the folding patterns seen in bacterial coats by looking at the simplified

problem of two concentric rings connected via springs. We show that when the two rings loses contact, rucks spontaneous formed leading to the complex folding patterns. We also develop a simple system of an extensible elastic on a spring support to study bifurcation in system that has adhesion. We explain the bifurcation diagram and show how it differs from the classical results.

Lastly, we investigate the statistical mechanics of the Sadowsky ribbon in a similar spirit to the famous Kratky-Porod model. We present a detail theoretical and numerical calculations of the Sadowsky ribbon under the effect of external force and torsion. This model may be able to explain new and novel biopolymers ranging from actin, microtubules to rod-like viruses that lies outside the scope of WLC model. This concludes the thesis.

Contents

List of Figures

List of Tables

Citations to Previously Published Work

Manuscript based on first part of Chapter 3 is in the process of submission. Manuscripts based on Chapters 2, second part of Chapter 3 and 4 are in preparation for submission.

Acknowledgments

I would like to begin by thanking my advisor Prof. L. Mahadevan for making my graduate school years such a great experience through his support, encouragement and numerous ingenious ideas for which I will always be very grateful. Maha is literally a walking Wikipedia with his wonderful grasp in so many fields of research, ranging from hydrodynamics, geometry and elasticity, cellular and developmental physiology, macromolecular assemblies to probability. Coupled with his great physical intuitions, his passion in science and ability to elucidate complicated ideas, I have learnt a great deal of Physics from him. He is also very good at knowing when to give me a little push in the forward direction when I needed it.

Completing this doctoral work has been a wonderful and often overwhelming experience. I remember seeing a poster when I first enter graduate showing two cartoons. The first cartoon shows a young (and impressionable) incoming graduate student staring at a chart that denotes his knowledge of the world. On the chart is an area of a certain size, half of it is labelled as "known" and the other half as "unknown". The second cartoon is the same graduate student (perhaps wiser) after getting his Ph.D staring at the "revised" chart. The area of "known" knowledge has grown somewhat larger in this new chart. However, the area of "unknown" knowledge has literally growth exponentially and has outgrown the chart in size. In many sense, this picture reflects the humbling experience of my graduate studies.

All members of the Maha group were instrumental in creating a condusive intellectual and social atmosphere. The ability to bounce ideas off so many excellent minds has been priceless. My most intense collaboration has been with Luca Giomi, who introduced me to the world of twisted ribbons. Special thanks go to Zhiyan

Wei for always being so fun to talk to on both physics and non-physics matters as well as the fun we had together on our numerous food excursions. My time in the office would certainly be much more boring if not for my other officemates Paolo Paoletti, Anja Slim and John Kolinski. It was a pleasure interacting with all the other past and present members of the Maha group, including Mahesh Bandi, Haiyi Liang, Sharon Gerbode, Gareth Wyn Jones, Greg Morrison, Andrew McCormick, Aryesh Mukherjee, Mark Henle and Shreyas Mandre.

There are countless others who have been there for me throughout my time as a graduate student. I would like to thank Prof. David Nelson, whose clarity and brilliance in Physics has been a great source of inspiration. I would also to thank my undergraduate adviser Prof. Michael Peskin, who has given me valuable advice and encouragements along the way. I thank Prof. Vinothan Manoharan for always being there to answer my questions. I thank Dr. Ozgur Sahin for showing to me the many wonderful uses of bacteria spores and the AFM. I would also like to thank Prof. Prof. Howard Stone and all his group members for exposing me to the fascinating world of fluid dynamics. I also thank everyone else at Harvard whom I had a chance to cross paths with including Subir Sachdev, Tim Kaxiras, Mikhail Lukin, Eugene Demler, Rudro Biswas, Yang Qi, Timur Gatanov, Daniyar Nurgaliev, Kirill Korolev, Pavel Petrov, Yevgeny Kats, Amy Peng, Jonathon Gillen, Haruka Tanji, Sheng Meng, Weili Wang and Maria Fyta. Special thanks go to Maha's secretary Marina Di Donato-McLaughlin for being so helpful; to William Walker who has been very helpful when processing financial matters and to Sheila Ferguson for being always there to answer my numerous questions.

Finally, and most importantly, I would like to thank my parents, my brother, my sister and my wife for their limitless support and unconditioned love. This thesis is dedicated to you.

Dedicated to my father Hua Chew Yong,
my mother Wah Eng Chua,
my brother Alan Ee Fei Yong
my sister Hui Ching Yong
and my wife Shih Ying Yao.

Chapter 1

Introduction, Motivation, and Outline

If I were to convey the main message of the thesis to a non-expert reader, I would say that it is about understanding the geometry of crumpled membranes, the buckling of rings and the twisting of ribbons. Looking up the English-language dictionary, I find that:

Crumple *crush (something, typically paper or cloth) so that it becomes creased and wrinkled,*

Buckle *bend and give way under pressure or strain,*

Twist *form into a bent, curling, or distorted shape,*

and surprisingly, the basic ideas of the physics are explained in these three words. Of course, there is much more richness in this three systems that I will present, which I hope is conveyed in clear manner in this thesis.

Let us start with a reminder of the basic physics of deformation of a thin, isotropic, homogeneous, naturally flat sheet. In the long-wavelength limit, the sheet has two primary modes of deformation: an out-of-plane bending and an in-plane stretching. Bending deformations produce strains of order z at a distance z along the normal to the middle surface. The elastic energy of pure bending is then $U_B \sim \int dz\, z^2 \sim h^3$. On the other hand, stretching of the middle surface produces homogeneous strains through the cross-section, so that $U_S \sim h$. The total energy may be written in a cavalier manner as

$$\text{energy} = h^3(\text{bending}) + h(\text{stretching}).$$

Indeed, as Rayleigh and others observed more than 100 years ago,

> *...thickness is diminished without limit, the actual displacement will be one of pure bending, if such there be, consistent with the given conditions*

Such bending/buckling in thin elastic shell membranes are ubiquitous in nature, in both physical and biological systems, over a wide length scale. We can observe it in viruses (10-100nm), where the icosahedral packings of protein capsomeres proposed by Caspar and Klug for spherical viruses become unstable to faceting for sufficiently large virus size, in analogy with the buckling instability of disclinations in two-dimensional crystals [55, 109, 93]; vesicles (1μm) take on various shape under osmotic pressure difference by tuning the excess area [112, 78]; microspheres (1μm) show buckling due to dissolution of the core in the external medium [116, 117, 81], pollen grain (10-100μm) is able to fold onto itself to prevent excess desiccation due to presence of axially elongated apertures of high compliance [47]; armored bubble (10-100μm) can form faceted polyhedral shapes that are stable to dissolution [1]; buckling in

droplets due to drying (1mm) [99]; wrinkling in skin/apple (10cm) [18]; phyllotaxis in plants (10cm) arise from a cooperation and competition between mechanical and biochemical processes [76, 91] to name a few (See Fig. 1.1).

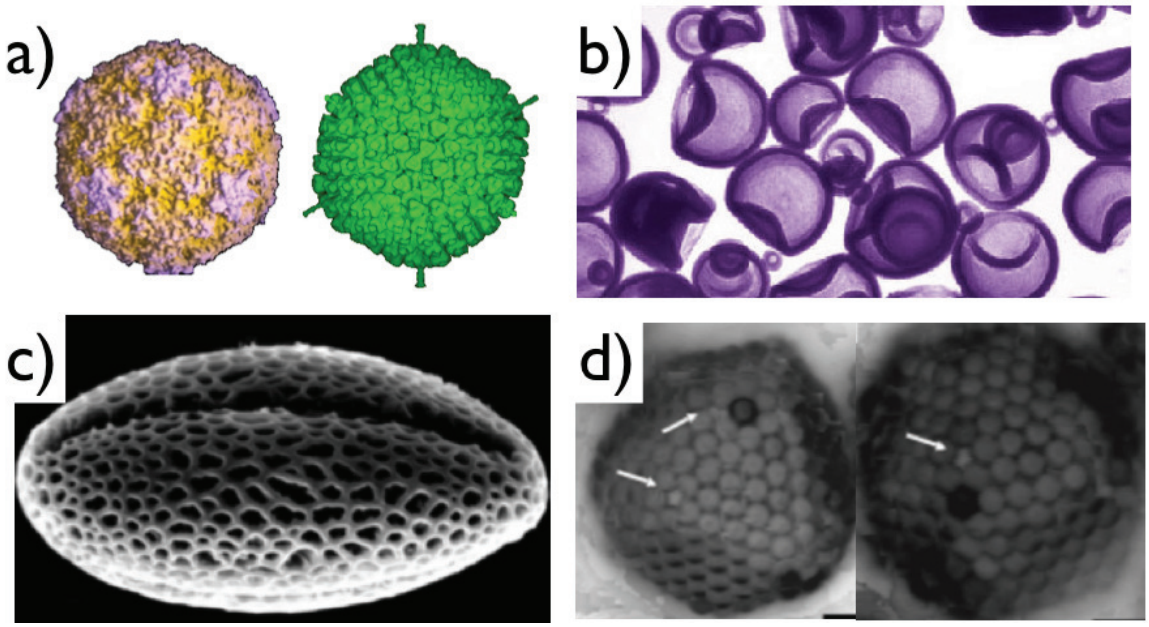

Figure 1.1: Crumpling occurs on a wide range of length scale (a) The rhinovirus (left) and the larger adenovirus (right) both exhibits icosahedral symmetry. (b) Block copolymer vesicles in solution. (c) Folding of a pollen grain. (d) Faceted shape of armored bubbles. White arrows indicate missing particle defects at the vertices of the bubble. The four images are taken from Ref. [84, 114, 47, 1] respectively.

Amazingly, continuum elastic theory works in all these length scale, a wonderful feat for a theory and we can use the theory to describe the shape of the membrane. Due to the nonlinearity of elasticity theory, they are essentially impossible to solve in analytical form except in some one-dimensional cases, so that one has to resort to either computations or a semianalytical approach using scaling and asymptotic arguments to make progress. As my adviser, Maha noted:

> *The contrast is self-evident in an experiment that is the result of many a failed calculation: how easy it is to crumple a piece of paper, and yet how hard it is to understand it!*

As we go from 2D membranes to 1D strings/rods/ribbons, we will discuss bending and twisting but the basic idea behind the physics remains the same. Namely, that 1D systems tend to reduce its curvature and torsional stress and will take on conformations that reduce its elastic energy.

1.1 Outline of Thesis

This thesis discusses three problems in soft matter physics:

1. Crumpling morphologies of crystalline shells with frozen defects (Chapter 2),
2. Buckled rings and its relations to bacterial spore (Chapter 3),
3. Statistical Mechanics of twisted ribbons (Chapter 4).

These topics represent disparate physical systems and require different toolkits of theory and computer simulation to understand them. However, they can all be understood in the context of elasticity theory as will become clear later in this thesis. The first part contains the most interesting simulations and I have spent the most time on it. All the chapters are self-contained and can be read independently.

1.2 Role of defects in the crumpling of crystalline shell

Continuum elasticity works until we go to small enough length scales, where crystallinity matters, and the role of topological defects become important [90, 55, 70] and we have to resort to discrete elasticity theory. Here, let us digress briefly to discuss about the armored bubbles experiment [1]. These fascinating objects can adopt stable faceted shapes as gas dissolves into the surrounding liquid. It is reported that the colloids tend to have six-fold sites and the five-fold disclination site is often unoccupied by a particle. This observation, is a manifestation of topological defects played out on a microscopic scale (10-100μm). These armored bubbles shapes are part of a continuous transition as a function of the ratio of the particle (radius a) to bubble radius (radius R) from clusters ($a/R \approx 1$), to facets ($a/R \approx 0.1$), to crumpled shapes ($a/R \ll 0.1$) [1] and this dimensionless parameter is analogous to ratio of bond length to size of system if one were to think about crystalline systems.

On a spherical surface of genus 0, it is known that crystalline structure (or equivalently, spring mass system) will exhibit a minimum of twelve five-fold disclinations and this number of topological defect is often expressed as:

$$N_5 - N_7 = 12,$$

where N_5 refers to the number of sites (or particles) with coordination number 5 and similarly for N_7. This is the well know *geometrical frustration* that is a consequence of the more general Euler-Poincaré formula, given by $\chi_E = V - E + F$, where χ_E is the Euler characteristic and F, E, V are the number of faces, edges and vertices

in a covering respectively. Since we are forming a discrete surface that is closed, this means that it is in fact polyhedron and it is homeomorphic to the sphere. In particular, $\chi_E = 2(1-g) = 2$ for a polyhedron. When we triangulate the surface of a sphere, since there are exactly three vertices per face and two vertices per edge, we find that $3F = 2E$. Let N_z be the number of vertex with z-coordination number. Then $V = \sum_z N_z$ and $\sum_z zN_z = 2E$. Using these geometric relations, we find that

$$\sum_z (6-z)N_z = 6\chi_E = 12. \tag{1.1}$$

Thus we see that we can form higher order discrete surface surfaces that involves three-, four- and five-fold disclinations or combinations of them as long as they satisfy (1.1). We show that on surfaces where stocasticity is quenched, then the crumpling of a drying surface [99] is completely driven by the presence and locations of the disclinations. Depending on the set and locations of the disclinations, we can produce buckled shapes that look like Platonic solids, Archimedean solids and so on. It is rather amazing how the symmetry of the discrete surface manifest itself outwardly in its geometry as it crumple. We were able to map out a phase diagram of the morphology of the buckled shells based on two dimensionless parameters h/R an R/a, where R is the characteristic size of the surface, h is the thickness of the surface and a is the characteristic size of the bonds (or edges). As this is an elastic system, we expect there to exist a significant amount of hysteresis and we investigated the hysteresis loop in the Platonic shells and found that it exhibit a sharp first order transition. We were able to write down a simple Landau free energy that characterize the buckling transition that involves the rotationally invariant parameters Q_ℓ and W_ℓ.

1.3 Spores and buckled elastica

Bacillus spores are dormant cells that exhibit high resistance to environmental stresses. In spite of its dormancy, once nutrient is available the spore is able to resume metabolic activity and return to vegetative growth. The core of the bacteria spore is surrounded by a loosely cross linked peptidoglycan layer called the cortex, that is thought to maintain the dehydrated state of the core. The spore outermost protective layer, the coat, is a structurally complex multilayered protein shell, which protects the genetic material while permitting the diffusion of water and small molecules to the spore interior and is largely responsible for the resilience of the spore. Spore can dynamically expand and contract in response to humidity and the coat can exhibit complex wrinkling patterns during dehydration. Rucks or wrinkles did not unfold completely even at very high relative humidity, suggesting that the coat does not limit cortex swelling.

$$U = U_{\text{bending}} + U_{\text{stretching}} + U_{\text{shear}} + U_{\text{spring}}$$

We generated a mechanical model predicting the emergence and dynamics of the coat folding patterns in Bacillus subtilis spores. We believe that the emergent properties of the assembled coat, such as its elastic modulus and thickness, rather than specific individual molecular components, are responsible for coat flexibility. From this viewpoint, a functional coat can be built in a large number of ways and with diverse protein components. Such freedom in design parameters could facilitate evolutionary adaptation (particularly with respect to material properties) and the emergence of the wide range of molecular compositions found among Bacillus spore coats.

We wrote down the simplest mathematical model that describe our mathematical model, namely, an compressible elastic connected to a bed of springs and under applied load at the ends. The force and torque balance lead to two equations which can be reduced to one scalar equation using the reduction method of Liapunov-Schmidt. The phase space of normalized pressure vs normalized load of this system has very rich features and there are multiple buckling modes along different branches. The buckling can be supercritical or subcritical depending on the values of the parameters.

1.4 Chapter 4: Statistical Mechanics of Twisted Ribbons

The physics of a "1-dimensional" object is very different as compared to a 2-dimensional shell. In 1D chains, there is one length scale that describe most of the physics, namely the length of the chain. The elastic energy term comes from the bending, stretching and twisting of this midline. We can describe the deformation of a segment of the chain by

stretch: $u(s)$, the extensional deformation, measures the fractional change in the length of a segment ds. $u = \Delta(ds)/ds$.

bend: κ (curvature) measures how the chain unit tangent vector changes as we move along the arc length.

Twist: ω measures how each succeeding elect has been rotated about the chain's axis relative to its neighbor. For example, if the segment is straight but twist

at its end by a relative angle $d\phi$, then $\omega = d\phi/ds$.

All these three quantities are local but they can be related to the overall deformation of the chain. A beam that is initially straight can deviate from this geometry by applying force and torque to it. Of course, most slender chains are not straight naturally due to entropic reasons (mainly). The chain adopts a random-coil conformation because there is one way to be straight but many more ways to be coiled up. Such 1D chains has been used to describe many systems in nature, most notably the DNA, which can be described very satisfactorily using the phenomenological worm-like chain model. In this model, we keep the bending and torsion but assume that the chain is inextensible.

Recently, there have been some work on studying the Sadowsky ribbon, which is very much like the wormlike chain model in spirit but there exist nonlinear coupling between the curvature and torsion term. This nontrivial coupling make the ribbon a very interesting model to study since it has many interesting physics waiting to be explored. A wormlike chain has tangent-tangent correlation function that decays exponentially. On the other hand, the Sadowsky ribbon has both tangent-tangent and binormal-binormal correlation function to worry about. The binormal-binormal correlation function falls off exponentially while the tangent-tangent has an oscillatory exponential decay that signifies the presence of an underlying helical structure that persists at any finite temperature. Using MC methods, we found the force extension curve of the Sadowsky with and without applied torque and found it to be to be much stiffener compared to the WLC in both cases. At low force and no applied torque, the effective diffusion constant of the Sadowsky ribbon is much stiffer than WLC and this is stems from the tangent-tangent persistence length of the Sadowsky ribbon. The

force-extension curve for the ribbon under different applied torque is very interesting. At small forces, the ribbon tend to stay as an entangled coil but beyond a critical force, it starts to extend sharply, analogous to a first order transition.

Chapter 2

Buckling morphologies of crystalline shells with frozen defects

2.1 Introduction

Imagine a thin spherical shell membrane of thickness h and radius R initially filled with some fluid. As the fluid is removed from the interior of the shell, the membrane will start to crumple and form rich and interesting faceted structure. As the shell deform, it will find a balance between the bending energy and strain energy that results in the lowest energy configuration. The elastic energy stored in a deformed thin shell can be subdivided into two contributions, one from the bending deformation, which is achieved by changing the curvature of the surface, and one from the in-plane stretching. The bending modulus κ scales as the third power of the shell thickness

h while the in-plane stretching modulus Y scales linearly with h. Therefore, if R is the characteristic size of the shell, as the ratio h/R approaches zero, stretching deformations become increasingly costly compared to bending deformations. For a given load, the thin shell will primarily respond by bending rather than stretching. However, in closed shells such as a soccer ball, pure bending is not possible without some stretching. Since stretching is energetically prohibitive, the deformed shape will mostly be an inextensional deformation of the original shape, with stretching being concentrated at ridges, resulting in a faceted structure. This tendency to form faceted structure is due to energy focusing [110] where the elastic energy, which is initially smoothly distributed, becomes more and more non-uniform, with high energy concentrated in the bent regions. This energy focusing becomes more prominent on membranes with thinner shells and the buckling behavior of the shell can be characterized by a dimensionless parameter h/R (or equivalently the Foppl-von Karman number $\gamma \sim (R/h)^2$ [55, 109]).

Such bending/buckling in thin elastic shell membranes are ubiquitous in nature, in both physical and biological systems, over a wide length scale. We can observe it in viruses (10-100nm), where the icosahedral packings of protein capsomeres proposed by Caspar and Klug for spherical viruses become unstable to faceting for sufficiently large virus size, in analogy with the buckling instability of disclinations in two-dimensional crystals [55, 109, 93]; vesicles (1μm) take on various shape under osmotic pressure difference by tuning the excess area [112, 78]; microspheres (1μm) show buckling due to dissolution of the core in the external medium [116, 117, 81], pollen grain (10-100μm) is able to fold onto itself to prevent excess desiccation due to presence

of axially elongated apertures of high compliance [47]; armored bubble (10-100μm) can form faceted polyhedral shapes that are stable to dissolution [1]; buckling in droplets due to drying (1mm) [99]; wrinkling in skin/apple (10cm) [18]; phyllotaxis in plants (10cm) arise from a cooperation and competition between mechanical and biochemical processes [76, 91] to name a few.

The theory of thin shell is highly non-linear and for the most cases, requires numerical solutions to extract meaningful information. One of the key ingredient is the discretization of the surface of the continuous crumpled membrane into a set triangulated subregion. A flat two-dimensional surfaces can be triangulated into a lattice of equally sized equilateral triangles, with each lattice site (or vertex) having a coordination number of six, e.g. honeycomb lattice. However, such perfect triangulation is impossible on a curve manifold with nonzero Gaussian curvature such as a sphere. This is the well know *geometrical frustration* that is a consequence of Euler-Poincaré formula, given by

$$\chi_E = V - E + F,$$

where χ_E is the Euler characteristic and F, E, V are the number of faces, edges and vertices in a covering respectively. In particular, $\chi_E = 2(1-g) = 2$ for a sphere (genus zero). When we triangulate the surface of a sphere, since there are exactly three vertices per face and two vertices per edge, we find that $3F = 2E$. Let N_z be the number of vertex with z-coordination number. Then $V = \sum_z N_z$ and $\sum_z zN_z = 2E$. Using these geometric relations, we find that

$$\sum_z (6-z)N_z = 6\chi_E = 12. \tag{2.1}$$

Thus, Euler-Poincaré formula implies that it is impossible to have a triangulation

with only 6-fold coordinated sites and if we consider a covering of a sphere of radius R consisting of only 5-, 6- and 7-fold coordinated sites, there will be exactly twelve more 5-fold than 7-fold sites due to the topology of the sphere. A disclination is a lattice site with coordination other than six. In most numerical studies, the triangulated mesh is generated via a prescribed algorithm of subdivision and the resulting mesh is usually considered to be "random" and does not affect the final solution of the problem. In fact, there is a whole sub-community within the Finite Element field studying mesh implementation and adaptivity. Definitely, in the study of partial differential equations, the way the domain is discretized is a personal choice in solving the problem. However, in the field of elasticity, where the surface itself contains information about the local stress and strain, it is less obvious why mesh discretization does not matter, since the mesh is the problem itself.

It is only recently that such topological defects have been studied in depth [55, 109, 90, 10, 8, 7, 9, 51, 21] and each disclination has a "energy" associated with it known as the core energy [70]. Due to the long range character of such disclinations, it is argued that the lowest energy state is one where there are exactly twelve 5-fold sites in an otherwise 6-folded triangulation and these twelve defects are located on the vertices of an icosahedron inscribed in the sphere of radius R. Such 5-fold disclinations are responsible for the faceting of an otherwise spherical triangulation into an icosahedral-like structure [55]. There are two time scales in this problem, namely, (1) time scale of the defect dynamics (τ_{defect}), which is the characteristic time a defect takes to move over a certain length on the surface and (2) time scale of the surface dynamics ($\tau_{surface}$), which is the characteristic time the topography

of the surface changes appreciably. Most of the study of the physics of topological disinclinations has been done either in the regime where the time scale of the defect dynamics is much smaller than that of the deformation time scale of the ambient surface, i.e., $\tau_{defect}/\tau_{surface} \ll 1$, which we will refer to as the frozen topography limit or at the other end of the spectrum where the embedding surface is changing on a time scale that is small compared to the time scale of the defect dynamics, i.e., $\tau_{defect}/\tau_{surface} \gg$, which is the frozen defects limit. The immediate case where $\tau_{defect}/\tau_{surface} \sim 1$ has only been studied recently on spherical shells [51] and it is found that the spontaneous emergence of defect scars reduce elastic strain stress and delays the onset of the buckling transition.

For the case of frozen topography, the defects are allowed to move, interact with one another and proliferate on a surface with fixed geometry. The defects will move to regions of the surface that results in the least strain and the migration of defects do not influence the geometry (curvature) of the surface. This is analogous to the motion of small particles in a strong gravitational field where we can neglect the gravitational contribution of the particles to the original field. It has been found that when the number of topological defects become large, the disclinations may form more complicated structures (depending on what one assume for the core energy of a disclination) [10, 8, 7, 38] on the sphere. In the limit of small core energies and large R/a (R is the radius of sphere and a is the lattice spacing), it is energetically favorable for the disclinations to form one dimensional arrays of dislocations, which are tightly bound (5-7)-fold disclination pairs with one net excess 5-fold disclination, also known as grain boundary "scars" [10, 9, 71]. In the limit of large core energies,

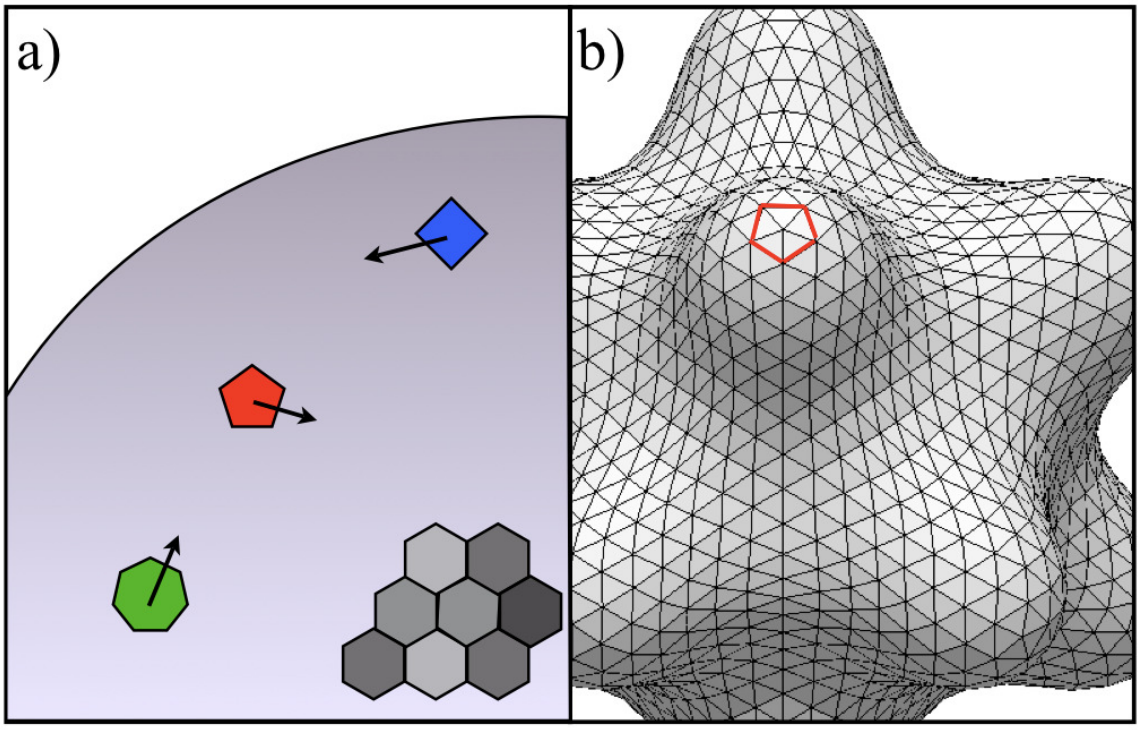

Figure 2.1: We illustrate here the difference between frozen topography and frozen defects. a) Frozen topography: There is one four-fold disclination (blue square), one five-fold disclination (red pentagon) and one seven-fold disclination (green heptagon) that are free to move on a spherical surface. These disclinations are embedded in a "sea" of 6-fold sites (grey hexagons). b) Frozen defects: The defects are frozen (fixed mesh) and the overall geometry (shape) of the surface can deform.

the creation of additional disclinations will be strongly penalized and the sphere will contain only the minimum allowed twelve 5-fold disclinations. The physics (in the zero temperature limit) is therefore characterized by the competition between the core energy cost of creating a topological defect and the compensating gain from the screening of Gaussian curvature when defects are allowed to proliferate.

For the case of frozen defects, we have a flexible membranes with crystalline order where the defects are frozen on the fluctuating surface. This is analogous to the motion of massive particles in general relativity where the curvature of the space is changing as the particles migrate in positions. It has been found that disclination plays an important role in the buckling of a flat membrane [90]. More recently, this methodology has been used to study the buckling of colloidal particles [81, 116, 117] and the folding of pollen grain [47]. In this paper, we look at the crumpling of spheres where the topological defects are frozen and see how the triangulation affect the shape of the deformed shell during shrinking. More precisely, we would like to know 1) How does the triangulation affects the morphology of a thin spherical shell that is shrinking with time and 2) How large must the mesh be until effects of the small number of disclinations is washed out? We consider the case where the core energies is large so it is energetically favorable to have the smallest set of topological defects. In particular, we created spheres that have defects associated with the Platonic solids and investigated the change in energy as the volume shrinks. The difference between frozen topography and frozen defects is shown in Fig. 2.1.

The organization of the paper is as follows. In Sec. 2.2, we present the mathematical model used in our numerical study. The different types of disclinations is

described in Sec. 2.3 and we study the crumpling process of spheres with different combinations of topological defects. The energy for the different spheres during the crumpling process is discussed in Sec. B.3, and we discussed about possible transition pathways among the different Platonic shells. The phase space as a function of the two dimensionless parameters containing all relevant length scales of the problem is discussed in Sec. 2.5. Sec. 2.6 contains a discussion of the classification of the spherical crystal lattice. We analyzed the shape of the crumpled spheres by looking at the spherical harmonic modes and calculated various rotationally invariant quantities in Sec. 2.7. In Sec. 2.8, we considered the effects of hysteresis for the different Platonic solids and show that there is a spontaneous breaking of the symmetry of the shell during the buckling phase and that the hysteresis loop display return point memory. In Sec. 2.9, we present a simple Landau free energy model that describe the symmetry breaking shape transition. We conclude in Sec. 2.10 our important results as well as a thought experiment that may be relevant to future studies.

2.2 Elastic Theory

The elastic energy E_T of a deformed shell may be regarded as the sum of bending and that due to stretching of the middle surface as follows [110, 54]:

$$\begin{aligned} H_T &= H_s + H_b \\ &= \int dA(E_s + E_b) \\ &= \frac{1}{2}\int dA(2\mu\gamma_{ij}^2 + \lambda\gamma_{kk}^2) + \frac{1}{2}\int dA(DH^2 + 2D_G K), \end{aligned} \tag{2.2}$$

where γ_{ij} is the strain tensor, μ and λ are the two-dimensional (2D) Lamé coefficients, D is the bending rigidity, D_G is the Gaussian rigidity, H and K are the mean and Gaussian curvatures respectively. If R_1 and R_2 are the principal radii of curvature, then $H = 1/R_1 + 1/R_2$ and $K = 1/R_1R_2$.

In order to understand the morphology of a crumpling thin shell, we use Surface Evolver [13] to simulate the deformation of the sphere under the constraint of a decreasing volume. Surface Evolver is an interactive program for the study of surfaces shaped by surface tension or other energies, and subject to various constraints. The total energy of a thin two-dimensional shell can be expressed as a sum of the stretching energy and the bending energy, i.e., $U_T = U_S + U_B$ [110, 54] and evolves toward minimal energy via a gradient or conjugate gradient descent method. For a closed surface with fixed topology, and when κ_G is a constant, the Gaussian curvature term integrates to a constant by the Gauss-Bonnet theorem and will henceforth be dropped, as it will have no influence on the morphology of the shell. Hence the bending energy only includes the contribution from the mean curvature. Thus in our numerics, we need only consider the elastic strain from the stretching of the shell and the bending energy from mean curvature.

The surface is implemented as a simplicial complex, that is a union of triangles, and each triangle (face) is uniquely defined by its three vertices $\mathbf{v}_1$, $\mathbf{v}_3$ and $\mathbf{v}_3$. Let $\mathbf{s}_1 = \mathbf{v}_2 - \mathbf{v}_1$ and $\mathbf{s}_2 = \mathbf{v}_3 - \mathbf{v}_1$ be the unstrained sides of the triangle, and construct column matrices $S = [\mathbf{s}_1, \mathbf{s}_2]$. When the surface is strained, the three vertices of each triangle is deformed from $\mathbf{v}_i$ to $\mathbf{v}'_i$. In a similar manner, let $\mathbf{r}_1 = \mathbf{v}'_2 - \mathbf{v}'_1$ and $\mathbf{r}_2 = \mathbf{v}'_3 - \mathbf{v}'_1$ be the strained sides and construct $R = [\mathbf{r}_1, \mathbf{r}_2]$. The deformation

gradient matrix D satisfies $DS = R$ and the Cauchy-Green strain matrix is given by $C = (D^T D - I)/2$, where I is the 2×2 identity matrix. Then the strain energy density is

$$\frac{Y}{2(1+\nu)}\left(Tr(C^2) + \frac{\nu}{(1-\nu)}(TrC)^2\right), \tag{2.3}$$

where $Y = Eh$ is the two-dimensional Young's modulus and ν is the Poisson ratio.

Each vertex v has a star of triangles around it of total area A_v. The force on each vertex v is

$$F_v = -\frac{\partial A_v}{\partial V}. \tag{2.4}$$

Since each triangle has 3 vertices, the area associated with v is $A_v/3$. Then the mean curvature is

$$h_v = \frac{F_v}{2(A_v/3)}. \tag{2.5}$$

The bending energy density is then

$$\kappa h_v^2 (A_v/3) = \kappa \frac{F_v^2}{4(A_v/3)}, \tag{2.6}$$

where $\kappa = Eh^3/12(1-\nu^2)$ is the bending rigidity. The ratio of bending rigidity to 2D Young's modulus κ/Y and the poisson ratio ν defines the thickness of the shell h, since

$$h^2 = 12(1-\nu^2)\frac{\kappa}{Y}. \tag{2.7}$$

Our model for the undeformed spherical shell has varying thickness h, initial volume $V_0 = 4\pi R^3/3 = 1$ (initial radius $R_0 = 0.62$) and spontaneous mean curvature equal to $c_0 = 1/R_0 = 1.61$. The Poisson ratio is determined to be $\nu = 1/3$ [90, 81] and the material is assumed to be isotropic with constant elastic moduli E. In our simulations, we vary the 2D Young's constant Y and fix $\kappa = 1$ so as to get a reasonable

range of h/R. Starting from a initial sphere, we then decrease the volume at a given constant rate δ until a final volume. For $\delta \ll 1$, the shell is evolving quasi-statically and is always at equilibrium. We control the volume and the pressure appear as a Lagrange multiplier. At each time step, Surface Evolver will evolve the surface toward the minimal energy by a gradient descent method. In order to create spheres with different topological defects, we first create a surface of our desired polyhedron in Surface Evolver. We turn off the bending and stretching energies and turn on the surface tension and let the surface evolve. For a fixed volume, the sphere is the solid with the smallest surface area. Hence this polyhedron will evolve to a sphere of volume V_0 since it is the minimal energy surface. The sphere hence created will have the defects associated with the original polyhedron. Then we turn on the bending and stretching energies and proceed with our deformation procedure.

2.3 Topological defects on crystalline shells

2.3.1 Set of minimal topological defects

Let us consider the set of minimal number of topological defects on a triangulated spherical surface that satisfy the Euler-Poincaré formula. This is the regime where the core energies are large so that the creation of topological defects is heavily penalized and the spherical shell prefers to have the minimum number of disclinations that satisfy equation (2.1). On a triangulated spherical surface, we can have 3-, 4-, 5-, 6-, 7-, 8-, 9-fold vertices. It may be useful to think of each site, with coordination number z, as having a topological charge of $6-z$ (indicating the strength of the disclination),

e.g. 3-fold site has charge +3, 4-fold site has charge +2 etc. Then equation (2.1) can be understood as a conservation of topological charge statement, i.e., the sum of topological charges on a spherical crystal lattice must add up to 12. Since 3-, 4-, 5-fold defects contribute positively, while 7-, 8-, 9-fold defects contribute negatively to the summation in equation (2.1), this means that any triangulated spherical surface must have a net excess of 3-, 4-, 5-fold defects compared to 7-, 8-, 9-fold defects in a sea of 6-fold sites that must add up to 12. There is a beautiful analogy to the BCS theory of superconductivity: the sea of 6-fold vertices are like the condensate of Cooper pairs in superconductivity and the various n-fold disclinations (n = 3, 4, 5, 7, 8, 9) are similar to the quasi-particle excitations which have long range interaction.

Since we are looking at the minimal number of topological defects (i.e., lowest energy configurations), we can restrict our attention to combinations of 3-, 4-, 5-fold defects. Let us denote the number of 3-, 4-, 5-fold disclinations by $\{n_1, n_2, n_3\}$, e.g. a sphere with 12 5-fold disclinations would be denoted by $\{0, 0, 12\}$. There are a total of 19 different possibilities and they fall into three distinct universality classes based on the number of distinct topological defects they have as shown in Table 2.1.

Table 2.1: Different configurations of topological defects.

# distinct defects	Different cases
1	$\{0,0,12\}$, $\{4,0,0\}$, $\{0,6,0\}$
2	$\{0,1,10\}$, $\{0,2,8\}$, $\{0,3,6\}$, $\{0,4,4\}$, $\{0,5,2\}$, $\{1,0,9\}$, $\{2,0,6\}$, $\{3,0,3\}$, $\{2,3,0\}$
3	$\{1,1,7\}$, $\{1,2,5\}$, , $\{1,3,3\}$, $\{1,4,1\}$, $\{2,1,4\}$, $\{2,2,2\}$, $\{3,1,1\}$

2.3.2 Spheres with one type of disclination

Consider a sphere created from an icosahedron that has defects associated with the $\{0, 0, 12\}$ class. This triangulation, which we will call the icosahedral-sphere (M_1), has exactly 12 5-fold defects at the vertices of an inscribed icosahedron. As the membrane shrinks, it starts to deform into a structure resembling that of an icosahedron (Fig. 2.2a), where there are noticeable buckling at the 12 disclination points which agrees with findings by earlier work [55, 109]. This shows that the disclination have very high energy and it is energetically favorable to buckle a 5-fold defect than to strain it.

On the other hand, the dodecahedral-sphere (M_2), which is dual to the icosahedral-sphere (M_1) and in the same $\{0, 0, 12\}$ class, the 5-fold disclinations lie in the center of the 12 pentagonal faces of an inscribed dodecahedron. M_2 will evolve to a structure that resembles a dodecahedron but with a protrusion from the center of each of the 12 pentagon face as shown in Fig. 2.2b. Although both M_1 and M_2 have 12 5-fold defects in them and they are all located on the vertices of an inscribed icosahedron, the defects on the two sphere have different relative orientation to one another as shown in Fig. 2.2. This difference in relative orientation among the 5-fold defects affects the pattern of the sea of 6-fold lattice sites surrounding them. This is the source of the long range effect of the disclination. Even as we refine the mesh and add more lattice sites between the disclinations, the relative orientations of the closest disclinations dictate the geometry of the membrane. Thus M_1 and M_2 evolve to different faceted surface under deformation even though they have the same number of topological defects. The positive (convex) disclination at the 5-fold site is also unsurprising since

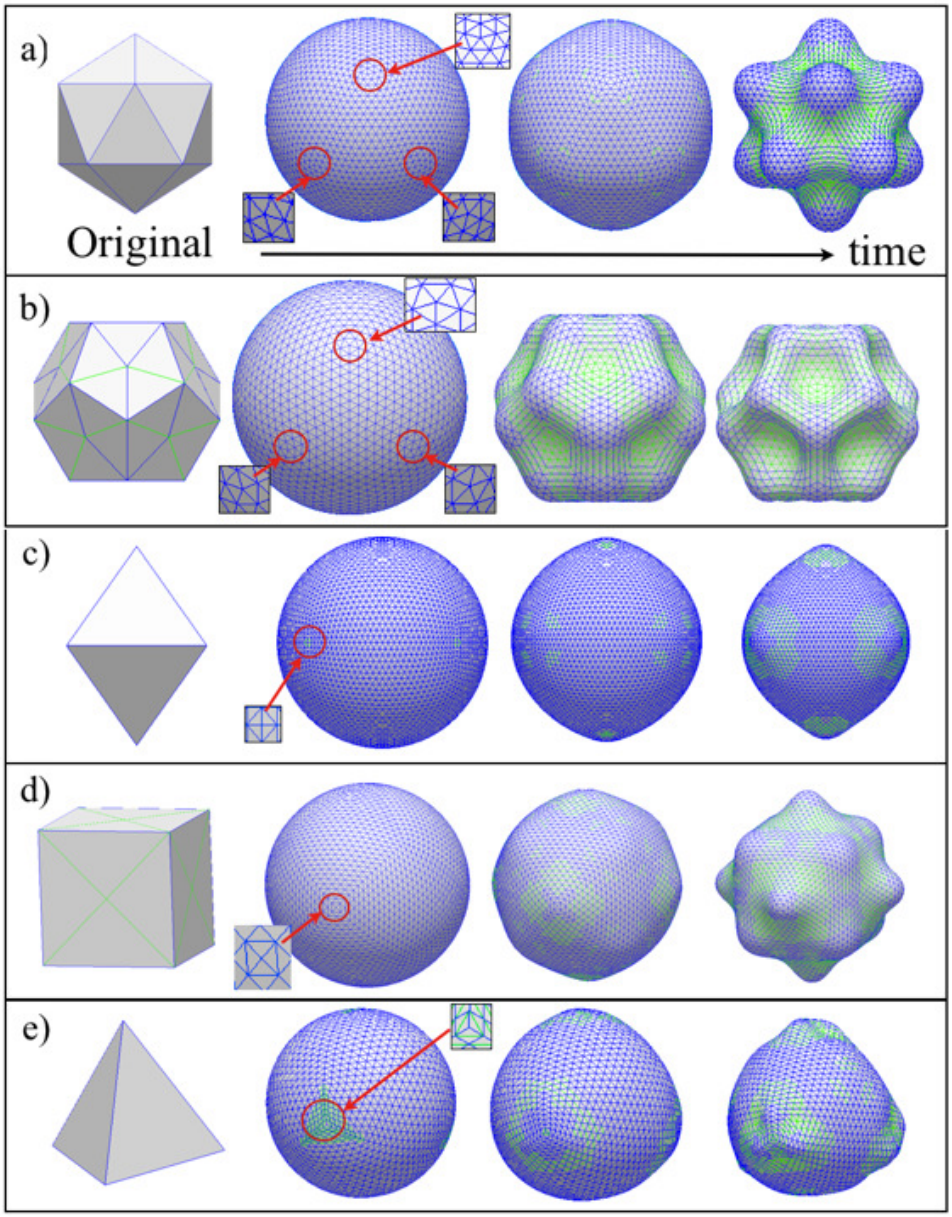

Figure 2.2: Simulations of a sphere with different disclinations shrinking with time (left to right). Diagrams are to scale. Leftmost picture of each row shows the original polyhedron. The second picture in each row shows the sphere formed from the different polyhedron before deformation. Third picture shows the sphere after shrinking by $\sim 20\%$ and the fourth picture shows the sphere after shrinking by $\sim 40\%$. Blue and green color denote convex and concave regions respectively. The disclinations are circled and zoomed in. (a) Icosahedron (M_1). (b) Dodecahedron (M_2). (c) Octahedron (M_3). (d) Cube (M_4). (e) Tetrahedron (M_5).

topological charges are attracted to regions of like-sign Gaussian curvature [70, 10, 20].

Next, we consider a sphere formed from the octahedron, the octahedral-sphere (M_3). There are six 4-fold defects on M_3, four of them equally space along the equator and one each on the North pole and South pole. The defects are oriented like a diamond along the equator and meridian as shown in Fig. 2.2c. Under deformation, M_3 evolves to a structure resembling an octahedron and the six 4-fold disclinations have buckled significantly compared to the rest of the shell. The sphere formed from a cube (M_4), which is dual to an octahedron and share the same symmetry group O, has six 4-fold disclinations and hence is in the same $\{0, 6, 0\}$ class as M_3. In this case, the six 4-fold defects are oriented like a square along the equator and meridian as shown in Fig. 2.2d. Under deformation, M_4 evolve to a octahedral-like surface and the location around the disclinations suffers the most buckling and lies at the vertices of the resulting deformed structure.

To complete the study of Platonic solids, we form a sphere made from a tetrahedron, the tetrahedral-sphere (M_5). In this case, there are exactly four 3-fold disclinations ($\{4, 0, 0\}$ class) and they lie on the vertices of an inscribed tetrahedron. This sphere will deform into a tetrahedral-like structure with the 3-fold disclinations located at the four vertices of the deformed structure. If we return to the Euler-Poincaré formula and think of $6 - z$ as the topological charge indicating the strength of the disclination, we see that sites with greater charge have a tendency to bend/buckle more, i.e., 4-fold sites can buckle more positively (convex) compared to a 5-fold site and 3-fold sites can buckle more positively (convex) compared to a 4-fold site. Conversely, 8-fold sites can buckle more negatively (concave) compared to 7-fold sites and

so on.

2.3.3 Spheres with more than one type of disclinations

Thus far, we have only considered spheres with only one type of disclination. Besides the Platonic solids, we find that the cuboctahedron ($\{0, 6, 0\}$), prism-6 ($\{0, 6, 0\}$) and antiprism-5 ($\{0, 0, 12\}$), also form spheres with singular defect type, to name a few. Next, let us consider spheres that contain 2 types of defects. We find that spheres formed from an antiprism-4 ($\{0, 2, 8\}$), pyramid-5 ($\{0, 5, 2\}$) or dipyramid-3 ($\{2, 3, 0\}$) fall under such category. The sphere formed from the antiprism-4 has a 4-fold disclination at the North and South poles each and eight 5-fold disclinations at the vertices of an inscribed antiprism-4 that zig zags along a belt around the equator ($2(+2) + 8(+1) = 12$). Upon deformation, the disclination sites will start to buckle and form and a structure that looks like a top as shown in the rightmost picture in Fig. 2.3a. The upper and lower half of the final shape are actually mirror images rotated by 90°, i.e., if you cut the top horizontally into two equal halves and rotate the lower half by 90° about a vertical axis and reflect it into the horizontal line, you will get the upper half.

The sphere formed from the pyramid-5 polyhedron ($2(+1) + 5(+2) = 12$) has a 5-fold disclination at the North and South pole each and five 4-fold defects evenly spaced along a line of latitude slightly below the equator as shown in Fig. 2.3b. The final shape after deformation looks somewhat like a pyramid-5 except with a bulging bottom. The sphere formed from a dipyramid-3 ($2(+3) + 3(+2) = 12$) has a 3-fold disclination at the North and South pole each and three 4-fold defects evenly

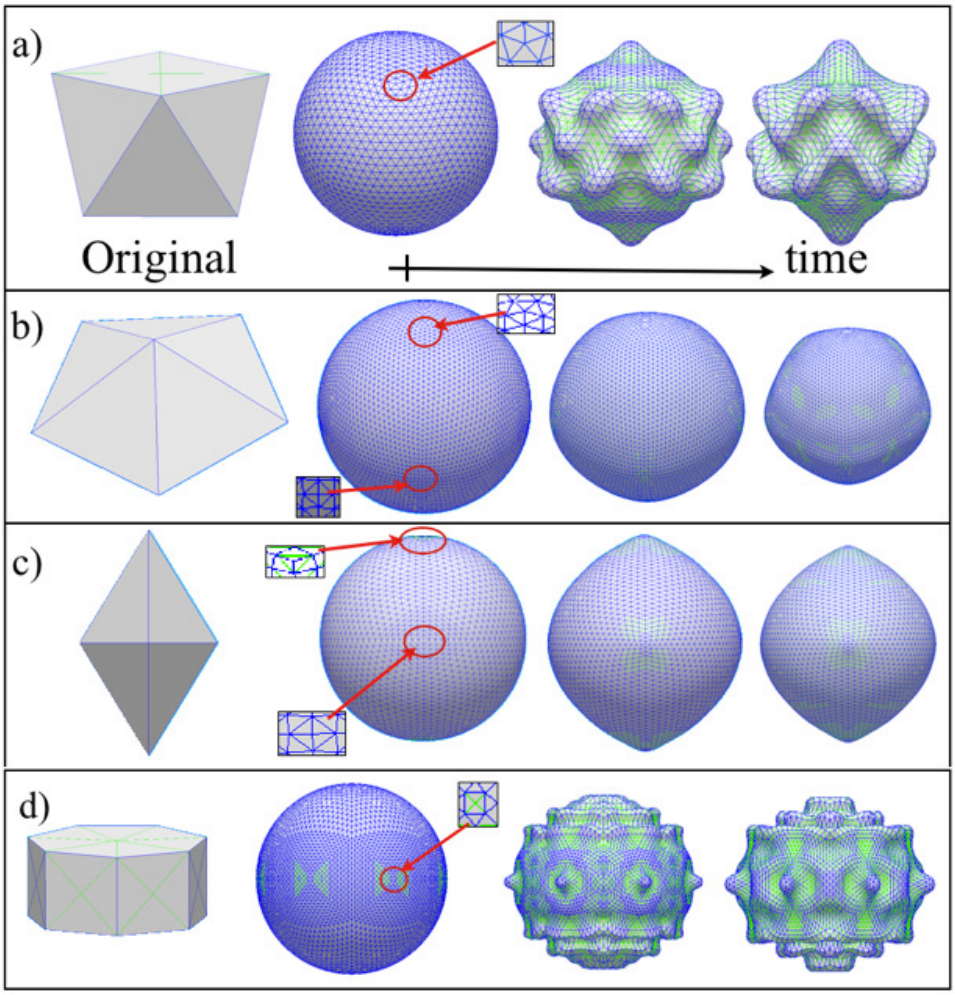

Figure 2.3: Simulations of a sphere with different disclinations shrinking with time (left to right). Diagrams are to scale. Leftmost picture of each row shows the original polyhedron. The second, third and fourth picture of each row shows the sphere at different time during the shrinking process. Blue and green color denote convex and concave edges respectively. The disclinations are circled and zoomed in. (a) Antiprism-4. (b) Pyramid-5. (c) Dipyramid-3. (d) Prism-7.

spaced along the equator as shown in Fig. 2.3c. This sphere slowly shrinks to form a structure that looks like a dipyramid-3 with sharper vertices at the North and South tip compared to the three vertices along the equator. This agrees with our understanding that sites with higher topological tend to buckle more.

2.3.4 Sphere with positive and negative disclinations

Lastly, let us consider polyhedrons that formed spheres with higher order disclinations other than the 3-, 4-, 5-fold defects that we have looked at so far. One example is a sphere created from a prism-7 as shown in Fig. 2.3d. The sphere thus formed has a 7-fold disclination at the North and South poles each and seven 4-fold disclinations ($2(-1) + 7(+2) = 12$). Under deformation, this sphere forms a beautiful structure with seven sides and a slightly pointed top and bottom cap, which closely resembles a prism-7, i.e., it is a prism-7 which bulging top and bottom surface as shown in Fig. 2.3d. The small area around the 7-fold disclination concave slightly inwards.

2.4 Elastic energies of thin crystalline shells

The spheres created from different polyhedrons have very different energies since the total energy U_T depends sensitively on the structure of the mesh, which as we saw in previous sections, is determined by the number of defects and their relative orientations. Most triangles in a spherical lattice are not equilateral (e.g. when we triangulate a square, we get four congruent right angle triangles instead of four equilateral triangles) and we will define the average length of the edges, $\bar{a}$ to be the lattice spacing a. As we refine the mesh, we get smaller lattice spacing a. We find that

as the ratio $R/a \gtrsim 10$ (continuum limit), the total energy of the sphere asymptotes, indicating that the minimal energy surface that we create under surface tension from the original polyhedron starts to approaches that of the perfect sphere. When $R/a \lesssim 1$, there are too few lattice sites on the sphere and hence the triangulation is not smooth. Refer to the Appendix for details.

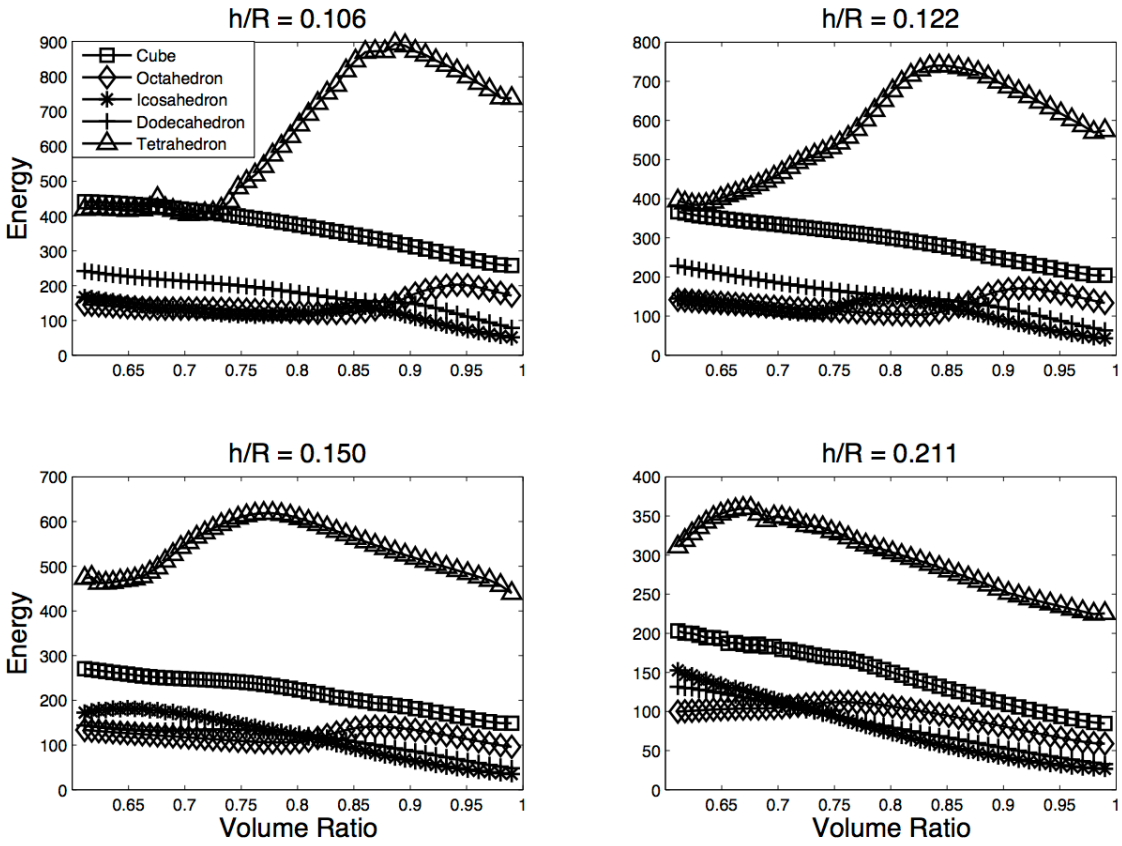

Figure 2.4: Plot of Energy vs Volume as the sphere shrinks for different values of h/R. Before deformation, the icosahedral-sphere (M_1) has the lowest energy followed closely by the dodecahedral-sphere (M_2). However, as we shrink the spheres, at some point, the octahedral-sphere (M_3) becomes energetically favorable. Thus for different volume reduction, the system will undergo structural transitions such as $M_1 \to M_2$, $M_1 \to M_2 \to M_3$ and $M_1 \to M_3$.

Depending on the mesh picked, there will be different stress and strain on the

shell. We find that the icosahedral-sphere (M_1) has the lowest energy, which agrees with previous studies [55, 109, 10]. This is followed closely by the dodecahedral-sphere (M_2), with an energy difference of less than 10%. This small difference in energy is unsurprising considering both M_1 and M_2 have the same symmetry. However, the difference in the relative orientation of the 5-fold disclinations results in dramatically different strain energy distribution on the sphere [7]. The octahedral-sphere is the third lowest followed by the cubical-sphere. The tetrahedral-sphere has significantly larger energy and this is because the four 3-fold disclinations create high amount of long range in-plain strain on the surface. Our findings also indicate that structures with $(P, 0)$ CK coordinates tend to have lower energies than their (P, P) counterparts. Also, different triangulations have different energy even as $R/a \to \infty$. This implies that once we pick a certain mesh, the allowable modes of excitations are already 'locked in'. If we think in terms of spherical harmonic modes ℓ, this means that only certain ℓ modes are permissible depending on the symmetry of the mesh. This observation will be expounded in greater detail in a later section.

Although the icosahedral-sphere (M_1) has the lowest energy before deformation, at some point during the shrinking process, the dodecahedral-sphere (M_2) starts to be energetically favorable. The full result of the total elastic energy as a function of volume for the five Platonic spherical shells at different h/R is shown in Fig. 2.4. As can be seen from Fig. 2.5, at high volume reduction, the dodecahedral-sphere (M_2) starts to form more bumps on its surface compared to the icosahedral-sphere (M_1) which is able to more effectively "screen" the 5-fold disclinations from one another. The total energy is a fine balance between bending and stretching and the small

increase in bending energy is more than compensated by the larger decrease in strain energy. The deformed shells appear to retains its original symmetry throughout the course of crumpling. This introduces the possibility of structural transition from M_1 to M_2 as the deformation becomes more pronounced.

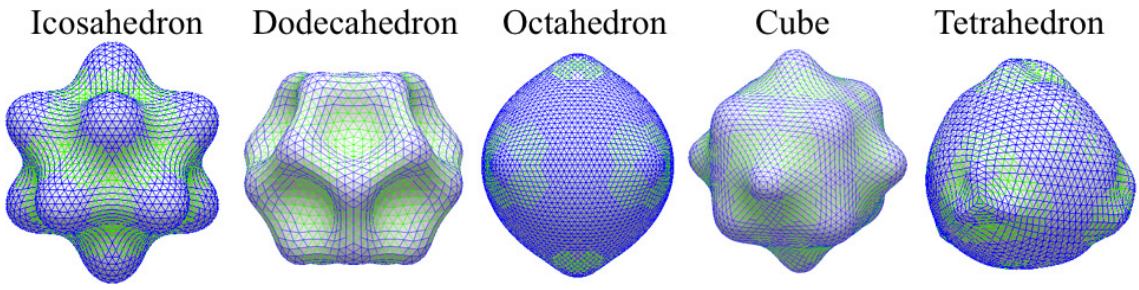

Figure 2.5: Comparison of the extend of buckling for shell with same symmetry group G but different CK coordinates for $h/R = 0.118$ at volume shrinkage of $\sim 40\%$. (a) dodecahedral-sphere (P, P) is more faceted than the icosahedral-sphere $(P, 0)$. (b) On the other hand, the faceting of the octahedral-sphere $(P, 0)$ is significantly different from the cubical-sphere (P, P).

For thin shells ($h/R \lesssim 0.15$), the octahedral-sphere can become the energetically favored state at high enough volume contraction and we see the possibility of structural transition pathways such as $M_1 \to M_2$, $M_1 \to M_2 \to M_3$ and $M_1 \to M_3$. The energy of the tetrahedral-sphere drops rapidly once it starts to crumple and form highly faceted structure as shown in Fig. 2.5 and the structural transition pathway $M_4 \to M_5$.

2.5 Phase space

When we shrink a spherical covering created from a particular polyhedron, most of the times we get a highly complex structure at high volume reduction and rarely, if

ever, do we get a crumpled structure that resembles original polyhedron. The shape of the deformed shell depends sensitively on the thickness of the shell h, the radius of the sphere R and the lattice spacing a and we would like to understand in what region of phase space (h, R, a) do we get a crumpled sphere that resembles the original polyhedron. Given a particular mesh type, we will explore the phase space of the final crumpled shape based on two dimensionless parameters, namely: h/R (aspect ratio) and R/a (lattice ratio). In particular, we have narrowed our attention to the class of spheres formed from Platonic solids and the final results are shown in Figs. 2.6, 2.7 and 2.8. h/R can be varied freely since it is controlled by the two elastic modulus Y and κ that we can set arbitrarily. Due to the algorithm that we use for subdivision, in which each edge is divided in two, and each triangle is divided into four new ones in a regular manner, R/a can only take on certain values at each step of the mesh refinement resulting in a somewhat coarseness in the R/a direction in the phase space diagrams.

The phase digram for the different spherical lattices appear to have the same qualitative features. As we vary the aspect ratio h/R, we find that thick spheres ($h/R \gtrsim 0.1$) tend to crumple isotropically and the deformed structure is generally smooth with no noticeable faceting; thin spherical shells tend to crumple into highly faceted structures. On the other hand, at low lattice ratio R/a, we generally get simpler crumpled structures since there are less degrees of freedom; as we increase R/a, we get more and more complicated deformed structures. At intermediate values of h/R and R/a, we do get structures that look like the original polyhedron. The striking similarities in the five phase diagrams suggest that the crumpling behavior is

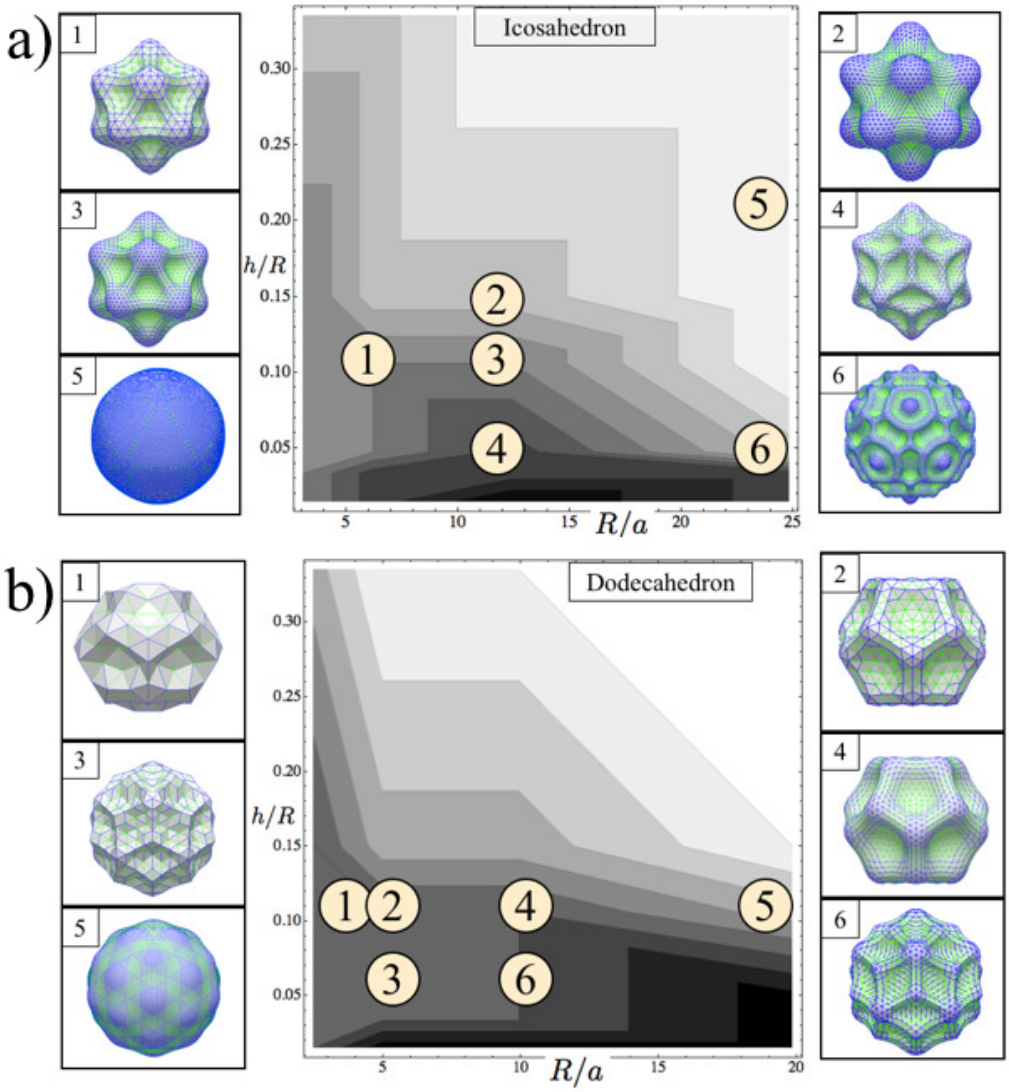

Figure 2.6: (a) The morphological phase diagram of sphere with icosahedral defect (M_1) as a function of the aspect ratio h/R and lattice ratio R/a. (1) corresponds to a shell with $h/R = 0.12$, $R/a = 3.1$; (2) corresponds to $h/R = 0.15$, $R/a = 6.2$; (3) corresponds to $h/R = 0.12$, $R/a = 6.2$ (This corresponds to the final crumpled shape of Fig. 2.2a); (4) corresponds to $h/R = 0.05$, $R/a = 12.4$; (5) corresponds to $h/R = 0.22$, $R/a = 24.8$; (6) corresponds to $h/R = 0.04$, $R/a = 24.8$. In all the simulations, the volume of the sphere is reduced by 40%. Color scheme used: White = spherical; Black = crumpled; Grey = polyhedral. (b) The morphological phase diagram of sphere with dodecahedral defect (M_2) as a function of the aspect ratio h/R and lattice ratio R/a. The final crumpled shape of Fig. 2.2b is (4).

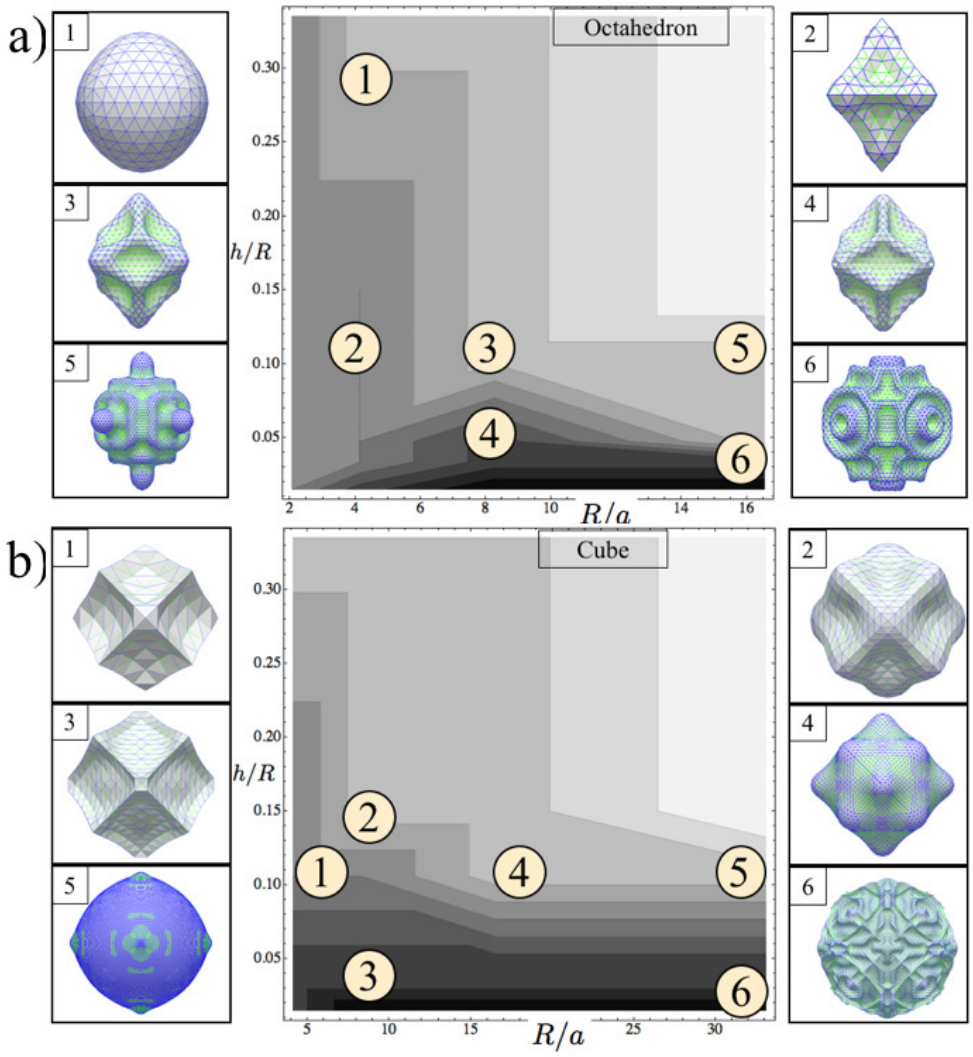

Figure 2.7: (a) The morphological phase diagram of sphere with octahedral defect (M_3) as a function of the aspect ratio h/R and lattice ratio R/a. (b) The morphological phase diagram of sphere with cubical defect (M_4) as a function of the aspect ratio h/R and lattice ratio R/a. (1) corresponds to a shell with $h/R = 0.3$, $R/a = 4.0$; (2) corresponds to $h/R = 0.12$, $R/a = 4.0$; (3) corresponds to $h/R = 0.12$, $R/a = 8.0$; (4) corresponds to $h/R = 0.05$, $R/a = 8.0$; (5) corresponds to $h/R = 0.12$, $R/a = 16.0$; (6) corresponds to $h/R = 0.04$, $R/a = 16.0$. In all the simulations, the volume of the sphere is reduced by 40%. Color scheme used: White = spherical; Black = crumpled; Grey = polyhedral. The final crumpled shape of Fig. 2.2c lies somewhere around (3) and (4). (b) The morphological phase diagram of sphere with cubical defect (M_4) as a function of the aspect ratio h/R and lattice ratio R/a. The final crumpled shape of Fig. 2.2d is (4).

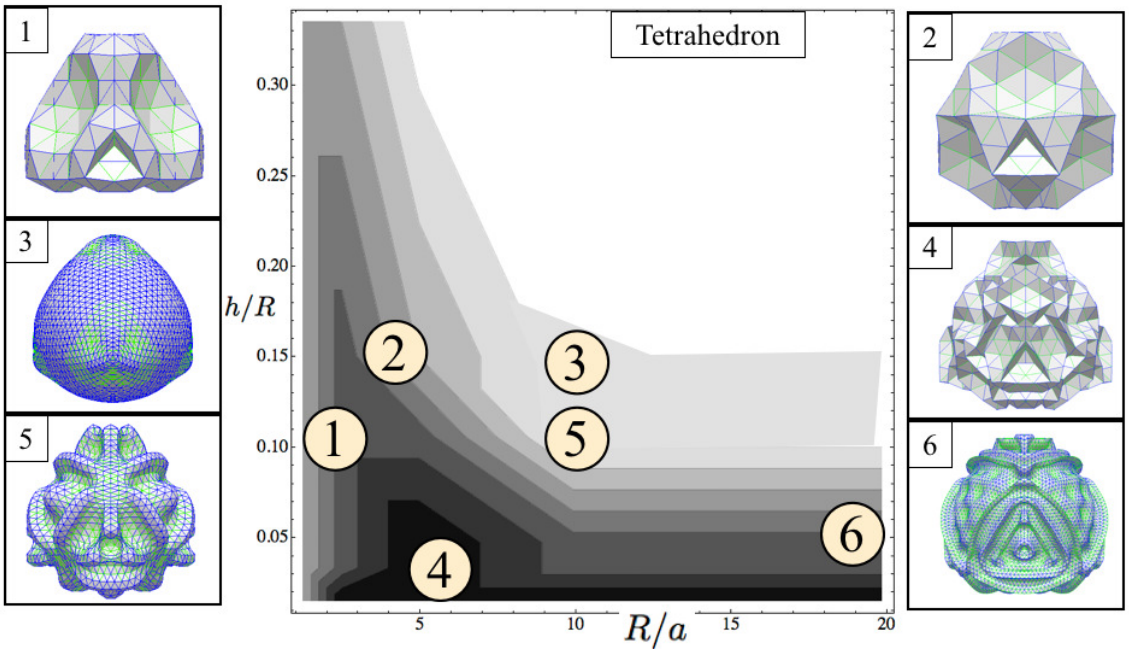

Figure 2.8: The morphological phase diagram of sphere with tetrahedral defect (M_5) as a function of the aspect ratio h/R and lattice ratio R/a. (1) corresponds to a shell with $h/R = 0.12$, $R/a = 1.4$; (2) corresponds to $h/R = 0.15$, $R/a = 2.8$; (3) corresponds to $h/R = 0.15$, $R/a = 11.6$ (This is the final crumpled shape of Fig. 2.2e); (4) corresponds to $h/R = 0.03$, $R/a = 5.8$; (5) corresponds to $h/R = 0.12$, $R/a = 11.6$; (6) corresponds to $h/R = 0.05$, $R/a = 23.2$. In all the simulations, the volume of the sphere is reduced by 40%. Color scheme used: White = spherical; Black = crumpled; Grey = polyhedral.

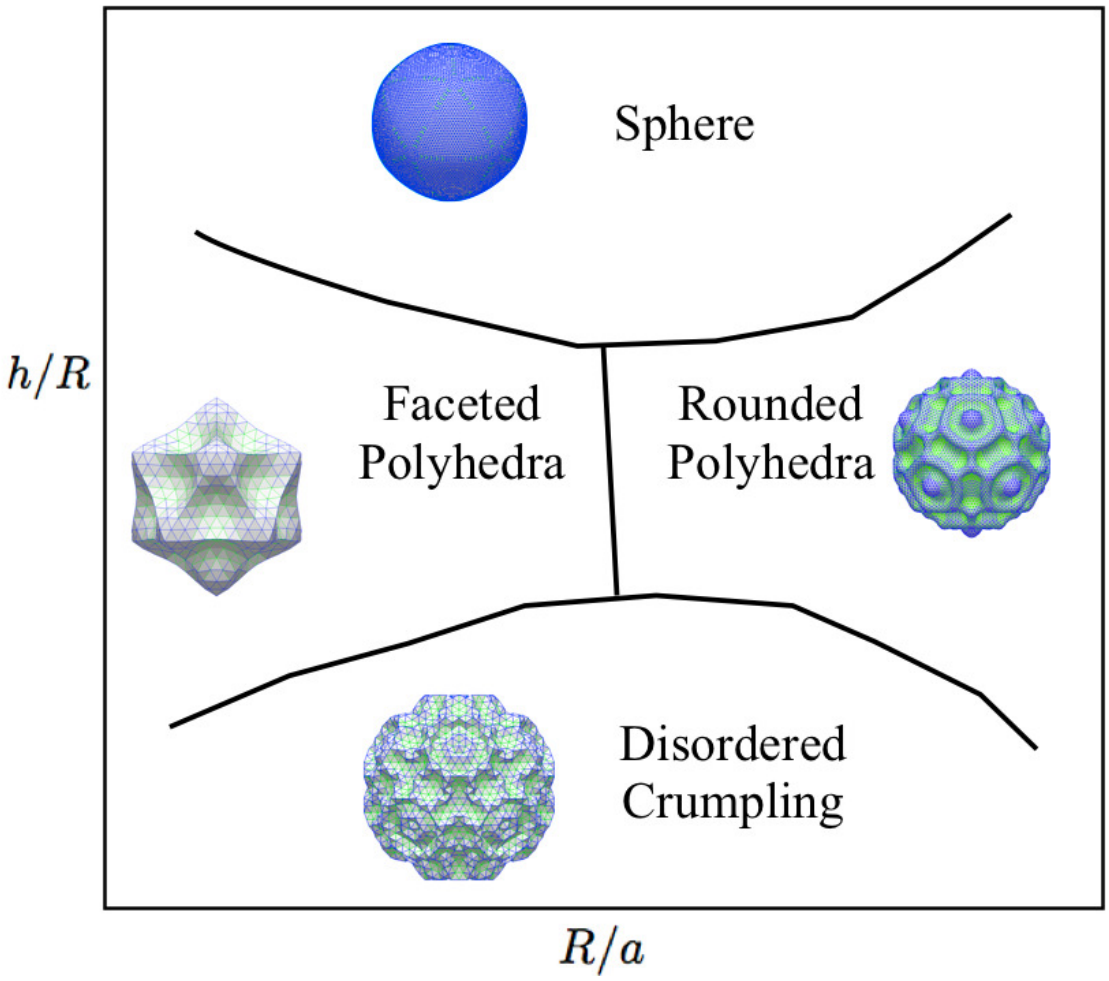

Figure 2.9: Phase diagram as a function of h/R and R/a. For small h/R and R/a, we get simple faceted crumpled final states. As R/a increase, the crumpled state gets more complex. On the other hand, as h/R increase, bending becomes increasingly energetically prohibitive, hence the sphere shrinks isotropically.

very generic and the phase diagram for any triangulated lattice should look qualitatively like Fig. 2.9. The boundaries are not well defined and it is a smooth transition going from one region to another.

2.6 Classification of shell type

From the numerical simulation, we find that if we form a triangulated spherical covering and put in some defects denoted by $\{n_1, n_2, n_3\}$, such that the disclinations obeys certain group symmetry G, i.e., the set of topological defects are invariant under the action of group G, then we expect that such as a sphere would, under shrinking, deform into a structure that resembles a polyhedron that has the symmetry of G. Consider two thin spherical shells formed from an octahedron and a cube respectively as shown in Fig. 2.10. Both spheres are invariant under the 48 element octahedral symmetry group $O_h \simeq O \times C_2$ and yet they deform to slightly different structure under shrinking (see Fig. 2.2). We see that specifying the group is not a *sufficient* classification as the relative orientation of the defects to one another, which plays an important role in determining the final shape of the deformed sphere, is not specified by the symmetry group. This issue with orientation stems from the long range interaction of disclinations and forbids a simple global defect theory to explain shell deformation.

The icosadeltahedral lattice [55, 93, 17], i.e., vertices on the lattice have coordination number either five or six, can be classified by a pair of integers (P, Q) known as the "Casper-Klug" (CK) coordinates, which indicates how the 5-fold sites are connected. The shortest path connecting a pair of nearest neighbor 5-coordinated

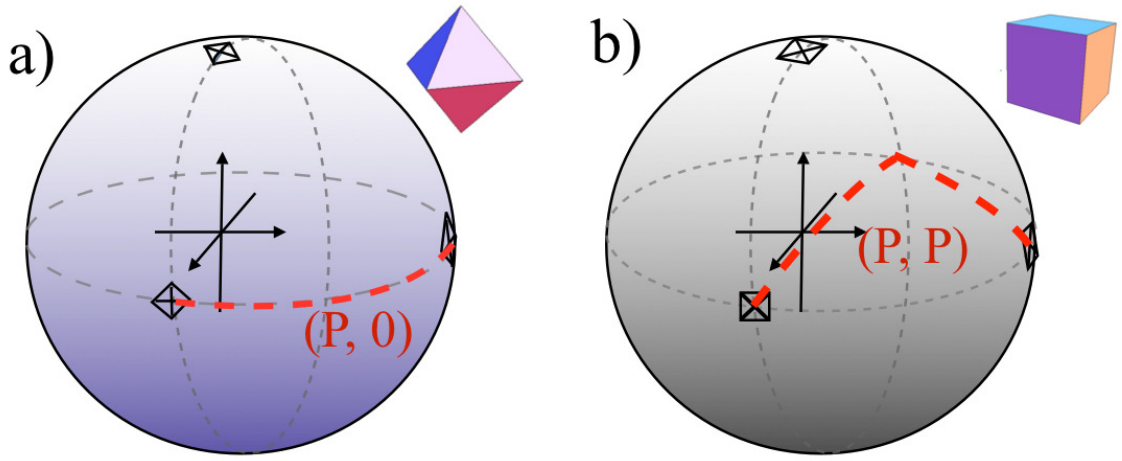

Figure 2.10: Spheres formed from octahedron (M_3) and cube (M_4). (a) Octahedron: The defects are oriented like a diamond at the six intersections of the x-, y-, z-axis with the sphere. "Casper-Klug" coordination is $(P, 0)$: takes P steps to move between a pair of closest neighbor 4-fold disclination as shown. (b) Cube: The defects are oriented like a square at the six intersection points. (P, P): takes P steps in one direction and P steps in another to move between a pair of closest neighbor 4-fold disclination.

vertices consist of P edges (steps) in some direction and Q edges in another direction on the spherical triangulation. Structures with P and Q non-zero and $P \neq Q$ are chiral. Their symmetry group is the chiral icosahedral symmetry group I of order 60. Structures with P or $Q = 0$, or with $P = Q$ are non-chiral and has the full icosahedral symmetry $I_h = I \times C_2$. In particular, the icosahedral-sphere (M_1) belongs to the class $(P, 0)$ while the dodecahedral-sphere (M_2) belongs to (P, P). The T number of the covering is given by $T = P^2 + Q^2 + PQ$, and is related to the number of vertices $V = 10\,T + 2$.

The "Casper-Klug" (CK) coordinates (P, Q) let us specify the relative orientation of the disclinations in an unambiguous manner for the icosadeltahedral lattice. In a similar fashion, we can extend the "Caspar-Klug" classification to include 3-, 4-fold

sites. The summary is shown in Table 2.2. Thus, we see that to fully classify the defects on a spherical lattice, it is necessary and sufficient to include

1. number and type of disclinations,

2. the full symmetry group of the defects G,

3. the "Casper-Klug" coordinates (P, Q).

Table 2.2: "Caspar-Klug" classification for thin crystalline shells.

Type of sphere	Symmetry	CK coordinates	# vertices
icosahedral-sphere (M_1)	I_h	$(P, 0)$	$V = 10\,T + 2$
dodecahedral-sphere (M_2)	I_h	$(P, 0)$	$V = 10\,T + 2$
octahedral-sphere (M_3)	O_h	$(P, 0)$	$V = 4\,T + 2$
cubical-sphere (M_4)	O_h	(P, P)	$V = 4\,T + 2$
Tetrahedral-sphere (M_5)	T_d	$(P, 0)$	$V = 2\,T + 2$
Antiprism-4-sphere	D_{4d}	$(P, 0)$	$V = 8\,T + 2$
Pyramid-5-sphere	C_{5v}	$(P, 0)$	$V = 5\,T + 2$
Dipyramid-3-sphere	D_{3h}	$(P, 0)$	$V = 3\,T + 2$
Prism-7-sphere	D_{7h}	(P, P)	$V = 7\,T + 2$

2.7 Shape Analysis

2.7.1 Group Theory

There are only three symmetry groups associated with the Platonic solids rather than five, since the symmetry group of any polyhedron coincides with that of its dual. Any symmetry of the original polyhedron must be a symmetry of the dual and vice-versa. The three polyhedral groups are: 1) the tetrahedral group T 2) the octahedral group O (which is also the symmetry group of the cube), and 3) the icosahedral group

I (which is also the symmetry group of the dodecahedron). Group theory tells us that $O \simeq S_4 \times C_2$ and $I \simeq A_5 \times C_2$, which implies that O and I have point inversion symmetry. For example, under point inversion, any point located at (θ, ϕ) in spherical coordinates will be transformed to $(\pi - \theta, \phi + \pi)$. Suppose we choose to parametrize a surface $r(\theta, \phi)$ using spherical harmonics, i.e.,

$$r(\theta, \phi) = \sum_{\ell=0}^{\infty} \sum_{m=-\ell}^{\ell} a_\ell^m \, Y_\ell^m(\theta, \phi). \tag{2.8}$$

If the surface has either O or I symmetry and hence obey point inversion, then

$$P\left[r(\theta, \phi)\right] = r(\pi - \theta, \phi + \pi) = \sum_{\ell=0}^{\infty} \sum_{m=-\ell}^{\ell} a_\ell^m \, Y_\ell^m(\pi - \theta, \phi + \pi),$$

where P is the point inversion operator. Since

$$Y_\ell^m(\pi - \theta, \pi + \phi) = (-1)^\ell Y_\ell^m(\theta, \phi), \tag{2.9}$$

we see that such a surface can only be described by a sum of even ℓ spherical harmonics. The tetrahedral group does not have point inversion symmetry so there is no restrictions on the allowed ℓ for the spherical harmonics. Also, since the surface $r(\theta, \phi)$ is real, this means that

$$r(\theta, \phi) = \sum_{\ell=0}^{\infty} \sum_{m=-\ell}^{\ell} a_\ell^m \, Y_\ell^m = \sum_{\ell=0}^{\infty} \sum_{m=-\ell}^{\ell} (a_\ell^m)^* \, (Y_\ell^m)^*.$$

Using the fact that

$$(Y_\ell^m)^* = (-1)^m Y_\ell^{-m},$$

this implies that

$$(a_\ell^{-m})^* = (-1)^m a_\ell^m. \tag{2.10}$$

One simple consequence is that a_ℓ^0 is always real.

2.7.2 Comparison with crumpled spheres

We can analyze the shapes of the deformed shells by looking at the spherical harmonics expansion of the vertices. The radial density of the vertices on the surface is defined by

$$D(\theta,\phi) = \sum_{i}^{N} R_i \delta(\phi - \phi_i)\delta(\cos\theta - \cos\theta_i), \tag{2.11}$$

where (θ_i, ϕ_i, R_i) represents the polar coordinates of vertex i ($i = 1, \ldots N$). Expanding the radial density in spherical harmonics up to $\ell = L$,

$$D(\theta,\phi) = \sum_{\ell=0}^{L} \sum_{m=-\ell}^{\ell} a_\ell^m Y_\ell^m(\theta,\phi), \tag{2.12}$$

we can understand the important small ℓ modes that are excited. For example, we look at the spherical harmonic expansion of some of the $h/R = 0.118$ shells that have been shrunk by approximately 20% (See Fig. 2.11). These shells have R/a of

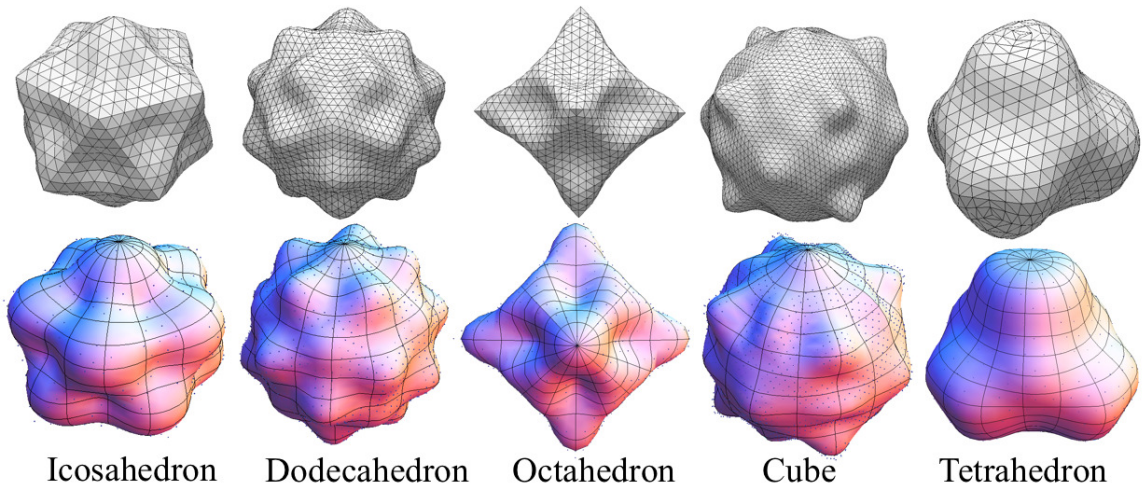

Figure 2.11: Crumpled shells (with volume shrinkage 20%) on the top row are the images from Surface Evolver. The images on the bottom row are the spherical harmonic approximation of the crumpled shells from the top shell as described by equation (2.13). The small dots on the bottom figures are the data points of the vertices.

around 20. For this set of five crumpled spheres, we find that the spherical harmonic

expansion is given by:

$$\begin{aligned}
r_{cube}(\theta,\phi) &\approx Y_0^0 + (0.003)Y_4^0 + (0.002)(Y_4^4 + Y_4^{-4}) + ..., \\
r_{oct}(\theta,\phi) &\approx Y_0^0 + (0.094)Y_4^0 + (-0.056)(Y_4^4 + Y_4^{-4}) + ..., \\
r_{ico}(\theta,\phi) &\approx Y_0^0 + (0.082)Y_6^0 + (-0.066)(Y_6^5 - Y_6^{-5}) + ... \\
r_{dodec}(\theta,\phi) &\approx Y_0^0 + (0.032)Y_6^0 + (-0.027)(Y_6^5 - Y_6^{-5}) + ..., \\
r_{tetra}(\theta,\phi) &\approx Y_0^0 + (0.059)Y_3^0 + (-0.036)(Y_3^3 - Y_3^{-3}) \\
&\quad +(0.038)Y_4^0 + (0.046)(Y_4^3 - Y_4^{-3}) + (-0.007)Y_6^0 \\
&\quad +(0.004)(Y_6^3 - Y_6^{-3}) + (-0.004)(Y_6^6 + Y_6^{-6}) + ...,
\end{aligned} \tag{2.13}$$

where we have rescaled a_0^0 to 1 and shown only the first few non-zero ℓ terms. This result can be compared to the spherical harmonic expansion for the Platonic solids resulting from Onaka's formulation [77]:

$$\begin{aligned}
r_{cube}(\theta,\phi) &\approx Y_0^0 + (-0.086)Y_4^0 + (-0.051)(Y_4^4 + Y_4^{-4}) + ..., \\
r_{oct}(\theta,\phi) &\approx Y_0^0 + (0.076)Y_4^0 + (0.046)(Y_4^4 + Y_4^{-4}) + ..., \\
r_{ico}(\theta,\phi) &\approx Y_0^0 + (-0.007)Y_6^0 + (0.016)(Y_{6,2} + Y_{6,-2}) \\
&\quad +(0.013)(Y_{6,4} + Y_{6,-4}) + (-0.011)(Y_{6,6} + Y_{6,-6}) + ..., \\
r_{dodec}(\theta,\phi) &\approx Y_0^0 + (0.009)Y_6^0 + (0.022)(Y_6^2 + Y_6^{-2}) \\
&\quad +(-0.018)(Y_6^4 + Y_6^{-4}) + (-0.015)(Y_6^6 + Y_6^{-6}) + ..., \\
r_{tetra}(\theta,\phi) &\approx Y_0^0 + (-0.148i)(Y_3^2 - Y_3^{-2}) + (0.002)Y_4^0 + (0.001)(Y_4^4 + Y_4^{-4}) \\
&\quad +(0.031)Y_6^0 + (-0.057)(Y_6^4 + Y_6^{-4}) + ...
\end{aligned} \tag{2.14}$$

The same ℓ modes appear in both equations (2.13) and (2.14), suggesting that the disclinations are largely responsible for the geometry of the crumpled shells. Here we find that the spherical harmonic expansion of the crumpled icosahedral-sphere (M_1), dodecahedral-sphere (M_2), octahedral-sphere (M_3) and cubical-sphere (M_4) contain even ℓ harmonics and that the low ℓ modes are the dominant modes at the onset of crumpling. On the other hand, the tetrahedral-sphere (M_5) have both even and odd ℓ modes. As the shell crumple even further, we find that in general, lower ℓ modes will shrink while the higher ℓ modes will grow in magnitude and importance.

2.7.3 "Shape" Spectroscopy

The set of spherical harmonics $Y_\ell^m(\theta, \phi)$ for a given ℓ forms a $(2\ell+1)$-dimensional representation of the rotational group SO(3). This means that the a_ℓ^m's for a given ℓ can be scrambled by a simple rotation of coordinates. Therefore, it is better to look at rotationally invariant quantities formed from the various a_ℓ^m that measure the angular projection onto the different ℓ [95, 113, 95]. One such invariant quantity is Q_ℓ, defined as

$$Q_\ell = \left(\frac{4\pi}{2\ell+1} \sum_{m=-\ell}^{\ell} |a_\ell^m|^2 \right)^{1/2}. \tag{2.15}$$

Q_ℓ measures the "magnitude" of the $(2\ell+1)$ order parameter a_ℓ^m. The quantity a_0^0, which corresponds to a constant spherical harmonics $Y_0^0 = 1/\sqrt{4\pi}$, is always nonzero, and scales with the size of the initial sphere R. Therefore, it is useful to normalized the various Q_ℓ by Q_0, so that it is independent of the overall magnitude of the $\{a_0^0\}$ for any given ℓ, namely,

$$\hat{Q}_\ell = Q_\ell / Q_0. \tag{2.16}$$

A larger $\hat{Q}_\ell$ implies a greater degree of asphericity.

The initial sphere has perfect spherical symmetry and the only nonzero mode is the $\ell = 0$ mode, i.e., only a_0^0 is non-vanishing. However, as the sphere crumples, the deformed shell starts to take on interesting shapes, with nonvanishing $\hat{Q}_\ell$'s, where $\ell \neq 0$. For example, $\hat{Q}_4$ measures tetrahedral or cubic symmetry and $\hat{Q}_6$ measures the icosahedral symmetry and so on. We calculate the $\hat{Q}_\ell$'s for the different Platonic-spheres at the end of the crumpling process, at volume shrinkage of around 40%. We find that the crumpled icosahedral-sphere has nonzero spherical harmonics only for $\ell = 0, 6, 10, 12, ...$, which strongly suggests that the set of topological defects is able to enforce the icosahedral symmetry as it crumples. The dodecahedral-sphere has the same angular momentum ℓ modes as the icosahedral-sphere. The cubical-sphere and octahedral-sphere have nonvanishing spherical harmonics for $\ell = 0, 4, 6, 8, 10, ...$ and the tetrahedral-sphere has $\ell = 0, 3, 4, 6, 7, 8, 9, 10, ...$ Some typical values of $\hat{Q}_\ell$ for the Platonic-spheres with $h/R = 0.118$ is shown in table 2.3.

Table 2.3: Normalized invariant $\hat{Q}_\ell$ for the different Platonic-spheres with $h/R = 0.118$. Note that $\hat{Q}_0 = 1$ by definition.

Type of shell	R/a	$\hat{Q}_3$	$\hat{Q}_4$	$\hat{Q}_6$	$\hat{Q}_7$	$\hat{Q}_8$	$\hat{Q}_9$	$\hat{Q}_{10}$
Icosahedron	10.9	0	0	0.0351	0	0	0	0.0093
Dodecahedron	9.5	0	0	0.0142	0	0	0	0.0170
Cube	12.3	0	0.0235	0.0126	0	0.00629	0	0.0099
Octahedron	7.3	0	0.0412	0.0492	0	0.00030	0	0.0098
Tetrahedron	9.7	0.0287	0.0251	0.0030	0.0047	0.00034	0.00234	0.0009

The normalized invariant $\hat{Q}_\ell$ varies as we change the two non-dimensional parameters h/R as well as R/a. The values of the normalized $\hat{Q}_\ell$ is illustrated in Table 2.4, which shows $\hat{Q}_6$ and $\hat{Q}_{10}$ for different values of h/R and R/a for the icosahedral-sphere. As R/a increases, we find that $\hat{Q}_6$ decreases while $\hat{Q}_{10}$ increases, which implies that

higher order ℓ modes becomes more important as the mesh spacing becomes finer, which is very reasonable. Similarly, we find that as the shell becomes thinner (smaller h/R), $\hat{Q}_6$ decreases while $\hat{Q}_{10}$ increases since more excitations are transferred from the lower order ℓ modes to the higher order ℓ modes.

Table 2.4: Normalized invariant $\hat{Q}_6$ and $\hat{Q}_{10}$ for different values of h/R and R/a of the icosahedral-sphere.

h/R	R/a	$\hat{Q}_6$	$\hat{Q}_{10}$	h/R	R/a	$\hat{Q}_6$	$\hat{Q}_{10}$
0.235	5.55	0.0363	0.0095	0.0745	5.55	0.0177	0.0150
0.235	11.55	0.0080	0.0003	0.0745	11.55	0.0200	0.0155
0.235	22.87	0.0039	0.0012	0.0745	22.87	0.00580	0.00001
0.118	5.55	0.0363	0.0095	0.0372	5.55	0.00583	0.00004
0.118	11.55	0.0357	0.0097	0.0372	11.55	0.00819	0.0199
0.118	22.87	0.0038	0.0170	0.0372	22.87	0.00517	0.0014

There is another important normalized invariant quantity that measures the symmetry of a cluster of points, namely [95],

$$W_\ell = \sum_{m_1+m_2+m_3=0} \begin{pmatrix} \ell & \ell & \ell \\ m_1 & m_2 & m_3 \end{pmatrix} a_\ell^{m_1} a_\ell^{m_2} a_\ell^{m_3}, \tag{2.17}$$

where

$$\begin{pmatrix} j_1 & j_2 & j_3 \\ m_1 & m_2 & m_3 \end{pmatrix} \tag{2.18}$$

is the Wigner $3j$-symbol. The Wigner $3j$-symbol is zero unless all these conditions are satisfied [67]:

$$m_1 + m_2 + m_3 = 0, \tag{2.19}$$

$$j_1 + j_2 + j_3 \in \mathbb{Z} \quad \text{(Integer perimeter rule)}, \tag{2.20}$$

$$|m_i| \leq j_i; \quad m_i \in \mathbb{Z}, \tag{2.21}$$

and

$$|j_1 - j_2| \leq j_3 \leq j_1 + j_2. \tag{2.22}$$

W_ℓ is a sensitive measure of the orientational symmetry of the shell. Similarly to Q_ℓ, we can normalize W_ℓ so that it does not depending on the overall scale of a_ℓ^m:

$$\hat{W}_\ell = \frac{W_\ell}{[\sum_m |a_\ell^m|^2]^{3/2}}. \tag{2.23}$$

For example, if we rescale each a_ℓ^m by a constant factor c, the magnitude of $\hat{W}_\ell$ remains the same since it is invariant under overall scaling.

The $\hat{Q}_\ell$ and $\hat{W}_\ell$ are akin to "shape spectroscopy" and will shed light to the geometry of the shell. $\hat{Q}_\ell$ measures the importance of the different $\ell \neq 0$ modes relative to $\ell = 0$ mode while $|\hat{W}_\ell|$ measures the symmetry of the shell. Given a shell, we can find how cubical, icosahedral or tetrahedral it is by evaluating the $\hat{W}_\ell$'s and compare them with the entries in Table 2.5, which are the $|\hat{W}_\ell|$'s of the Platonic solid calculated using the Onaka's formula [77]. Despite their rather different shapes, we find that the icosahedral-sphere and dodecahedron sphere have identical $\hat{W}_\ell$'s, except for a sign. This result is not so surprising in light of the fact that they belong to the same symmetry group I since the parameters are a direct index of the symmetry of the vertices. The closer the set of $\hat{W}_\ell$'s of the crumpled shell to the values for the ideal Platonic solid, the greater the degree of resemblance. The sign of the $\hat{W}_\ell$ depends on the sign of a_ℓ^0, which in turn depends on the coordinate system. We can relate the a_ℓ^m's in one coordinate system to another using the Wigner matrices $D_{m,m'}^{(\ell)}$ viz.

$$(a_\ell^m)^{new} = \sum_{m'} D_{m,m'}^{(\ell)}(\alpha, \beta, \gamma) a_\ell^m, \tag{2.24}$$

where α, β, γ are the usual Euler angles. The Wigner matrices $D^{(\ell)}_{m,m'}$ form a $(2\ell+1)$-dimensional representation of the rotational group. Since we are only interested in the symmetry of the surface, only the magnitude is of significance and hence, we will consider $|\hat{W}_\ell|$ instead of $\hat{W}_\ell$ for the rest of this paper. We will elaborate further on this point in Sec. 2.9.

Table 2.5: Normalized invariant $|\hat{W}_\ell|$ for the five Platonic solids.

Type	$\lvert\hat{W}_4\rvert$	$\lvert\hat{W}_6\rvert$	$\lvert\hat{W}_8\rvert$	$\lvert\hat{W}_{10}\rvert$	$\lvert\hat{W}_{12}\rvert$
Icosahedron	–	0.169754	–	0.0939683	0.0990394
Dodecahedron	–	0.169754	–	0.0939683	0.0990394
Cube	0.159317	0.0131606	0.0584548	0.0901302	0.0146554
Octahedron	0.159317	0.0131606	0.0584548	0.0901302	0.0268426
Tetrahedron	0.159317	-0.0131606	0.0584548	0.0901302	0.0129313

For the case of the icosahedral-sphere, we find that the first two non-zero $|\hat{W}_\ell|$'s are $|\hat{W}_6| = 0.169754$ and $|\hat{W}_{10}| = 0.0939683$ and that $\hat{W}_\ell$ appear to be independent of h/R and R/a based on the phase space we considered. Additionally, for our icosahedral-sphere, we find that all the a_6^m vanish except a_6^0 and $a_6^{\pm 5}$, and that

$$\left(a_6^0\right)^2 = \frac{11}{7}|a_6^{\pm 5}|^2. \tag{2.25}$$

This agrees exactly with earlier works [95, 14, 87] and that this is in fact an extremalizing solution that maximizes equation (2.17). We find that for all the crumpled icosahedron-shells listed in Table 2.4, equation (2.25) is satisfied to within 1%, showing a strong signature of icosahedral symmetry. The values of the $|\hat{W}_\ell|$ for the five crumpled Platonic-spheres shown in Fig. 2.11 agrees with those of the pure Platonic solids listed in Table 2.5. Similarly, for the cubical-sphere and icosahedral-sphere, we

find the order parameter satisfy

$$\left(a_4^0\right)^2 = \frac{14}{5}|a_4^{\pm 4}|^2, \tag{2.26}$$

with all other $a_4^m = 0$. Such a set of a_4^m is known to maximize $|\hat{W}_4|$ [95, 14, 87]. We will elaborate further on this point in Sec. 2.9.2.

2.8 Hysteresis

Hysteresis refers to the history dependence of a material under an external strain. Hysteresis phenomena occur naturally in many physical systems, ranging from magnetic materials, elastic systems, to electric systems, in which a lag occurs between the application and the removal of a force or field and its subsequent effect. In a system with hysteresis, the output depends in part on the internal state of system and not only on its input. Many systems that exhibit hysteresis will return to precisely the same state after being cycled. For example, magnetic tapes can be re-recorded, vortex clusters can enter and leave superconductors leaving the system in largely the same state it began in and so on. However, there are systems which do not show return point memory. If one bends a table fork too far, it will deform and not spring back to its original shape. Beyond the elastic limit, the fork starts to exhibit hysteresis and repeated cycles introduce work hardening and eventual fracture [88]. The thermodynamic properties of a system are defined completely by the temperature, pressure, etc., and are independent of how the system reached these conditions. Therefore a hysteretic state must be out of equilibrium, or metastable. Also, hysteresis is often associated with first order phase transition in which there is a discontinuity in the

order parameter.

When we apply an external pressure to a thin spherical shell, it will quickly evolve into a polyhedral shape and the shape depends on the mesh type as we showed in the Sec. 2.3. As the external pressure is further increased, we find that beyond a critical point, i.e. buckling pressure, the shell will undergo an abrupt buckling or "snap through" transition that is difficult to reverse. There will be the formation of bulges at the facets of the polyhedral structure. The bulge to the first approximation is like an inverted mirror image of the original shell. Imagine cutting the sphere along a plane and then inverting the cut cap. Then glue it back to the sphere such that there are no discontinuities in the curvature along the rim, and the stretching of the inverted cap is minimized. All the stretching will be concentrated at the bending strip, the ridge of the bulge while the rest of the shell is unstrained [54]. Decreasing the external load again will generally not cause the shell to "pop out back into its undeformed shape, as it can be trapped in a local minimum different than the zero deformation minimum. This "snap-through" transition is therefore hysteretic, much like a first order phase transition [48].

Elastic hysteresis is more pronounced when the loading and unloading is done quickly than when it is done slowly [45]. Some materials such as hard metals do not show elastic hysteresis under a moderate load, while other materials such as rubber exhibit a high degree of elastic hysteresis. In our simulation, we set $\delta p/p_b \sim 5\%$ (p_b is characterize buckling pressure) in order to get a reasonable number of simulation points. In this part of the simulation, we control the pressure instead of the volume in order to get a reasonably spaced set of data. Due to the hysteresis nature of elastic

system, changing the pressure step δp will yield slightly different elastic hysteresis. The hydrostatic pressure p is increased in a stepwise manner δp, with a minimization via gradient descent method at each pressure step. The initial volume of the spherical surface is $V_0 = 1$ and the shell is assumed to be unstrained. The initial spherical thin shell quickly loses stability and evolves toward a polyhedral shape depending on the mesh type. Further increment in pressure leads to more pronounced faceting as we have found in previous sections. However, at a high enough pressure, something dramatic occurs. The crumpled structure becomes more and more unstable and eventually collapses and a "snap-through" transition occurs. This transition happens when the final volume is around 30% of the initial volume V_0. The pressure is then reduced at this point and the cycle is reversed. As the hydrostatic pressure is slowly decreased, the sphere does not return to the inflated condition by the same path in the pressure-volume diagram, but remain "trapped at the collapsed state until the pressure reached values as low as 20% of p_b. For this set of simulations, we use $\kappa = 1$ and $Y = 500$.

2.8.1 icosahedral-sphere

We first consider the most fundamental mesh type, the icosahedral-sphere, also known as the $(P, 0)$ Icosadeltahedral shell. In our simulations, we consider the case $P = 8$, which has 642 vertices, 1920 edges and 1280 facets. The initial spherical shell quickly becomes slightly pointed at the locations of the twelve symmetrically positioned five-fold coordinated points of the triangular mesh. As we increase the pressure, the shell shrinks and becomes more and more faceted, eventually, at a

critical buckling pressure $p_b \sim 220$, the shell becomes unstable and starts to collapse, undergoing a dramatic change in shape, becoming more cubic-like with depressions at six faces of the "cube" as seen in Fig. 2.12. Due to the multiple concave regions that we normally associate with buckling, we identify this sharp transition as a buckling transition. From classical continuum elastic theory, the buckling pressure of a sphere under hydrostatic pressure is $p_b \sim 4\sqrt{\kappa Y}/R^2 \sim 230$. So it is rather amazing that we get very similar numbers for the critical buckling pressure if we think of this "snap-through" transition as a buckling event.

As we reduce the pressure, the shell remains cubic-like with the six bulges becoming less pronounced. Eventually, at some low enough pressure, the bulges pop back out and the shell ceases to have any noticeable concave regions. As we further reduce the pressure, the shell recovers its initial shape. From this, we can conclude that there are four distinct parts to the hysteresis loop, the crumpling phase as we go from shape (1) to (2) (refer to Fig. 2.12); the buckling phase from shape (2) to (4); the relaxation phase from shape (4) to (6) and finally the restoration phase from shape (6) to (8). This size of the elastic hysteresis is approximately 50.

We can analyze the shapes of the deformed shell by looking at the spherical harmonics expansion of the vertices and looking at the various rotational invariant quantities such as Q_ℓ and W_ℓ [113, 95] as defined in the previous section. We will expand the radial density in spherical harmonics using a least square fit up to $L = 16$. From the initial spherical shell, as we increase the pressure, we find that $\ell = 6, 10, 12, \ldots$ modes become more prominent. This is consistent with the results from previous sections. What is surprising is that as the shell becomes more and more

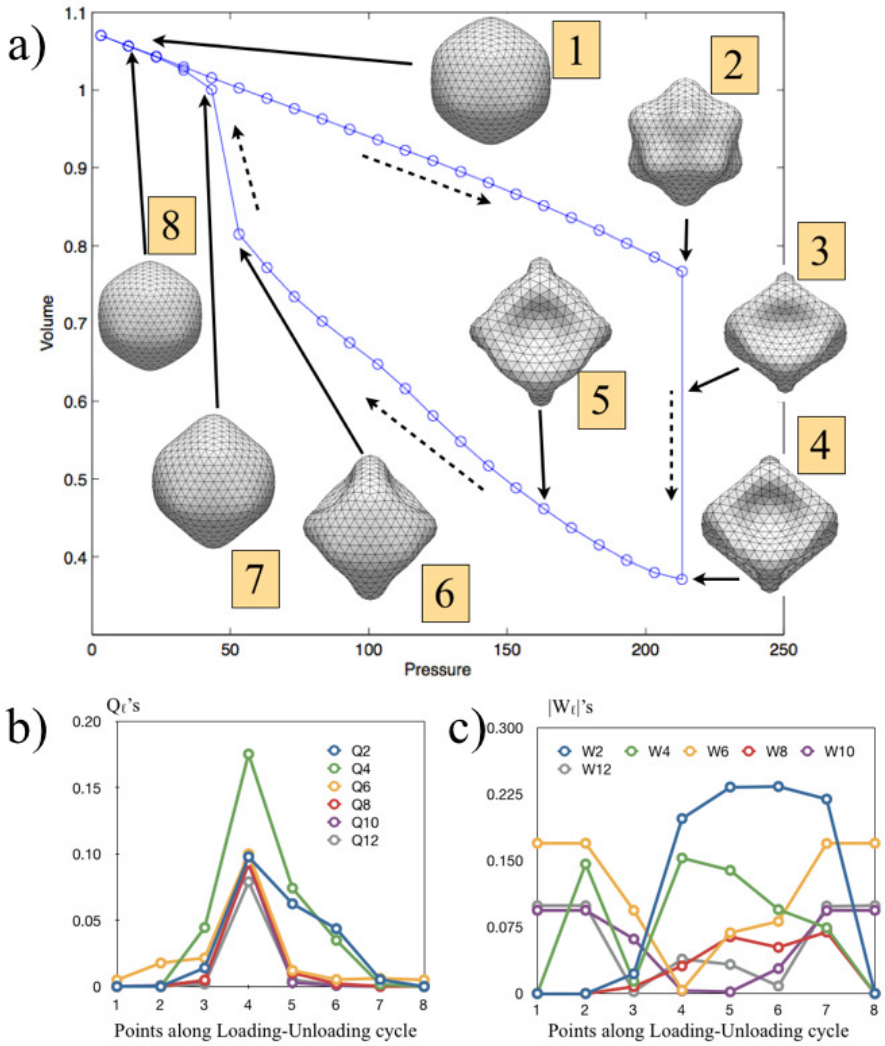

Figure 2.12: (a) P-V response of a crushed icosahedral-sphere. The labels (1) to (8) show the shape of the shell at during loading and unloading. As the pressure is gradually increased from $p = 3$, the shell becomes more faceted as reflected in (2). At the critical buckling pressure $p_b \sim 210$, the icosahedral-like shell undergoes an abrupt collapse into a vastly different looking shell (4). As the pressure is decreased, the shell does not return to the inflated condition by the same path at the pressure-volume diagram, but slowly inflates via a different pathway as reflected by (6) and (7). The dotted arrows denote the direction of the loading-unloading cycle. (b) The values of the normalized $\hat{Q}_\ell$ (according to Eqn. (2.16)) of the icosahedral-sphere at different pressure point of loading-unloading cycle. The various $\hat{Q}_\ell$ grow during the buckling transition, with $\ell = 4$ mode being the most pronounced. The asymmetry of the curves about point (4) reflects the hysteretic behavior of the system. (c) The $\hat{W}_\ell$ (according to Eqn. (2.23)) paint a similar picture. We see significant deviation from icosahedral-symmetry and the emergence of octahedral symmetry

faceted, we start to see the emergence of $\ell = 4, 8, \ldots$ modes, typically associated with octahedral-symmetry as well as the $\ell = 2$ mode which does not belongs to the icosahedral group I, tetrahedral group T or the octahedral group O. During the "snap-through" transition, akin to first order phase transition, these are the modes that are the most excited as seen from Fig. 2.12. From the values of $\hat{Q}_\ell$, it appears that $\ell = 4$ mode is the most enhanced followed by $\ell = 2$ mode. The asymmetry of the curves about point (4) reflects the hysteretic behavior of the system. The $\ell = 2, 4$ modes remain significant even as the hydrostatic pressure is reduced. The $\hat{W}_\ell$ highlight the same picture and we see significant deviation from icosahedral-symmetry at high external pressure and the emergence of octahedral symmetry. At hysteresis point (4), we find that the buckled shell has $|\hat{W}_4| = 0.152948$ and $|\hat{W}_6| = 0.03106$ which are both very close to that of the cube, given by $|\hat{W}_4^{cube}| = 0.159317$ and $|\hat{W}_6^{cube}| = 0.05845$. All these show that there is a spontaneous breaking of icosahedral symmetry during the buckling transition and that there is an emergence of higher order symmetry groups. Also, we see that $|\hat{W}_2| \approx 0.225$ during the return portion of the hysteresis loop. This is some sort of d-wave excitations ($\ell = 2$) mode that emerge during buckling. The hysteresis also exhibit return point memory [88], namely the system returns to the original curve at exactly the same state that it left. The results are summarized in Fig. 2.12.

2.8.2 dodecahedral-sphere

The buckling behavior of the dodecahedral-sphere (also known as the (P, P) Icosadeltahedral shell) is rather different from the icosahedral-sphere. In our case,

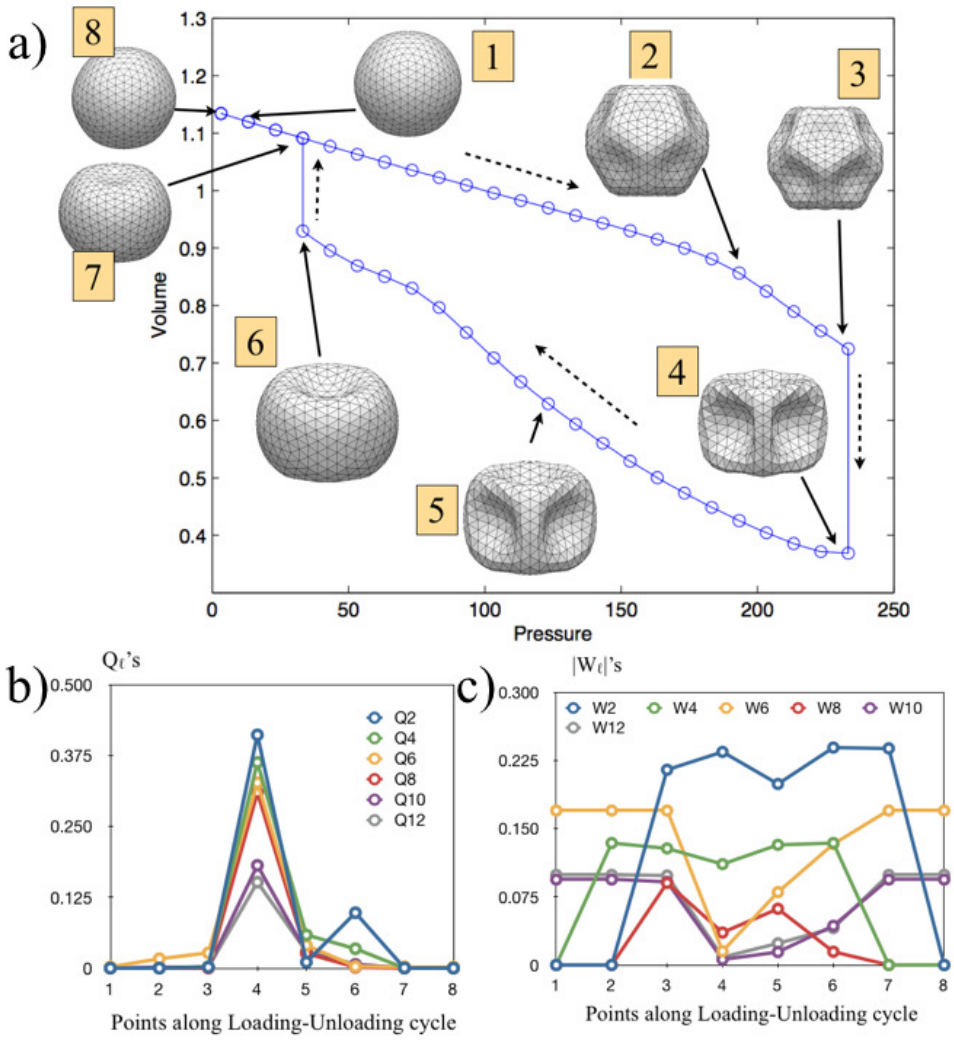

Figure 2.13: (a) P-V response of a crushed dodecahedral-sphere. The labels $(1)-(8)$ show the shape of the shell at different points of the hysteresis. As the pressure is gradually increased from $p = 3$, the shell becomes more faceted as reflected in shapes (2) and (3). At a critical pressure $p_b \sim 230$, the icosahedral-like shell undergoes an abrupt collapse into a vastly different looking shell (4) that resembles a cube. As the pressure is reduced, the number of depressions (bulges) decreased from twelve to six. As the pressure is further decreased, the number of bulges reduces to two as reflected by shape (6). The dotted arrows denote the direction of the LU cycle. (b) The values of the normalized $\hat{Q}_\ell$ (according to Eqn. (2.16)) of the dodecahedral-sphere at different pressure point of LU cycle. The various $\hat{Q}_\ell$ grow during the buckling transition. The asymmetry of the curves about point (4) reflects the hysteretic behavior of the system. At shape (6), we see that there is a spike in the $\ell = 2$ mode. (c) The $\hat{W}_\ell$ (according to Eqn. (2.23)) paint a similar picture. We see significant deviation from icosahedral-symmetry and the emergence of octahedral-symmetry. $|\hat{W}_2|$ stays roughly constant at 0.23 after buckling.

we consider $P = 4$, which has 482 vertices, 1440 edges and 960 facets. The initial spherical shell quickly becomes slightly pointed at the locations of the twelve symmetrically positioned five-fold coordinated points of the triangular mesh. Due to the different orientations of the five fold disclinations ((P, P) icosadeltahedral shell), we get a structure that resembles the dodecahedron. As we increase the pressure, the facets of the shell concave inward, and we see the emergence of twelve bulges as shown in Fig. 2.13. The depressions become more pronounced as we increase the pressure until at a critical buckling pressure $p_b \sim 230$, the shell loses stability and collapses, forming a structure that looks like a cube (label (4)). The number of bulges reduces from twelve to six and they become deeper, resulting in a smaller overall volume. Presumably, the decrease in number of bulges allows for more concave bulges and facilitates a smaller shell volume. As we increase the pressure, the bulges become shallower until eventually four of the bulges disappear and the shell forms a discocyte-like structure. It is axi-symmetrical with two bulges at the north and south poles (label (6)). As the pressure is reduced to the original pressure, the sphere resumes its original form as shown in label (7) of Fig. 2.13. There are four phases in the hysteresis cycle: 1) the crumpling phase as we go from shape (1) to (3) (refer to Fig. 2.13); the buckling phase from shape (3) to (4); the relaxation phase from shape (4) to (6) and finally the restoration phase from shape (6) to (8). The size of the elastic hysteresis is approximately 65 which is larger than the case for the icosahedral-sphere. Due to higher buckling pressure p_b, the hysteresis is larger for the dodecahedral-sphere compared to the icosahedral-sphere.

Our shape analysis of the dodecahedral-sphere under hydrostatic pressure reveals

a similar picture as compared to the icosahedral-sphere as illustrated in Fig. 2.13. During the buckling phase, there is a spontaneous breaking of the icosahedral symmetry and the emergence of other ℓ modes. As evident from Fig. 2.13b, the $\ell = 2, 4, 6, 8$ modes become comparable ($\sim$30%) to $\ell = 0$ mode. The asymmetry of the curves about point (4) reflects the hysteretic behavior of the system. At the shape (6), we see that there is a spike in $\ell = 2$ mode. Fig. 2.13b is even more revealing. As the shell crumple, $|\hat{W}_4|$ went from 0 to 0.13, suggesting the emergence of octahedral/tetrahedral-symmetry. The value of $|\hat{W}_4|$ stays pretty constant at 0.13 along the hysteresis loop except at the start and end points where it is approximately zero. Also, we see that during the buckling transition, $|\hat{W}_6|$ decreases from 0.17 to 0.015 indicating a suppression of icosahedral-symmetry ($|\hat{W}_6^{ico}| = 0.17$) and the emergence of the octahedral-symmetry ($|\hat{W}_6^{cube}| = 0.013$). $|\hat{W}_8|$ stays around 0.05 during buckling, which is fairly close to that of the octahedral/tetrahedral symmetry (See Table 2.5 for complete comparison). Additionally, $|\hat{W}_2| \approx 0.23$ after buckling, similar to what we found for the icosahedral-sphere, indicating the presence of d-wave excitations. Thus, we find that qualitatively, the dodecahedral-sphere display similar hysteretic behavior to the icosahedral-sphere.

2.8.3 cubical-sphere and octahedral-sphere

Let us now consider the cubical-sphere, which has 770 vertices, 2304 edges and 1536 facets. From our simulation, we find that the initial spherical surface quickly becomes cubical. As we reduce the pressure, the shell becomes more and more faceted, with well-defined ridges. As we increase the pressure, the crumpled shape remains

approximately cubical and we do not observe any noticeable buckling behavior. The six evenly distributed bulges become deeper as we increase the pressure resulting in a more shriveled structure. As we decrease the pressure, the shell starts to swell up again, along a different pathway. At a certain pressure, $p \sim 50$, the bulges disappear and the shell becomes globally convex and there is a noticeably jump in the volume. This process is summarized in Fig. 2.14. The hysteresis of the cycle is about 72, which is greater than the previous two cases. There are three distinctive parts to the hysteresis loop: 1) the crumpling phase from label (1) to (3); 2) the relaxation phase from shape (3) to (5) and the restoration (or pop-out) phase from label (5) to (6). There is no buckling phase here as structurally, the shell appears to retain cubical symmetry throughout the cycle. This is a significant departure from the icosahedral-sphere or dodecahedral-sphere, which are manifestly first order transition. Here it appears that the transition is smooth and inherently second order.

The plots of $\hat{Q}_\ell$ and $|\hat{W}_\ell|$ reveal a similar picture as shown in Fig. 2.14. During the crumpling phase, the $\hat{Q}_4$, $\hat{Q}_6$, $\hat{Q}_8$, $\hat{Q}_{10}$ and $\hat{Q}_{12}$ all become more prominent. The most important mode is the $\ell = 4$, which is almost twice as large as the second highest mode $\ell = 8$. However, as we decrease the pressure, all the excited modes decrease in magnitude, as the shell resumes a more spherical shape. $\hat{W}_\ell$ for $\ell = 4, 6, 8, 10$ remain constant throughout the hysteresis cycle and only $\hat{W}_{12}$ show a slight departure from the initial value. This indicate that the shrinking shell retain its cubical symmetry to a high extent through the crumpling process. There is no symmetry group breaking terms such as the $\ell = 2$ term appearing.

The case for the octahedral-sphere is very similar to the cubical-sphere, which is

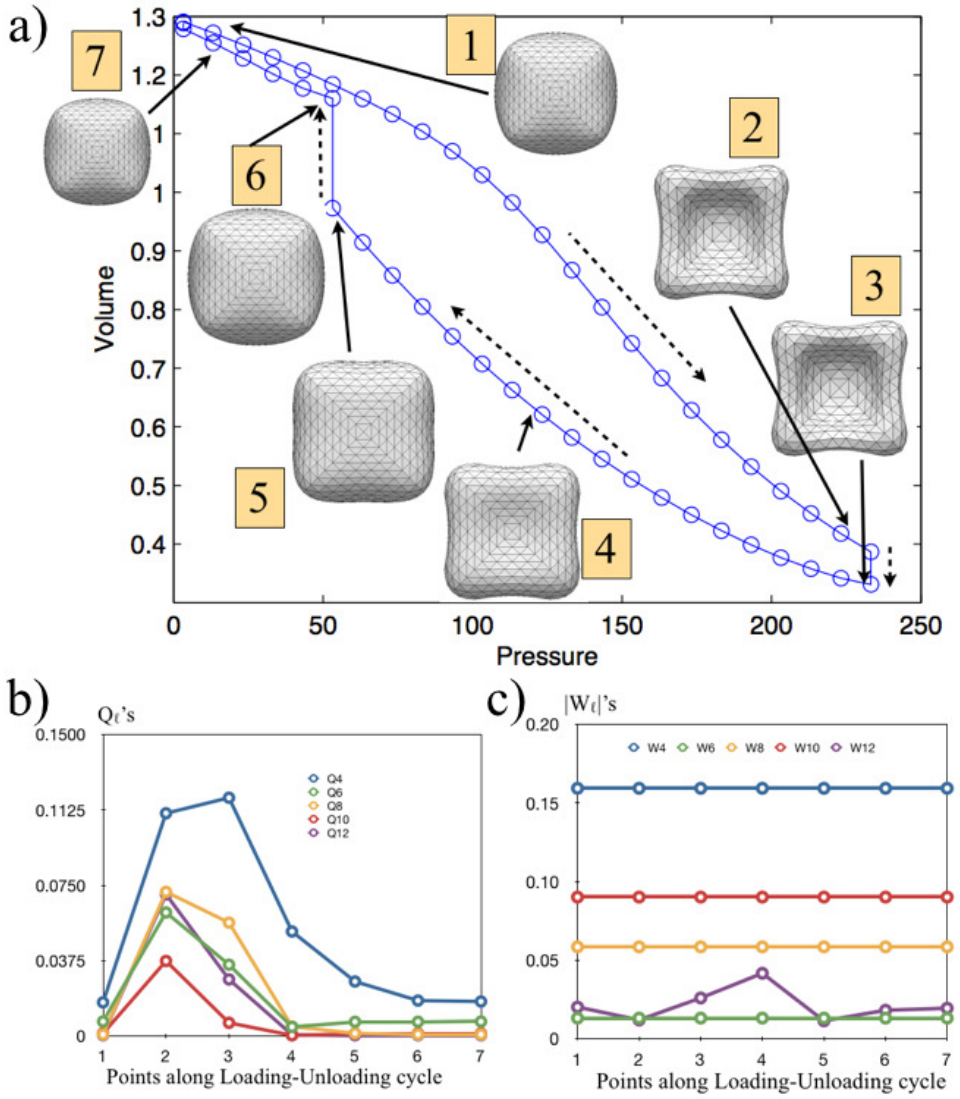

Figure 2.14: (a) P-V response of a crushed cubical-sphere. The shapes (1) – (7) shows the shape of the shell at different points of the hysteresis. As the pressure is gradually increased from $p = 3$, the shell becomes more faceted as reflected in shapes (2) and (3). There is no well-defined buckling pressure as the crumpled shell appears cubical even at high pressures. As the pressure is reduced, the bulges of the shell become shallower (shape (4)) until at shape (5), $p \sim 50$, the bulges "pop" out and the shell becomes globally convex in appearance as we can see from shape (6). The dotted arrows denote the direction of the LU cycle. (b) The values of the normalized $\hat{Q}_\ell$ (according to Eqn. (2.16)) of the cubical-sphere at different pressure point of LU cycle. The various $\hat{Q}_\ell$ grow during the buckling transition, with $\ell = 4$ mode being the most pronounced. The asymmetry of the curves about point (4) reflects the hysteretic behavior of the system. (c) The $\hat{W}_\ell$ (according to Eqn. (2.23)) paint a similar picture. We find that the $\hat{W}_\ell$ for $\ell = 4, 6, 8, 10$ remain fairly constant during the hysteresis cycle and only $\ell = 12$ mode shows any departure from its initial value. The crumpled shell retains its octahedral-symmetry to a high degree and we do not see any $\ell = 2$ emerging.

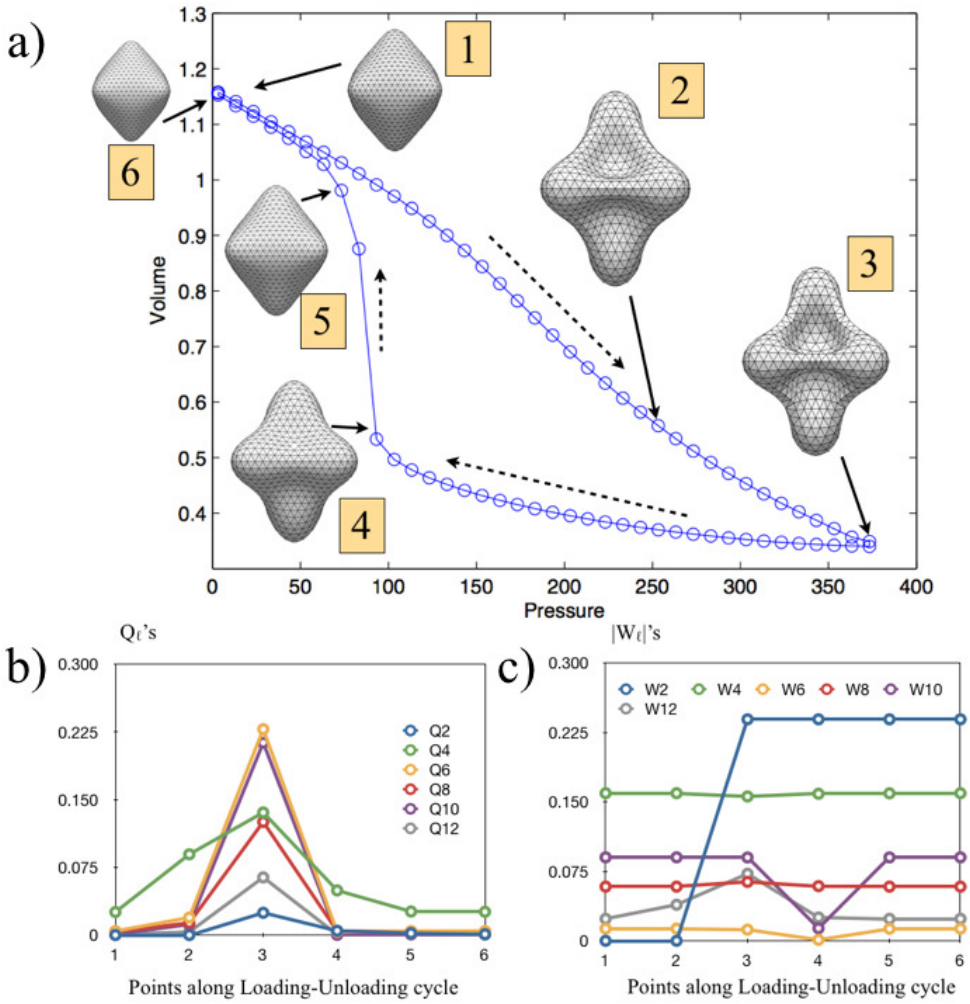

Figure 2.15: (a) P-V response of a crushed octahedral-sphere. The shapes (1) – (6) shows the shape of the shell at different points of the hysteresis. As the pressure is gradually increased from $p = 3$, the shell becomes more faceted as reflected in shapes (2) and (3). There is no well-defined buckling pressure as the crumpled shell appear cubical even at high pressures. As the pressure is reduced, the bulges of the shell become shallower (shape (4)) until at shape (5), $p \sim 80$, the bulges "pop" out and the shell becomes convex in appearance. The dotted arrows denote the direction of the LU cycle. (b) The values of the normalized $\hat{Q}_\ell$ (according to Eqn. (2.16)) of the octahedral-sphere at different pressure point of LU cyclethe various $\hat{Q}_\ell$ grow during the buckling transition, with $\ell = 4$ and 10 modes being the most pronounced, followed by $\ell = 4$ and 8. We do see $\ell = 2$ mode appear although its effect appear to be relatively small. (c) The $\hat{W}_\ell$ (according to Eqn. (2.23)) paint a similar picture. We see small deviation from octahedral-symmetry and the emergence of d-wave modes ($\ell = 2$). $|\hat{W}_2| \approx 0.0225$ throughout the crumpling process.

unsurprising since they are dual to one another. The mesh we used has 1026 vertices, 3072 edges and 2048 facets. The spherical shell quickly becomes octahedral-like in shape at the start of the simulation, consistent with what we observed in the previous section. As we reduce the pressure, the shell retains the octahedral symmetry, and we see eight triangular bulges appear symmetrically on the surface. As the pressure is further increased, the bulges become deeper, facilitating a smaller volume. There is no noticeable buckling behavior as the shell remains octahedral-like throughout. As we go the opposite sense in the hysteresis loop (decreasing pressure), the shell starts to swell up and the depressions become shallower and at $p \sim 80$, the depressions disappear as the volume jumped significantly and all the concave regions disappear from the shell. The whole hysteresis loop is summarized in Fig. 2.15. In terms of the $\hat{Q}_\ell$, we find that the most important modes are $\ell = 6$ and 10 followed by $\ell = 4$ and 8. We do see $\ell = 2$ mode appear although its effect appear to be relatively small compared to the other modes as seen in Fig. 2.15b. For the case of $|\hat{W}_\ell|$, we find that $|\hat{W}_4|$, $|\hat{W}_6|$ and $|\hat{W}_8|$ remain fairly constant during the whole hysteresis cycle. As the shell becomes crumpled, we see the simultaneous emergence of $|\hat{W}_2| \approx 0.225$ and the reduction in $|\hat{W}_{10}|$ and $|\hat{W}_{12}|$. We see small deviation from octahedral-symmetry and the emergence of d-wave modes ($\ell = 2$).

Comparing the hysteresis effect of the octahedral-sphere and cubical-sphere, we see that qualitatively they are very similar as both shells manifestly exhibit octahedral symmetry during crumpling and the shells maintain high degree of octahedral-symmetry throughout the hysteresis cycle as seen from the constant values in $|\hat{W}_\ell|$ (See Fig. 2.14 and 2.15). The only significant deviation is that for the octahedral-

sphere, we see the emergence of $\ell = 2$ mode, which is absent in the cubical-sphere.

2.9 Landau Theory

2.9.1 Order Parameter

The results discussed empirically in Sec. 2.8 can be understood more easily in the context of Landau's general theory of phase transition [42, 72, 95]. As explained in Sec. 2.7, the radial density can always be expanded in the spherical harmonics, which form a complete set of functions on the unit sphere:

$$D(\theta, \phi) = \sum_{\ell=0}^{\infty} \sum_{m=-\ell}^{\ell} a_\ell^m Y_\ell^m(\theta, \phi).$$

For the initial sphere, which is a perfect sphere, all the a_ℓ^m except a_0^0 are zero. As the shell crumple, some of the a_ℓ^m for $\ell \neq 0$ will become non-zero. A shell with a broken spherical symmetry is characterized by some smallest value of $\ell_* > 0$ for which $a_\ell^m \neq 0$:

$$\begin{aligned} \delta D(\theta, \phi) &= D(\theta, \phi) - a_0^0 Y_0^0 \\ &\approx \sum_{m=-\ell_*}^{\ell_*} a_{\ell_*}^m \, Y_{\ell_*}^m(\theta, \phi) + \cdots , \end{aligned} \tag{2.27}$$

where the ellipsis stands for higher order harmonic terms. This set of $a_{\ell_*}^m$ can be thought of as a rotational order parameters that forms a $(2\ell_* + 1)$-dimensional order parameter describing the low-temperature phase (or equivalently low-pressure phase since $p \propto T$).

2.9.2 Simplest Landau model

We can write down the simplest Landau free energy describing the departure from spherical symmetry involving rotationally invariant combinations of $\{a_\ell^m\}$ [42, 72, 95, 14]:

$$F_\ell = r_\ell \sum_{m=-\ell}^{\ell} |a_\ell^m|^2 + w_\ell \sum_{m_1+m_2+m_3=0} \begin{pmatrix} \ell & \ell & \ell \\ m_1 & m_2 & m_3 \end{pmatrix} a_\ell^{m_1} a_\ell^{m_2} a_\ell^{m_3} + O(a_\ell^m)^4, \quad (2.28)$$

where r_ℓ and w_ℓ are pressure-dependent parameters. From hereon, we will drop the asterisk in the ℓ for brevity. We see that the first term is proportional to Q_ℓ and the second term is proportional to W_ℓ. Assuming that the second-order coupling $r_\ell(p)$ becomes negative with decreasing pressure, then eventually F_ℓ will be minimized by a state such that

$$a_\ell^m \neq 0$$

at low pressures when the first term in (2.28) dominates the free energy landscape. Recall that the rotationally invariant quantity

$$\sum_{m=-\ell}^{\ell} |a_\ell^m|^2 \propto Q_\ell^2,$$

measures the "magnitude" of the $(2\ell+1)$-dimensional order parameter so the first summation in (2.28) is always positive and the sign depends on the sign of the $r_\ell(p)$. If the third-order coupling w_ℓ is nonzero, Landau theory predicts that the transition to this state will be first order [95, 20]. If we fixed the magnitude Q_ℓ, we can ask what are the preferred states. If the transition is weakly first order, then the preferred state can be found by minimizing the third order term in (2.28), with the second order term held fixed.

Thus, the problem reduces to finding extrema of the symmetry invariant $\hat{W}_\ell$. If w_ℓ is positive, then we need to minimize $\hat{W}_\ell$; conversely, if w_ℓ is negative, then we need to maximize $\hat{W}_\ell$. In general, the sign of $\hat{W}_\ell$ depends on the sign of $\hat{a}^0_\ell$, which depends on the coordinate system we used to perform our spherical harmonics expansion (See Eqn. (2.24)). The problem of finding the extrema of $\hat{W}_\ell$ has been investigated in the context of patterns in fluid convection in spherical shell [14, 87] and in bond orientation order in liquids and glasses [95] and we will just summarize the relevant results here.

The trivial solution of Eq. (2.23) for any given ℓ is the spherical solution

$$a^0_\ell = 1, \quad a^m_\ell = 0 \quad \text{otherwise.} \tag{2.29}$$

The magnitude of $\hat{W}_\ell$ in this case is given by:

$$\hat{W}^{trivial}_\ell = 2^{-\frac{1}{2}+\ell}\sqrt{\pi}\sqrt{\frac{2^{-2\ell}\left(-\frac{1}{2}+\frac{\ell}{2}\right)!\frac{3\ell}{2}!}{\left(\left(-\frac{1}{2}-\frac{\ell}{2}\right)!\right)^2\left(\frac{\ell}{2}!\right)^3\left(\frac{1}{2}+\frac{3\ell}{2}\right)!}}. \tag{2.30}$$

However, the trivial solution is not the one realized physically since there are other solutions with larger values of $\hat{W}_\ell$.

For the case of $\ell = 2$, the relevant extrema is the axisymmetric solution with all the a^m_2 real and that

$$\left(a^{\pm 1}_2\right)^2 = \frac{1}{3}(1+a^0_2)(1-a^0_2) \quad \text{and} \quad a^{\pm 2}_2 = \frac{1}{\sqrt{6}}(1-a^0_2). \tag{2.31}$$

This is a one parameter family of solution in a^0_2 and the magnitude of $\hat{W}_2$ is given by

$$|\hat{W}^{axi}_2| = 0.239046, \tag{2.32}$$

which is independent of a^0_2.

For $\ell = 4$, the extrema of interest is the cubic solution with all the a_4^m real and

$$(a_4^0)^2 = \frac{14}{5}|a_4^{\pm 4}|^2 \quad \text{nonozero}, \quad a_4^m = 0 \quad \text{otherwise.} \tag{2.33}$$

This solution subspace is spanned by a_4^0 and $a_4^{\pm 4}$. If $a_4^0 > 0$, then the extrema is a maximum, otherwise, the extrema is a minimum. The maximum corresponds to the cubic symmetry while the minimum us associated with its "dual", the octahedron. The magnitude of $\hat{W}_4$ is given by

$$|\hat{W}_4^{cube}| = 0.159317, \tag{2.34}$$

in agreement with the values we found for the cube as listed in Table 2.5.

For the case $\ell = 6$, there are two extrema that are relevant. The first is the icosahedral solution that is spanned by real-valued a_6^0 and $a_6^{\pm 5}$ with all other $a_6^m = 0$ and they obey the relation

$$\left(a_6^0\right)^2 = \frac{11}{7}|a_6^{\pm 5}|^2. \tag{2.35}$$

The magnitude of $\hat{W}_6$ is given by

$$|\hat{W}_6^{ico}| = 0.169754, \tag{2.36}$$

in agreement with what we found for the icosahedron. In this special coordinate system, we find that if $a_6^0 > 0$, then the extrema is a maximum, which display "icosahedral" symmetry. Conversely, if $a_6^0 < 0$, then the extrema is a minimum and it corresponds to "dodecahedral" symmetry [95]. However, if we used a different coordinate system, then the meaning of the sign of the $\hat{W}_6$ becomes less clear. For example, using the spherical harmonics expansion of Onaka's formula for Platonic solids in equation (2.14), we find that $\hat{W}_6^{ico} = \hat{W}_6^{ico} = -0.169754$ and the sign loses its meaning.

On the other hand, if we consider the "cubic" solution spanned by a_6^0 and $a_6^{\pm 4}$ with all other $a_6^m = 0$, the extrema is satisfied when

$$\left(a_6^0\right)^2 = \frac{2}{7}|a_6^{\pm 5}|^2, \tag{2.37}$$

and the corresponding $\hat{W}_6$ is given by

$$|\hat{W}_6^{cubic}| = 0.013161. \tag{2.38}$$

These two configurations are shown by Busse [14] to be extrema in the full 13-dimensional space of $\ell = 6$ spherical harmonics and has further conjectured that $|\hat{W}_6^{ico}|$ is a global maximum of $|\hat{W}_6|$.

2.9.3 Coupling between Order Parameters

We see that Eq. (2.28) is reasonably adequate at describing the "crumpling" phase of the shell but is totally inadequate in describing the "buckling" phase, where there are a few ℓ's, say ℓ_1 and ℓ_2 that are equally important, with possible couplings between them. In this case, the most general Landau free energy one can write is for a system with two distinct ℓ is

$$F = F_{\ell_1} + F_{\ell_2} + F_{\ell_1,\ell_2} + F_{\ell_2,\ell_1} + \cdots, \tag{2.39}$$

where F_ℓ is given by Eq. (2.28), ellipsis refers to higher order harmonic terms that are neglected and

$$F_{\ell_i,\ell_j} = w_{\ell_i,\ell_j} \sum_{m_1+m_2+m_3=0} \begin{pmatrix} \ell_i & \ell_i & \ell_j \\ m_1 & m_2 & m_3 \end{pmatrix} a_{\ell_i}^{m_1} a_{\ell_i}^{m_2} a_{\ell_j}^{m_3}. \tag{2.40}$$

The parameter w_{ℓ_i,ℓ_j} measures the coupling between the modes ℓ_i and ℓ_j. The presence of the coupling term F_{ℓ_i,ℓ_j} means that nonzero ℓ_i spherical harmonics can act like an ordering field which couples linearly to the $a_{\ell_j}^m$, generating ℓ_j modes if these are not already nonzero.

This expression (2.39) can be generalized easily to more spherical harmonics. In general, if there are n distinct ℓ's, namely, $\ell_1, \ell_2, \ldots \ell_n$, the most generally Landau free energy expression one can write down is

$$F = \sum_i F_{\ell_i} + \sum_{i \neq j} F_{\ell_i,\ell_j} + \cdots . \tag{2.41}$$

where there are at most $n + n(n-1) = n^2$ terms. The coupling terms F_{ℓ_i,ℓ_j} are nonzero only when the Wigner selection rules given by (2.19), (2.20), (2.21), (2.22) are satisfied, so in general, some of the $n(n-1)$ coupling terms may vanish.

For simplicity, let us we consider a simple system with two different ℓ's, say $\ell_1 = 4$ and $\ell_2 = 6$, similar to an earlier work [95]. The most general Landau free energy is

$$F = F_4 + F_6 + F_{6,4} + F_{4,6}, \tag{2.42}$$

where there is coupling between $\ell = 6$ mode and $\ell = 4$ mode. Suppose that the crumpled shell initially only has $\ell = 6$ mode and that $a_4^m = 0 \; \forall m$. The authors in [95] noted that nonzero a_4^m can still be generated even if they do not minimize the corresponding free energy F_ℓ. The presence of the coupling term $F_{6,4}$ means that nonzero $\ell = 6$ spherical harmonics can act like an ordering field which couples linearly to the a_4^m, generating $\ell = 4$ modes if these are not already nonzero. In order to prevent this type of feedback mechanism, the $\ell = 6$ spherical harmonics must

satisfy $2(4)+1=9$ nonlinear equations, namely,

$$\sum_{m_1(m_1+m_2=-m)}\sum_{m_2}\begin{pmatrix}6 & 6 & 4\\ m_1 & m_2 & m\end{pmatrix}a_6^{m_1}a_6^{m_2}=0,\quad m=0,\pm1\cdots\pm4. \tag{2.43}$$

These nine constraints completely specify the $\ell=6$ spherical harmonics, up to an arbitrary rotation (3 degrees of freedom) and an overall amplitude (1 degree of freedom), i.e. $9+3+1=2(6)+1=13$. Similar argument works for the reverse case where we start with a crumpled shell with only nonzero $\ell=4$ mode and vanishing $\ell=6$ mode, except here $F_{4,6}$ leads to $2(4)+1=9$ constraints.

Interestingly, if we consider the set of icosahedral harmonics that maximizes $\hat{W}_6$ defined by Eq. (2.35), we find that Eq. (2.43) is satisfied. Incidentally, the icosahedral harmonics do not generate $\ell=2$ mode since they satisfy the five nonlinear equations:

$$\sum_{m_1(m_1+m_2=-m)}\sum_{m_2}\begin{pmatrix}6 & 6 & 2\\ m_1 & m_2 & m\end{pmatrix}a_6^{m_1}a_6^{m_2}=0,\quad m=-2,-1,0,1,2. \tag{2.44}$$

Therefore, if we consider the icosahedron (solid), we find that all the coupling terms are irrelevant and we can describe the Icosahedron by

$$F=F_6+F_{10}+F_{12}+\ldots. \tag{2.45}$$

However, we do not expect this kind of miraculous cancelation to occur on any regular basis and that in general, for any crumpled surface, we do expect to see some of the coupling terms to become relevant..

From this example, we see that, say we are interested in the ℓ_i spherical harmonics, in order to not have feedback coupling between ℓ_i and ℓ_j mode, a necessarily condition

is for the set of spherical harmonics $\{a_{\ell_i}^m\}$ to satisfy the $2(\ell_j)+1$ nonlinear constraints:

$$h_{\ell_i,\ell_j}^m = \sum_{m_1(m_1+m_2=-m)} \sum_{m_2} \begin{pmatrix} \ell_i & \ell_i & \ell_j \\ m_1 & m_2 & m \end{pmatrix} a_{\ell_i}^{m_1} a_{\ell_i}^{m_2} = 0, \quad m = 0, \pm 1, \ldots, \pm \ell_j. \tag{2.46}$$

This will lead to the vanishing of the coupling term F_{ℓ_i,ℓ_j} in the Landau Free energy since

$$F_{\ell_i,\ell_j} = w_{\ell_i,\ell_j} \sum_m h_{\ell_i,\ell_j}^m a_{\ell_j}^m = 0. \tag{2.47}$$

Alternatively, even if the $2(\ell_j)+1$ nonlinear constraints given by (2.46) are not fully satisfied, the coupling term can still vanish if the summation of all the nonzero h_{ℓ_i,ℓ_j}^m vanishes:

$$F_{\ell_i,\ell_j}/w_{\ell_i,\ell_j} = \sum_m h_{\ell_i,\ell_j}^m a_{\ell_j}^m = 0. \tag{2.48}$$

Suppose we have a system with n distinct ℓ's and we would like to only consider certain couplings, then we need to write down a few sets of $2\ell+1$ constraints and in general, we will have many different sets of algebraic solutions that satisfy these equations (up to rotations and amplitude) and in the rare case where we have only 4 degrees of freedom in each of the $2\ell_i+1$ manifolds, then will we get a unique solution.

Let us now consider the hysteresis of the icosahedral-sphere and try to construct a simple Landau model that can describe the symmetry breaking process. A careful analysis of the icosahedral-sphere shows that in fact h_{ℓ_i,ℓ_j}^m are generally nonzero as we traverse the hysteresis loop so that the constraints given by (2.46) are not satisfied. However, it may be that there might exist miraculous cancelation with the h_{ℓ_i,ℓ_j}^m such that Eqn. (2.48) is satisfied, resulting in a simpler Landau model. Our calculations show that this is not the case and the result is summarized in Fig. 2.16. The coupling

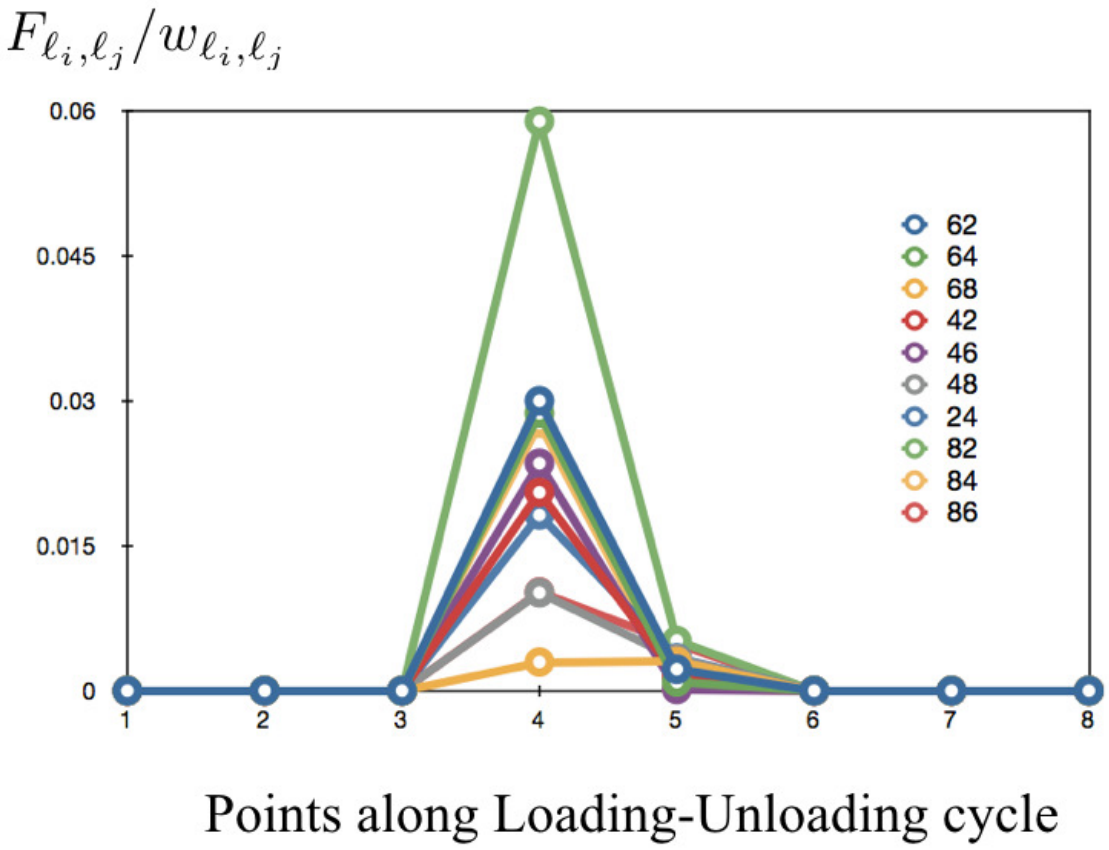

Figure 2.16: The coupling term given by Eqn. (2.48) is plotted for the various points along the loading-unloading cycle of the icosahedral-sphere (Refer to Fig. 2.12). We see that the coupling terms are initially zero and become nonzero during the buckling phase (points 3-5), a signature of the symmetry breaking. As we move to the relaxation phase (5-6), the values of the coupling terms become greatly diminished and they vanish completely during the restoration phase.

terms F_{ℓ_i,ℓ_j} become during the buckling and relaxation phase and vanishes during the crumpling and restoration phase. Therefore, we find that we cannot simplify the Landau free energy and it is necessarily of the form given by Eqn. (2.41) with $\ell = 2, 4, 6, 8, 10, 12, \ldots$.

2.10 Conclusion

The shrinking of spherical crystal lattices (frozen defects) with different topological defects satisfying Euler-Poincaré formula in the frozen topography ($\tau_{defect}/\tau_{surface} \gg 1$) limit is studied. The shape of the crumpled shells depend sensitively on the number and types of disclinations on the lattice. Shells with only one type of disclination were found to crumple into shapes that resembles that of the Platonic solids. Spherical lattices with multiple types of disclinations deformed into more complex structures and sites with greater topological charge have a tendency to bend/buckle more. We analyzed the the energies of the crumpled shells formed from Platonic solids and found that although the icosahedral-sphere is initially the most stable, it does not remain the lowest energy state during the full process of shrinking and will undergo structural transition pathways into other lattice type. By changing the thickness of the shell, the radius of the sphere and the lattice spacing, we explored the phase space of the crumpled spheres belonging to the Platonic solids and found striking similarities in the different phase diagrams suggesting that different spherical lattices have the same qualitative behavior under shrinking. We present a satisfying way to classify spherical crystal lattice based on listing the number and type of disclinations, the full symmetry group of the defects and a generalized "Casper-Klug" coordinates. Elastic systems

often exhibit hysteresis and we studied the hysteresis in the five Platonic shells and found that for the icosahedral-sphere, dodecahedral-sphere and octahedral-sphere, there is a spontaneous symmetry breaking with the appearance of $\ell = 2$ mode and other symmetry related modes during the buckling process. The icosahedral-sphere and dodecahedral-sphere appear to have a well-defined"snap-through transition, much like a first order phase transition; the cubical-sphere and octahedral-sphere appear to have no snap-through transition and is much like a second order phase transition. Lastly, we presented a Landau free energy model that captures the shape changing symmetry breaking transition of the shell during hysteresis.

Throughout this work, we made the key assumption that we are working in the regime where the core energies of the defects are large and so the spherical shell prefers to have the minimum number of disclinations. When the core energies is small, the number of defects will proliferate and it is something we hope to understand better in the future. Studies in topological defects have been done primarily either in the limit of frozen defects (as in this paper) or frozen topography. The intermediate case where defects and topology are both allowed to vary, i.e. $\tau_{defect}/\tau_{surface} \sim 1$ has only been investigated in one work [51] and it is an area of research that is largely untapped. Here is a *Gedankenexperiment* that we ponder. Suppose we have some topological defects on a spherical shell and they are evenly spaced along a Riemannian circle that contains the North and South pole. This great circle divides the sphere into two equal caps. Imagine that a cylindrical portion starts to continuously grow between the two caps so the sphere is slowly deformed into a elongated pill-like shape. If the defects are allowed to move as the geometry of the surface deformed, do the defects prefer

to migrate to the cylindrical region (zero Gauss curvature) or the spherical region (non-zero Gauss curvature)? We can even add an interesting twist to this thought experiment. When this elongated pill reaches a critical length, it start to bend in the equatorial plane such that it form a torus-like ring. Now there are regions of positive, zero and negative Gauss curvature [100]. How will the defects distribute themselves?

Chapter 3

Physical basis of the bacterial spore coat architecture and its relation to the elastic

3.1 Introduction

Bacillus spores are highly resistant dormant cells formed in response to starvation. The spore is surrounded by a structurally complex protein shell, the coat, which protects the genetic material while permitting the diffusion of water and small molecules to the spore interior [27, 43, 26, 103]. In spite of its dormancy, once nutrient is available the spore is able to resume metabolic activity and return to vegetative growth, a process requiring the coat to be shed. Spores dynamically expand and contract in response to humidity, demanding the coat be flexible [105, 25]. Despite the coats critical biological functions essentially nothing is known about the design principles that

allow the coat to be tough but also flexible and, when metabolic activity resumes, to be efficiently shed. Here, we investigated the hypothesis that these apparently incompatible characteristics derive from an adaptive mechanical response that endows them simultaneously with strength and pliancy as well as the capacity to be shed rapidly.

A simple theoretical model of the coat allows us to understand the folding patterns seen in bacterial coats. Furthermore, we show how the spore architecture and mechanical properties prevent coat shedding until the cell volume increases past a threshold associated with a critical cell size preceding the first cell division. Consistent with this prediction, it has been found that coat shedding does not occur when the cell volume expansion is inhibited using antibiotics. These results suggest that the bacterial spore coat has adapted mechanically to serve several critical functions including regulating the release of the outgrowing cell. The spore and its protective coat represent a simple paradigm likely used in diverse cell types [28] where regulated flexibility of a surface layer is adaptive, and may inspire novel applications for controlled release of materials.

Bacillus spores consist of multiple concentric shells encasing dehydrated genetic material at the center (the core). One of these shells is a loosely cross linked peptidoglycan layer, called the cortex, surrounding the core. Encasing this is the coat, which exhibits a unique folding geometry (Fig. 3.1a-c). Paradoxically, the coat must be chemically resilient and physically tough but still possess significant flexibility in responding to environmental stimuli [43, 26, 105, 25, 19, 79, 104, 80, 44]. During germination, the coat must be broken apart so it can be rapidly shed [89].

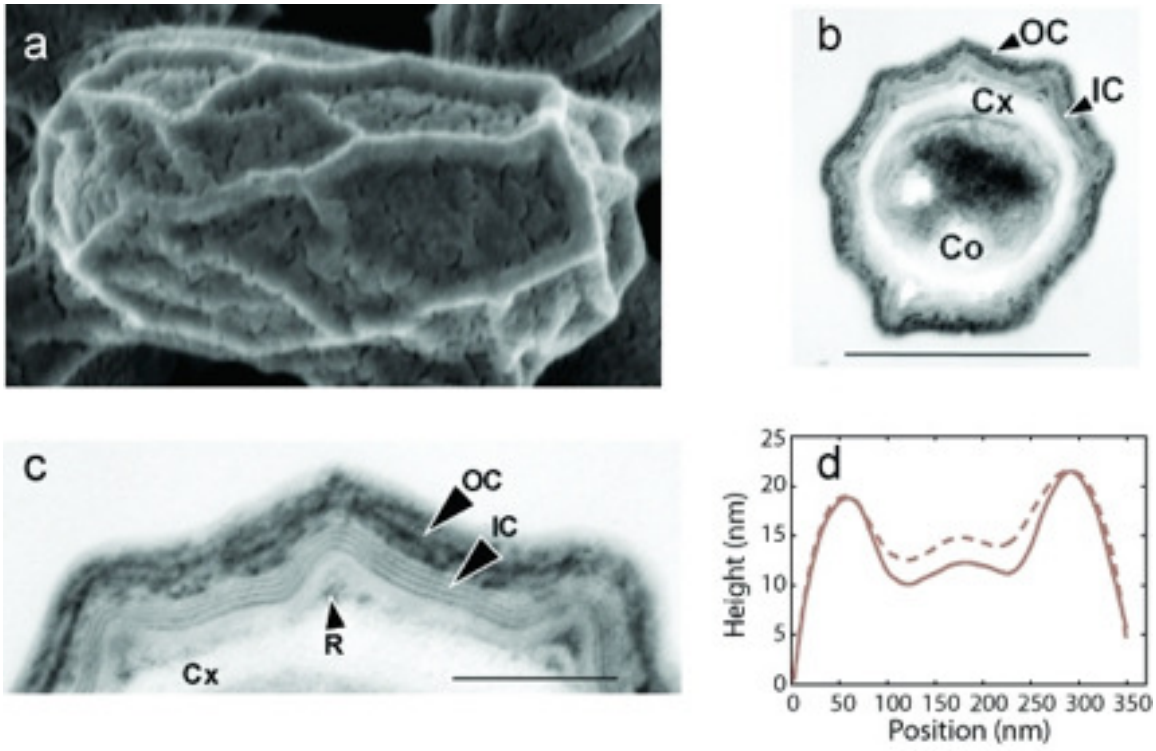

Figure 3.1: Morphology of the B. subtilis spore. Wild type (strain PY79) spores were analyzed by SEM (a), TEM17 (b, c) or AFM (d). c is a magnification of part of b. Cortex (Cx), coat (Ct) and a ruck (R) are indicated in panels b and/or c. (d) Height profiles measured across the short axis of a spore are recorded at low (35%, solid) and high (95%, dashed) relative humidity depict partial unfolding of the wrinkles at high relative humidity. To plot the two curves as close as possible, an offset is added to the height profile at low relative humidity because the overall height of the spore increases with relative humidity. The size bars indicate (a, c) 250 nm or (b) 500 nm.

The ridges of the B. Subtilis coat emerge during the process of sporulation in which water is expelled from the spore core and cross links occur in the cortex. The mature spore is not static. It expands and contracts in response to changes in relative humidty [105, 25]. The height profiles of a B. Subtilis in Fig. 3.1d show that a partial unfolding of the ridges accompanies the expansion of the spore at high humidity.

Although ridges are present in many if not most species [19, 12, 11] of the Bacillus genus, they are very poorly understood; we do not understand the forces guiding their formation, how their topography is influenced by the coats materials properties or their biological function, if any. To address these questions, we first considered that ridges could emerge spontaneously, as in the case of wrinkles that form when a thin layer of material that adheres weakly to a support is under compression [18]. The coat and cortex form such a system, because the core volume (and, therefore, its surface area) decreases during sporulation [86].

Rucks can form if the stress in the system overcomes the adhesive forces between the coat and the underlying cortex [52]. The critical size of a ruck in 2-dimension can be estimated in two ways. Firstly, let us consider the size of a ruck in soft, extensible films that adhere to a substrate as shown in Fig. 3.2b. The energy per unit width of the film of length ℓ is

$$W = U_a + U_b + U_c$$

where $U_a \sim J\ell$ is the adhesive energy, $U_b \sim (Eh^3)\Delta^2/\ell^3 \sim (Eh^3)\epsilon/\ell^2$ is the bending energy and $U_c \sim (Eh)\epsilon^2/\ell$ is the compressive strain energy (h is the thickness of the film). The longitudinal displacement ϵ is related to the lateral displacement Δ via $\Delta \sim (\epsilon\ell)^{1/2}$. Minimizing $W(\epsilon, \ell)$ with respect to ϵ and ℓ yields scaling laws for the

critical compression

$$\epsilon_c \sim (Jh^3/E)^{1/4} \tag{3.1}$$

required to form a ruck of critical size

$$\ell_c \sim (Eh^5/J)^{1/4}. \tag{3.2}$$

The elastic modulus of the spore coat is measured using an atomic force microscope to be around 12 GPa. Using the typical dimensions of a spore ruck $\ell_c \sim 100$nm, $\Delta \sim h \sim 40$nm, we estimate that $\epsilon \sim 16$nm and $J \sim 12$ N/m. So we expect the amount of compression to be $\epsilon/\ell \sim 9\%$.

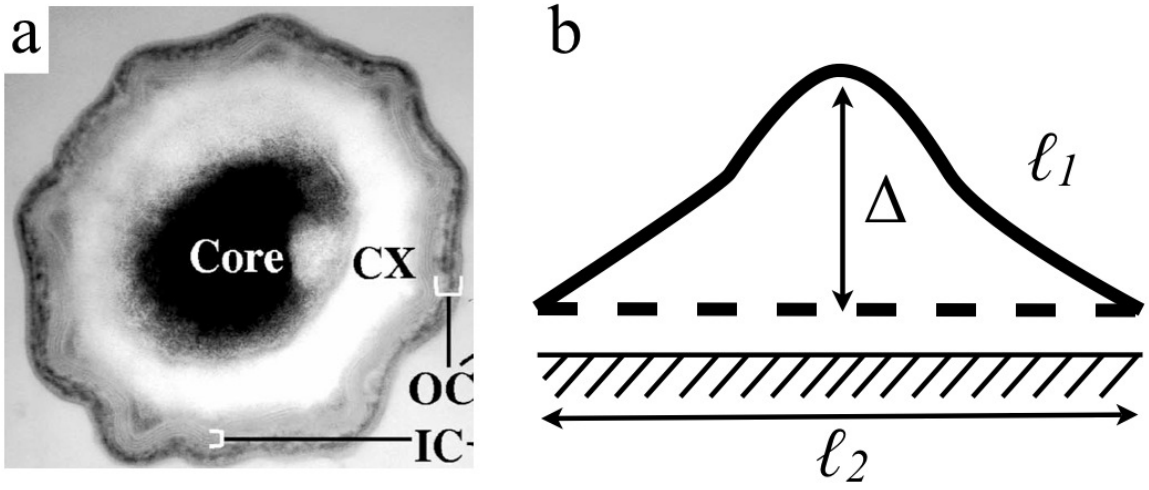

Figure 3.2: (a) SEM image of *B. subtilis*. CX: cortex, IC: Inner spore Coat, OC: Outer spore Coat. We make no distinction between the inner and outer coat in our modeling. (b) A thin ruck on a flat adhesive substrate of height Δ and length ℓ_1. For the extensible elastica, $\ell_1 = \ell + \epsilon$, where the original length of the elastica is $\ell_2 = \ell$ as indicated by the dotted line and ϵ is the amount the elastica is stretched. For the inextensible elastica under stress, $\ell_1 = \ell$ and $\ell_1 = \ell - \epsilon$. $\Delta \sim (\epsilon\ell)^{1/2}$ for either model.

Alternatively, if we assume that the film is inextensible and is compressed an amount ϵ by an applied stress F in the longitudinal direction, then the energy per unit width of the film of length ℓ is $W = U_a + U_b + U_c$ where $U_a \sim J\ell$ is the adhesive

energy, $U_b \sim (Eh^3)\epsilon/\ell^2$ is the bending energy and $U_c \sim F\epsilon$ is the energy due to the applied force. Minimizing $W(\ell)$ with respect to ℓ yields scaling law for the critical ruck size

$$\ell_c \sim (Eh^3\epsilon/J)^{1/3}. \tag{3.3}$$

Under the same parameters as before, we find that this model predicts that $J \sim$ 30N/m. The energy of adhesion between the coat and the cortex, associated with nonspecific electrostatic interactions between the positively charged cortex peptidoglycan [66] and the negatively charged coat [22], was measured to be $J \sim$10 Joules/m^2, so either model gives reasonable approximations.

3.2 Numerical Simulations

In order to simulate ruck formation when the spore shrinks, we model the spore as two concentric rings (or polygons) of radii R_1 and R_2 that are comprised of N edges and N vertices. This model is based on our analysis of the cross section of the bacteria spore as shown in Fig. 3.1 and 3.2a, which shows that the cross section of the cortex appear roughly circular while the coat appear to form many rucks along the circumference. The SEM images show that there are delamination along the circumference of the cross section of the bacteria spore during dehydration. The formation of rucks along the circumference will explain the emergence of the ridges along the long axis of the bacteria.

The outer polygon models the coat while the inner polygon models the core and cortex. For each vertex on the inner polygon there is a corresponding vertex on the outer polygon, lying on the same radial line. The polygon asymptotes a circle as

N increases. In the simulation, the inner polygon oscillates sinusoidally between the initial radius R_1 and minimum radius R_2. We did not allow bending and stretching. This periodic motion is suppose to simulate the cyclical expansion and contraction of a bacteria spore due to changes in humidity as observed in experiments. Again, from SEM images, we see that the cross section of core remains circular during expansion and contraction and hence, we picked a simple motion in our numerical simulations. Thus, each cortex vertex oscillates between R_1 and R_2 with a characteristic period T_c. The outer polygon, modeling the coat, has more complex mechanical behavior. In addition to the bending and stretching energy associated with the elastic extensible ring [54], we added substrate energy between the two concentric rings to model the adhesion force between the coat and cortex, which is Hookean and of finite range. Finally, we added a shearing penalty between the two layers to prevent the two polygons from sliding relative to one another.

We calculated the response of this structure to gradual reductions in volume using a combination of scaling analyses and numerical simulations, restricting ourselves to two dimensions, both because the wrinkle morphology is that of long ridges along the spore, and in order to focus on a minimal model. The inner polygon is allowed to shrink slowly to some minimum radius R_0 via a hookean restoring force. We do not allow it to bend and stretching is not penalized since the core is known to be extremely soft., i.e. each core vertex slowly shrinks along its radial line. The outer polygon, which is used to model the spore coat, has more interesting mechanical behavior. In addition to the bending and stretching energy associated with the elastic ring [54], we added a substrate energy between the two concentric polygons that models

the adhesion force that exist between the coat and the core. This adhesion force is hookean and of finite range as shown in figure 3.3.

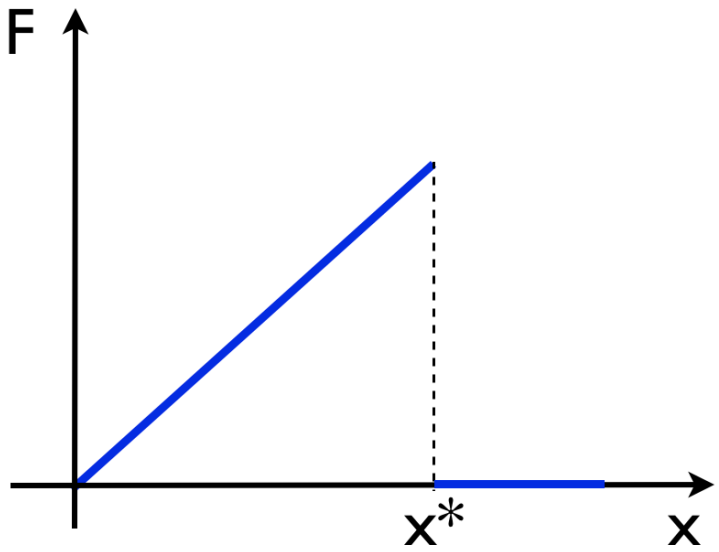

Figure 3.3: Finite range hookean restoring force between spore coat and core substrate

We will label the outer vertices by (x_i, y_i) and the inner vertices by (x_i^c, y_i^c). Let us define $\Delta x_i = x_{i+1} - x_i$, $\Delta y_i = y_{i+1} - y_i$, then the length of an outer edge is given by $\Delta r_i = \sqrt{(\Delta x_i^2 + \Delta y_i^2)}$. The angle between the i^{th} edge (tangent vector of i^{th} vertex) and the x-axis is give by θ_i, where $\tan\theta_i = \Delta y_i / \Delta x_i$. Similar notations hold for the inner polygon, with the addition of a superscript c. In all, the total energy of the spore coat is given by:

$$U(\text{coat}) = U_{bend} + U_{stretch} + U_{substrate} + U_{shear}, \tag{3.4}$$

where

$$U_{bend} = \quad -\kappa_b \sum_i \cos(\theta_{i+1} - \theta_i - \delta) \quad , \delta = \frac{2\pi}{N}, \tag{3.5}$$

$$U_{stretch} = \quad \frac{\kappa_h}{2} \sum_i \left(\frac{\Delta r_i - \ell}{\ell} \right)^2 \quad , \ell = 2R_2 \sin \frac{\pi}{N}, \tag{3.6}$$

$$U_{substrate} = \quad \frac{\kappa_s}{2} \sum_i (r_i - r_i^c)^2 \quad , r_i = \sqrt{x_i^2 + y_i^2}, \tag{3.7}$$

$$U_{shear} = \quad -\kappa_r \sum_i \cos(\theta_i^c - (i-1)\delta). \tag{3.8}$$

U_{bend} and $U_{stretch}$ denote the bending and stretching energy respectively, while $U_{substrate}$ denotes the adhesive restoring energy between the cortex and the coat. r_i^c is the equilibrium separation and U_{shear} is the shear energy when the two layers slide relative to one another.

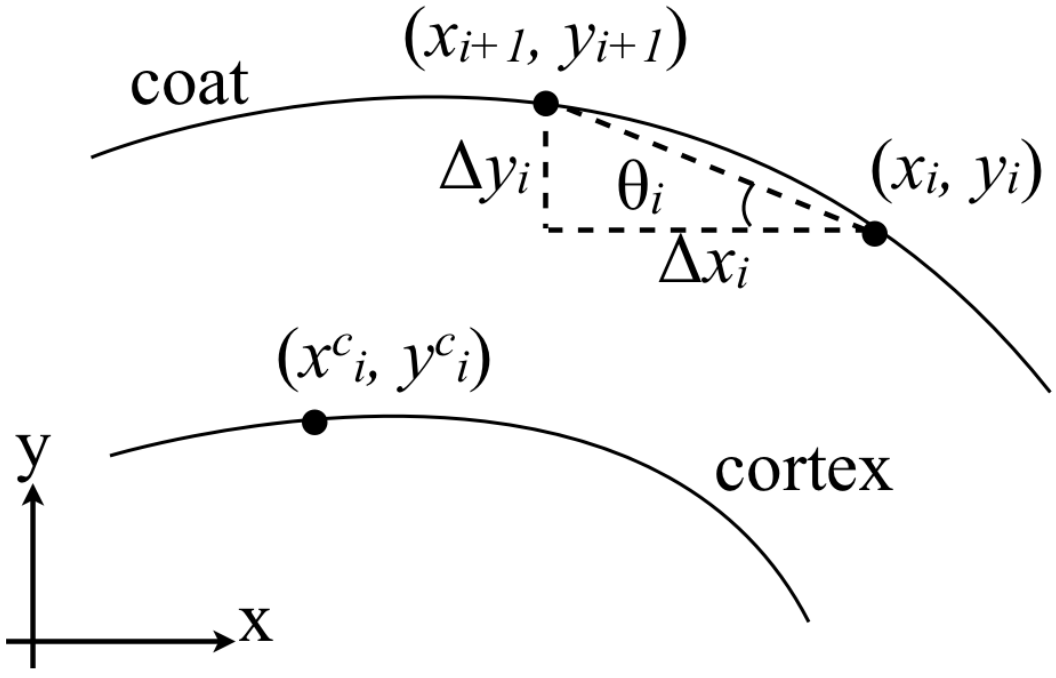

Figure 3.4: Schematic of the B. Spore: model and notations

The outer (coat) vertices (x_i, y_i) evolve via an overdamped dynamics:

$$\eta\frac{dx_i}{dt} = -\frac{\partial U(\text{coat})}{\partial x_i}, \quad \eta\frac{dy_i}{dt} = -\frac{\partial U(\text{coat})}{\partial y_i}, \tag{3.9}$$

On the other hand, since the inner polygon undergoes a simple harmonic motion

$$R_{core}(t) = R_m + A\cos\omega t,$$

where $R_m = (R_1 + R_2)/2$ and $A = (R_2 - R_1)/2$, the inner vertices $(x_i^c;\, y_i^c)$ move via

$$\frac{dx_i^c}{dt} = -\omega A\sin(\omega t)\cos(\phi_i^c), \tag{3.10}$$

$$\frac{dy_i^c}{dt} = -\omega A\sin(\omega t)\sin(\phi_i^c). \tag{3.11}$$

Where ϕ_i^c is the angle of the i^{th} inner vertice relative to the x-axis. Additionally, the Hookean adhesion force is assumed to be of finite range and the bonds linking two rings will break if the force exceeds some cutoff separation x^*, where $x^* = max()$ denotes the maximum extension of the spring at each vertex before it breaks. We can relate the elastic modulus for the substrate to the adhesion constant J. If we assume that there is one spring per edge ℓ, then

$$\frac{1}{2}\kappa_s(x^*)^2 = \frac{1}{2}\kappa_s[max(r_i - r_i^c)]^2 = J\ell. \tag{3.12}$$

3.3 Discussions

Once the simulation starts running, the inner core region will shrink to its minimum radius R_1, resulting in the outer coat being pulled inwards due to the Hookean adhesion force between the two layers and forming complex patterns of wrinkles/rucks. Typical parameter values in our model are as follows: spore radius R_{coat}, and thickness, h, of the coat to be ∼300nm and ∼40nm, respectively [104, 98] (See Table 3.1),

the measured elastic modulus of the B. subtilis coat E ∼13.6 GPa using an atomic force microscope (AFM), and the energy of adhesion between the coat and the cortex, J ∼10 Joules/m^2, associated with nonspecific electrostatic interactions between the positively charged cortex peptidoglycan [66] and the negatively charged coat [22]. Even though we do not know much about the biology happening at the spore coat, our collaborator has made measurements on the elastic properties of the coat and found that the elastic modulus of the bacteria spore remains fairly constant under various conditions such as different humidities and even after mutations, so the assumption of a constant elastic modulus is fairly reasonable.

We would like to relate the numerical values to experimentally observable quantities. Since

$$\kappa_h' \sim Eh,$$

and

$$\kappa_b' \sim Eh^3,$$

where $E = 13.9$GPa is the elastic constant and $h \sim 40$nm is the thickness of the coat, we find that $\kappa_h' \sim 500$N/m, $\kappa_b' \sim 9 \times 10^{-13}$Nm and $J \sim 1$N/m. Here the prime on the parameters represent physical values from the corresponding numerical values used in the simulation. By matching the analytical expressions for bending and stretching energy to the numerical expressions given by eqs. (3.5) and (3.6), we find

$$\kappa_h \propto \frac{\kappa_h'}{\ell},$$
$$\kappa_b \propto \frac{\kappa_b'}{\ell}.$$

The simulations show that as the rings shrink when the strain is larger than a critical threshold, so that the coat first buckles to form a symmetric wavy pattern

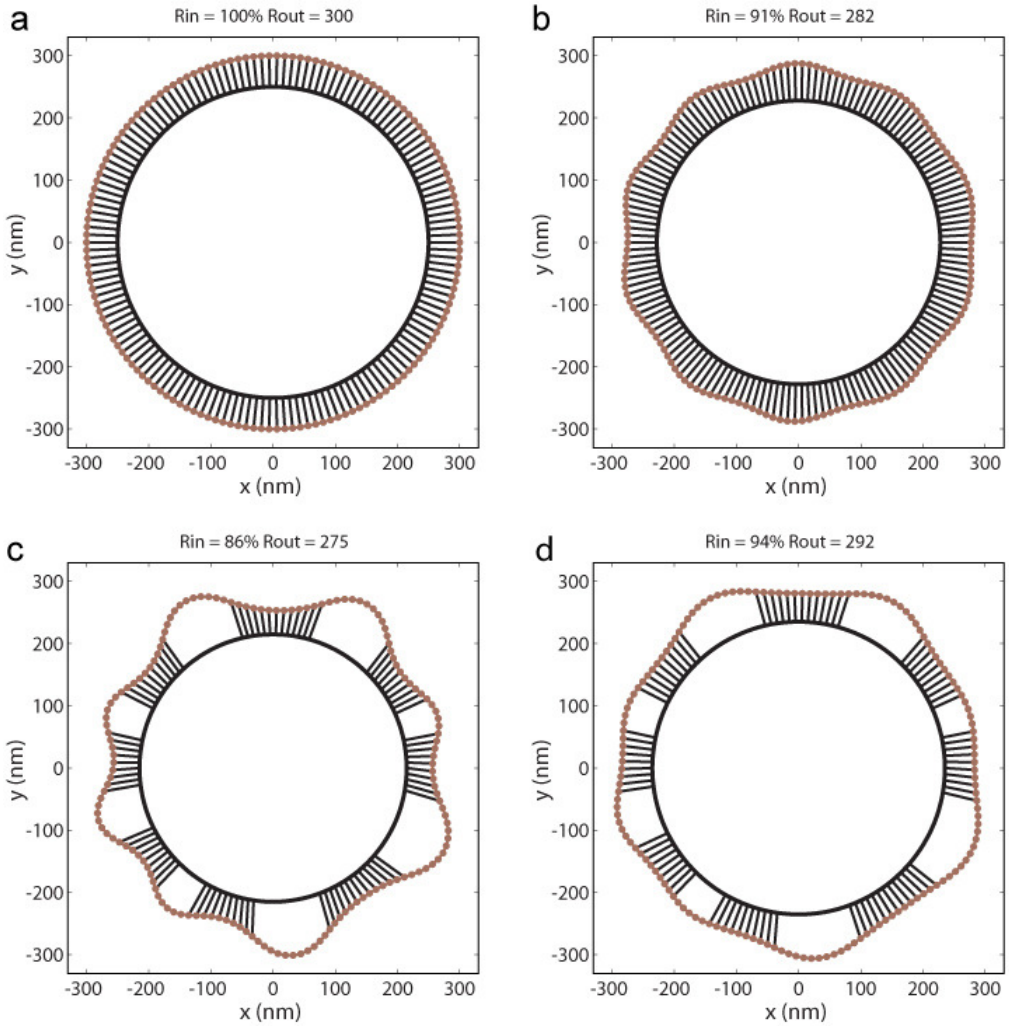

Figure 3.5: Model of formation of folds in the spore coat and their response to spore swelling. (a-c) Simulation of the ruck formation as the radius of spore interior (R_{in}) shrinks during sporulation. Rout is the average outer diameter. Using bending and stretching modulus values estimated from thickness and mechanical measurements of the coat, the model predicts the emergence of rucks that are comparable in width, height and number to previous reports [29]. (d) Upon spore expansion, rucks formed during sporulation do not reattach readily, but rather decrease their height and increase their width.

Table 3.1: Descriptions and values of the parameters used in simulations.

Name	Description	Numerical values used in simulation
N	Number of discretization	150
κ_b	Bending modulus	2×10^6
κ_h	Stretching modulus	10^5
κ_s	Adhesion modulus	360
κ_r	Shearing Modulus	10^6
T_c	Period of cortex oscillation	2
δ	Equilibrium angle	$2\pi/N$
η	Damping constant	1
R_1	Initial size of inner coat	250
R_2	Initial size of outer coat	300
A	Amplitude of cortex oscillation	18
J	Adhesion constant	52000
ℓ	Equilibrium length of outer edge	$2R_2 \sin(\pi/N)$
x^*	Maximum extension of bonds	$\sqrt{2J\ell/\kappa_s}$

around the cortex. This pattern then loses stability to delamination to form rucks (Fig. 3.5a-c). Wrinkles formed according to the mechanism in Fig. 3.5a-c are persistent. They do not readily attach back to the cortex, since they arise due to a subcritical (nonlinear) instability. This has implications for the dormant spore, since it suggests that after completion of sporulation the spore volume can increase or decrease in response to ambient relative humidity. By keeping the coat flexible, the persistence of rucks prevents the coat from resisting these changes in the volume [105, 25], thereby providing a mechanism for maintaining structural integrity of the spore. Fig. 3.5(d) shows the simulated coat geometry when the spore expands after the rucks are formed corresponding to the case when sporulation is complete.

The rucks unfold by decreasing their height and increasing their width, in qualitative agreement with our biological observations, Fig. 3.1d. Interestingly, the rucks did not unfold completely even at very high relative humidity in the AFM analy-

sis (Fig. 3.5d). We obtained similar results for B. anthracis spores (See Appendix Fig. D.1). Fully hydrated B. atrophaeus spores were previously shown to exhibit similar characteristics [79], suggesting that this behavior is not limited to a single species. This observation suggests that the expansion of the dormant spore is not limited by the coat. Instead, the cortex of the dormant spore has a limited ability to swell. Consistent with this view, B. subtilis spores lacking most of the coat due to mutations in cotE and gerE [31] were not larger than wild type spores at high relative humidity (See Appendix Fig. D.2 for experimental results done by my collaborator Ozgur Sahin). The cortexs limited ability to swell can be explained by its rigidity, as our AFM based mechanical measurements on the cotE gerE mutant revealed an elastic modulus around ∼6.9 GPa. A rigid cortex is also needed to sustain pulling forces on the coat, as well as in creating a tight girdle around the dehydrated core. Thus, it seems that our simple double concentric elastic extensible ring model is able to explain the formation of rucks on the bacteria spore coat satisfactorily.

3.4 Mathematical Model

Our analysis of the buckling states of an extensible elastic ring is based on the Euler-Bernoulli theory of elastic beam [60, 54, 2, 3]. The Euler-Bernoulli's hypothesis states that plane cross sections which are perpendicular to the neutral axis before deformation remain plane and perpendicular to the neutral axis after deformation, i.e. no shear strain. Consider a rod of length ℓ initially along the horizontal axis connected to a system of elastic hookean springs . A compressive force P is applied to the ends so that the rod bends. The point that is initially at $(x, 0)$ will be deformed

to $(x+u(x), w(x))$ as shown in figure C.1. A small element along the rod dx becomes $ds = (1+\epsilon)dx$ after deformation and experience a restoring force in the vertical direction proportional to w. Let θ be the angle that the tangent to the midline makes with the horizontal axis and denote $A_x \equiv dA/dx$. From geometric consideration, we find that

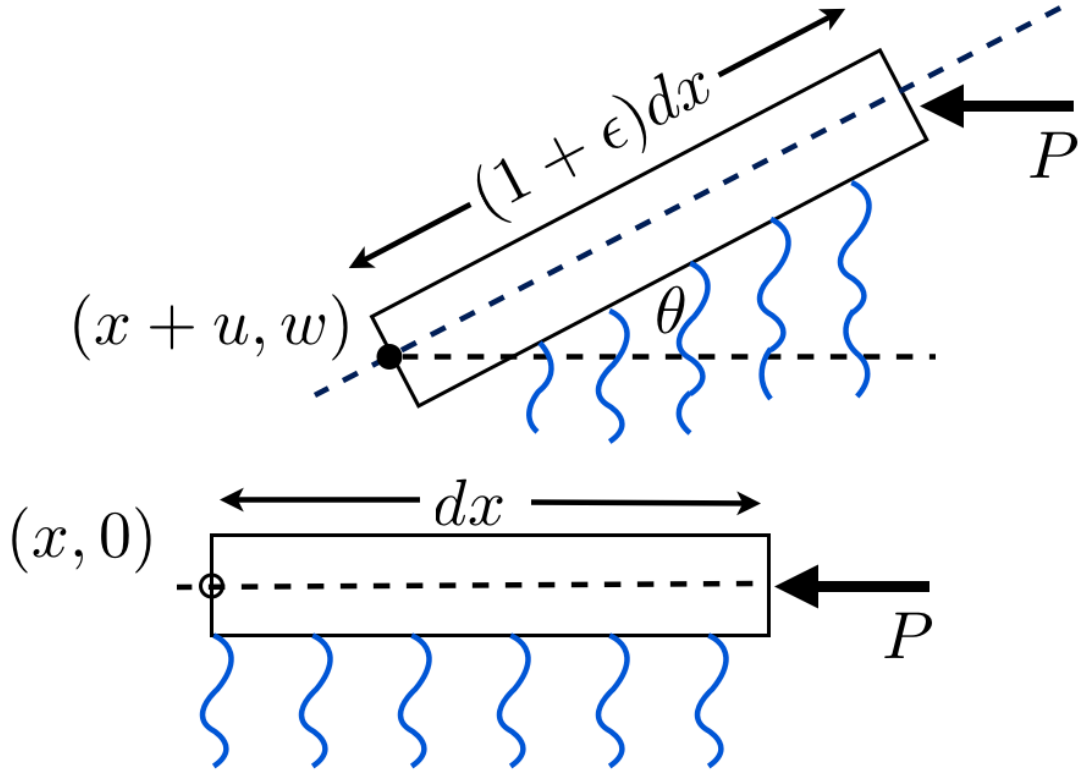

Figure 3.6: Deformation of a beam cross-section. The point $(x, 0)$ moved to $(x + u(x), w(x))$ after deformation where $w(x)$ is the vertical displacement and $u(x)$ is the horizontal displacement. The length of the segment dx is stretched to $ds = (1+\epsilon)dx$, where $\epsilon = \sqrt{(1+u_x)^2 + w_x^2} - 1$. Blue curly lines denote the elastic hookean springs.

$$\cos\theta(x) = \frac{1+u_x}{1+\epsilon}, \quad \sin\theta(x) = \frac{w_x}{1+\epsilon}, \tag{3.13}$$

where

$$1 + \epsilon = \sqrt{(1 + u_x)^2 + w_x^2}. \tag{3.14}$$

The curvature is

$$\kappa = \frac{d\theta}{ds} = \frac{\theta_x}{1 + \epsilon}. \tag{3.15}$$

The potential energy of the system is given by

$$U = \int_0^\ell dx \left(\frac{1}{2} EI\theta_x^2 + \frac{1}{2} EA\epsilon^2 + \frac{1}{2} Kw^2 \right) + P\Delta u, \tag{3.16}$$

where $\frac{1}{2}Kw^2$ represents the elastic spring support energy per unit length and $P\Delta u$ represents the work done by the applied force P. Since

$$\Delta u = u(L) - u(0) = \int_0^\ell dx((1 + \epsilon)\cos\theta - 1), \tag{3.17}$$

we find that we can rewrite (3.16) as

$$U = \int_0^\ell dx \left(\frac{1}{2} EI\theta_x^2 + \frac{1}{2} EA\epsilon^2 + \frac{1}{2} Kw^2 + P((1 + \epsilon)\cos\theta - 1) \right). \tag{3.18}$$

Let us define a new variable η such that $\eta_x = w$. Requiring that the first variation of the potential energy to vanish, we find that

$$\begin{aligned} \delta U = & \int_0^\ell dx \left\{ -EI\theta_{xx} - (1 + \epsilon)P\sin\theta - K\eta(1 + \epsilon)\cos\theta \right\} \delta\theta \\ & + \int_0^\ell dx \left\{ P\cos\theta - K\eta\sin\theta + EA\epsilon \right\} \delta\epsilon \\ & + [EI\theta_x \delta\theta]_0^\ell + [K\eta\delta w]_0^\ell = 0, \end{aligned} \tag{3.19}$$

where we use

$$\delta w_x = \sin\theta\delta\epsilon + (1 + \epsilon)\cos\theta\delta\theta \tag{3.20}$$

to get rid of δw_x. Since the variations $\delta\epsilon$, $\delta\theta$ are arbitrary, the terms in the parenthesis must necessarily vanish separately. The last two boundary terms vanish due to the boundary conditions (for a pinned-pinned beam):

$$\theta_x(0) = \theta_x(\ell) = w(0) = w(\ell) = 0. \tag{3.21}$$

We find that

$$\epsilon = -\frac{P}{EA}\cos\theta + \frac{\eta K}{EA}\sin\theta. \tag{3.22}$$

After going through some algebra, we find that a compressible elastic beam with spring support can be described by two ordinary differential equations

$$\begin{aligned}\theta_{xx} = &-\alpha P(1 - \beta P\cos\theta + \beta K\eta\sin\theta)\sin\theta \\ &- \alpha K\eta(1 - \beta P\cos\theta + \beta K\eta\sin\theta)\cos\theta,\end{aligned} \tag{3.23}$$

$$\eta_{xx} = (1 - \beta P\cos\theta + \beta K\eta\sin\theta)\sin\theta, \tag{3.24}$$

subject to the boundary conditions given by (3.21) where we have defined $\alpha = (EI)^{-1}$ and $\beta = (EA)^{-1}$. Notice that this problem has reflectional symmetry or $\mathbf{Z}_2$-symmetry: $(\theta, \eta) \to (-\theta, -\eta)$. The trivial solution is simply $(\theta, \eta) = (0, 0)$, i.e. the fundamental solution. We are interested in the bifurcation from the fundamental solution. Let us expand the 2 ODE in a Taylor series as follows:

$$\begin{aligned}\theta_{xx} = &-\alpha K(1 - \beta P)\eta - \alpha P(1 - \beta P)\theta \\ &- \alpha\beta K^2\eta^2\theta + \frac{1}{2}\alpha K(1 - 4\beta P)\eta\theta^2 + \frac{1}{6}\alpha P(1 - 4\beta P)\theta^3 + ...\end{aligned} \tag{3.25}$$

$$\eta_{xx} = (1 - \beta P)\theta + \beta K\eta\theta^2 - \frac{1}{6}(1 - 4\beta P)\theta^3 + ... \tag{3.26}$$

Note that when we set $K = 0$ into (3.25), we recover the well-known Duffing's equation.

3.5 Bifurcation Analysis

Let us rewrite the system of ODE (3.25) and (3.26) in an abstract form more suitable for analysis [40]. Let

$$\Phi(\theta, \eta) = L \begin{pmatrix} \theta \\ \\ \eta \end{pmatrix} + N(\theta, \eta) = 0, \tag{3.27}$$

where the linear part is given by

$$L \begin{pmatrix} \theta \\ \\ \eta \end{pmatrix} = \frac{\partial^2}{\partial x^2} \begin{pmatrix} \theta \\ \\ \eta \end{pmatrix} + \begin{pmatrix} \alpha P(1-\beta P) & \alpha K(1-\beta P) \\ \\ -(1-\beta P) & 0 \end{pmatrix} \begin{pmatrix} \theta \\ \\ \eta \end{pmatrix}, \tag{3.28}$$

and the nonlinear part is given by

$$N(\theta, \eta) = \begin{pmatrix} \alpha\beta K^2\eta^2\theta - \frac{1}{2}\alpha K(1-4\beta P)\eta\theta^2 - \frac{1}{6}\alpha P(1-4\beta P)\theta^3 \\ \\ -\beta K\eta\theta^2 + \frac{1}{6}(1-4\beta P)\theta^3 \end{pmatrix}. \tag{3.29}$$

The In this form, $\Phi(\theta, \eta; P, K, \alpha, \beta) : \mathscr{X} \times \mathbb{R}^4 \to \mathscr{Y}$ is a mapping between Banach spaces defined as follows. The domain $\mathscr{X}$ is the space of all real-valued, twice continuously differentiable vector function $\vec{q}(x) = (\theta(x), \eta(x))^T$ defined on $x \in [0, \ell]$ that has vanishing first derivatives at the boundaries, i.e. $\vec{q}(0) = \vec{q}(\ell) = \vec{0}$. $\mathbb{R}^4$ refers to the space spanned by the four real variables $\{P, K, \alpha, \beta\}$. The range $\mathscr{Y}$ is the space of continuous vector function defined on $x \in [0, \ell]$. Observe that $\Phi(0, 0; P, K, \alpha, \beta) = 0$ for all P, K. In other words, the undeformed configuration satisfies the equilibrium equations for any external load P and spring constant K. In our analysis, we will treat P as the bifurcation parameter and keep K, α, β fixed.

3.5.1 Linearized Problem

We claim that all eigenfunctions of linear part L have the form

$$\begin{pmatrix} \theta \\ \\ \eta \end{pmatrix} = \cos\left(\frac{n\pi x}{\ell}\right) \begin{pmatrix} c_1 \\ \\ c_2 \end{pmatrix}, \tag{3.30}$$

where n is a positive integer. Observe that the two parameters c_1 and c_2 span a two-dimensional subspace of functions which is invariant for L and they satisfy the boundary conditions (3.21). For each n, there exist two linearly independent eigenfunctions of L. By Fourier analysis,

$$\{\cos(n\pi x/\ell) : n = 1, 2, 3, ...\} \tag{3.31}$$

is a complete set of scalar functions. Arguing componentwise, it follows that (3.30) provides a complete set of vector functions. Thus, we can restrict L to this two-dimensional subspace, namely L_2, which is

$$\begin{pmatrix} -\gamma^2 + \alpha P(1-\beta P) & \alpha K(1-\beta P) \\ \\ -(1-\beta P) & -\gamma^2 \end{pmatrix}, \tag{3.32}$$

where $\gamma = n\pi/\ell$. The determinant is given by

$$\det(L_2) = \gamma^2(\gamma^2 - \alpha P(1-\beta P)) + \alpha K(1-\beta P)^2. \tag{3.33}$$

The linear map L_2 is invertible unless the determinant vanishes in which case, the implicit function theorem fails and we have a bifurcation. Solving for P, we find that

$$P_{\pm}^{(n)} = \frac{2\alpha\beta K + \alpha\gamma^2 \pm \gamma^2\sqrt{\alpha(\alpha - 4\beta^2 K - 4\beta\gamma^2)}}{2\alpha\beta^2 K + 2\alpha\beta\gamma^2}. \tag{3.34}$$

Let us define the effective spring constant $\mu = \beta K$, the slenderness $\lambda = \sqrt{A\ell^2/I} = \sqrt{\alpha\ell^2/\beta}$ and the Euler load $P_E = \pi^2 EI/\ell^2 = \pi^2/(\alpha\ell^2)$. Then we can rewrite (3.34)

more compactly as

$$\frac{P_{\pm}^{(n)}}{P_E} = \frac{\lambda^2}{2\pi^2}\left[\frac{(2\mu+\gamma^2)}{(\mu+\gamma^2)} \pm \frac{\gamma^2}{(\mu+\gamma^2)}\sqrt{1-\frac{4\ell^2(\mu+\gamma^2)}{\lambda^2}}\right]. \tag{3.35}$$

Notice that $P_{\pm}^{(n)}/P_E$ is real-valued only when

$$\lambda^2 \geq \lambda_0^2(n) = 4\ell^2(\mu + (n\pi/\ell)^2). \tag{3.36}$$

When $\lambda^2 < \lambda_0^2(1)$, $P_{\pm}^{(1)}/P_E$ is not real, implying that bifurcation is not possible and the fundamental mode $(\theta, \eta) = (0, 0)$ is the only solution. This can be interpreted as the shortening of the beam is sufficient to accommodate the increased in external load that buckling never occurs. When $\lambda^2 = \lambda_0^2(n)$, we have a double root since $P_+^{(n)} = P_-^{(n)}$ and there is only one bifurcation. This point will be further elucidated in a latter section.

As $\lambda \to \infty$, we find that

$$\frac{P_-}{P_E} \approx \frac{\lambda^2}{\pi^2}\left(\frac{\mu}{\mu+(n\pi/\ell)^2} + \frac{2n^2\pi^2}{\lambda^2}\right) + O(\lambda^{-2}) \tag{3.37}$$

and

$$\frac{P_+}{P_E} \approx \frac{\lambda^2}{\pi^2}\left(1 - \frac{n^2\pi^2}{\lambda^2}\right) + O(\lambda^{-2}). \tag{3.38}$$

For the case $\mu = 0$, we find that (3.35) reduces to

$$\frac{P_{\pm}}{P_E} = \frac{\lambda^2}{2\pi^2}\left(1 \pm \sqrt{1-\frac{4\pi^2 n^2}{\lambda^2}}\right), \tag{3.39}$$

which agrees with earlier work by Magnusson *et al* [60].

3.5.2 Stability of Fundamental Solution

Let us now consider the stability of the fundamental solution, $(\theta, \eta) = (0, 0)$. The matrix L_2 has two eigenvalues, which are the roots of the characteristic equation

$$\lambda^2 - \text{trace}(L_2)\lambda + \det(L_2) = 0. \tag{3.40}$$

The system is stable if the two eigenvalues have negative real parts, otherwise it is unstable [53, 23]. We will study the stability by looking at the trace and determinant of L_2. The trace of L_2 is

$$\text{trace}(L_2) = \alpha P(1 - \beta P) - 2\gamma^2, \tag{3.41}$$

and the determinant is given by (3.33). There are four possible combinations for the signs of $\det(L_2)$ and $\text{trace}(L_2)$. Whenever $\det(L_2) < 0$, one of the eigenvalues must be real and positive so the system is unstable regardless of the sign of $\text{trace}(L_2)$. If $\det(L_2) > 0$ and $\text{trace}(L_2) > 0$, the system is unstable since the eigenvalues are either both real and positive or are a pair of complex conjugates with positive real part. Hence we find that the system is stable only if $\det(L_2) > 0$ and $\text{trace}(L_2) < 0$. In this case, the two eigenvalues of L_2 are either a pair of complex conjugates with negative real parts or real and negative. Since the eigenvalues have negative real parts, the system is stable. The graph of $\text{trace}(L_2)$ and $\det(L_2)$ for typical values of α, β and K is plotted in figure 3.7.

The trace changes sign when

$$\alpha P(1 - \beta P) = 2\gamma^2. \tag{3.42}$$

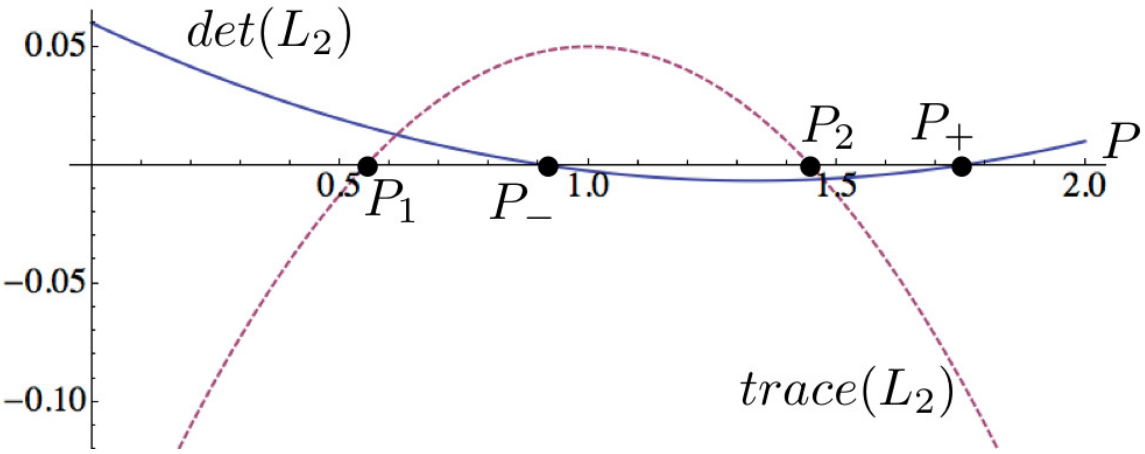

Figure 3.7: Stability diagram. Plot of $\det(L_2)$ (solid blue line) given by Eqn. (3.33) and $\mathrm{trace}(L_2)$ (dashed red line) given by Eqn. (3.43) as a function of P for typical values of α, β, K and $n = 1$. Refer to Eqns. (3.34) and (3.35). The determinant vanishes at $P = P_\pm$ as defined by (3.35). The trace vanishes at $P = P_{1,2}$ as defined by (3.43). In this case, the fundamental solution is stable for $P < P_1$ and $P > P_+$.

Solving for P, we find that

$$\frac{P_{1,2}^{(n)}}{P_E} = \frac{\lambda^2}{2\pi^2}\left(1 \pm \sqrt{1 - \frac{8n^2\pi^2}{\lambda^2}}\right), \tag{3.43}$$

where $P_1^{(n)}$ is the smaller of the two roots. At $P_{1,2}^{(n)}$, if $\det(L_2) > 0$, we find that the pair of complex conjugate eigenvalues of the linearization crosses the imaginary axis of the complex plane. This is the well-known Poincaré-Andronov-Hopf bifurcation. If $\det(L_2) < 0$ at $P_1^{(n)}$, the eigenvalues are real, equal in magnitude and opposite in signs. This point is a saddle node. Since one of the eigenvalues is positive, the system is unstable. By inspection, we see that

$$\min_n P_1^{(n)} = P_1^{(1)}, \quad \text{and} \quad \max_n P_2^{(n)} = P_2^{(1)}. \tag{3.44}$$

Following the discussion in Magnusson *et al* [60], we similarly require that $\epsilon > -1$ and that $\epsilon \leq -1$ is nonpermissible. This material model corresponds to a "spring-like" material that is linear until the two ends of the spring touch where it becomes

infinitely stiff. This implies that for the fundamental path, i.e. $(\theta, \eta) = (0, 0)$, the admissible region, defined by $\epsilon > -1$, we obtain

$$\frac{P}{P_E} < \frac{\lambda^2}{\pi^2}. \tag{3.45}$$

Let us define

$$P_a = \min_n \left\{ P_-^{(n)}, P_1^{(1)} \right\} \quad \text{and} \quad P_b = \max_n \left\{ P_+^{(n)}, P_2^{(1)} \right\}. \tag{3.46}$$

Thus, we conclude that the fundamental solution, $(\theta, \eta) = (0, 0)$, is stable when $0 < P < P_a$ and $P_b < P < \lambda^2 P_E/\pi^2$. This is a region bordered by the following curves: $P = \lambda^2/\pi^2$, $P = P_a$ and $P = P_b$.

3.5.3 Phase Diagram

We see that three types of bifurcation can arise in this system. When $\det(L_2) = 0$, we get the *steady-state bifurcation* (codimension one) whereby one of the two eigenvalues becomes zero. When $\text{trace}(L_2) = 0$ and $\det(L_2) > 0$, we get *Hopf bifurcation* (codimension one), whereby the two eigenvalues crosses the imaginary axis. Lastly, when $\text{trace}(L_2) = 0$ and $\det(L_2) = 0$, we get the the *Bogdanov-Takens (BT) bifurcation* (codimension two) at which the critical equilibrium has a zero eigenvalue of (algebraic) multiplicity two [53]. At each BT bifurcation point, the Hopf bifurcation curve turns into the neutral saddle curve (with real $\lambda_1 = -\lambda_2$). The case for $n = 1$ is plotted in figure 3.8 and the graphs for $n = 2, 3, \ldots$ look qualitatively similar. We can piece all these information to get the complete phase diagram as shown in figure 3.9. For $n = 1$ and $\lambda = 10$, there exist two buckling loads with the same eigenmode. For $\lambda = 20$, we get a total of five buckling loads belonging to two eigenmodes($n = 1, 2$),

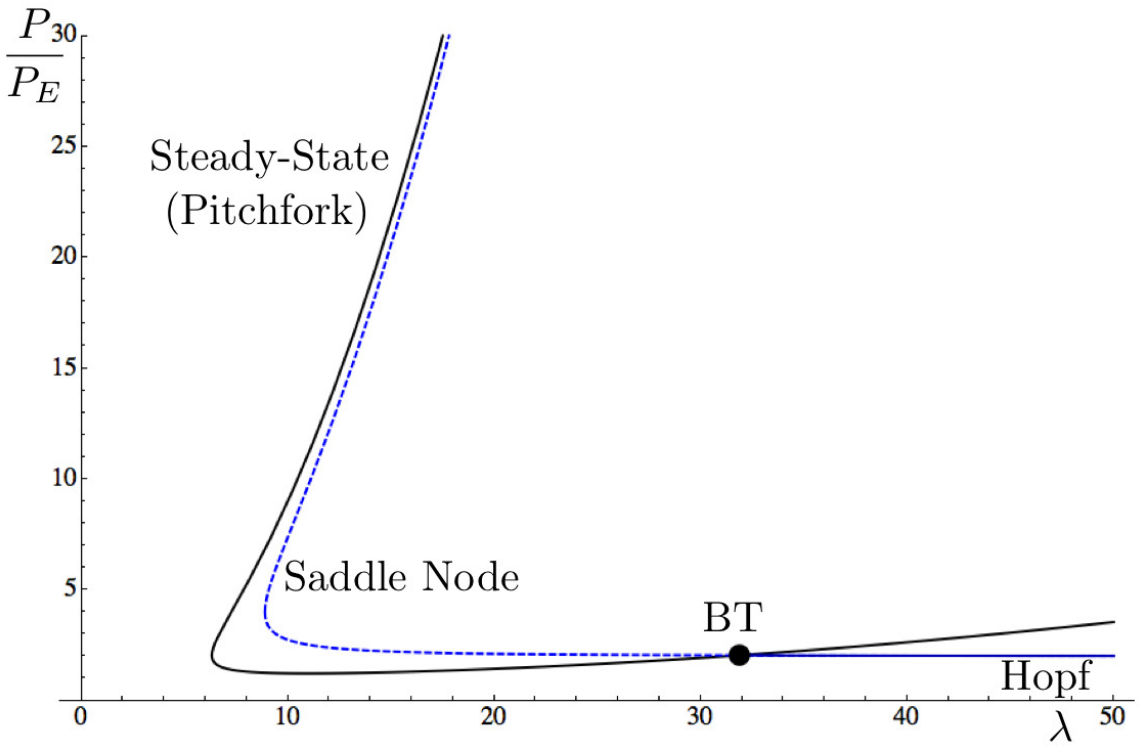

Figure 3.8: Phase diagram of the applied load versus slenderness for $\mu = 0.1$, $\ell = 1$ and $n = 1$. Solid black line denotes steady-state bifurcation whereby $\det(L_2) = 0$. The blue solid line denotes Hopf bifurcation while the blue dash line denotes neutral saddle curve, both of which satisfy $\text{trace}(L_2) = 0$. The Bogdanov-Takens (BT) point occurs when the curves $\det(L_2) = 0$ and $\text{trace}(L_2) = 0$ intercepts.

four of which are steady-state bifurcation and one is the Hopf bifurcation. When λ is increased past 50, a second Hopf bifurcation appears.

Along the steady-state bifurcation, we need to calculate the normal form in order to determine the type of codim 1 bifurcation that arises. As we will see in the next section, we will get supercritical or subcritical pitchfork bifurcation depending on the parameters. On the other hand, along the Hopf bifurcation branches as shown by the blue dashed curves in figure 3.9, depending on the value of the first Lyapunov coefficient ℓ_1, we may have supercritical ($\ell_1 < 0$), subcritical ($\ell_1 > 0$) or Bautin (also

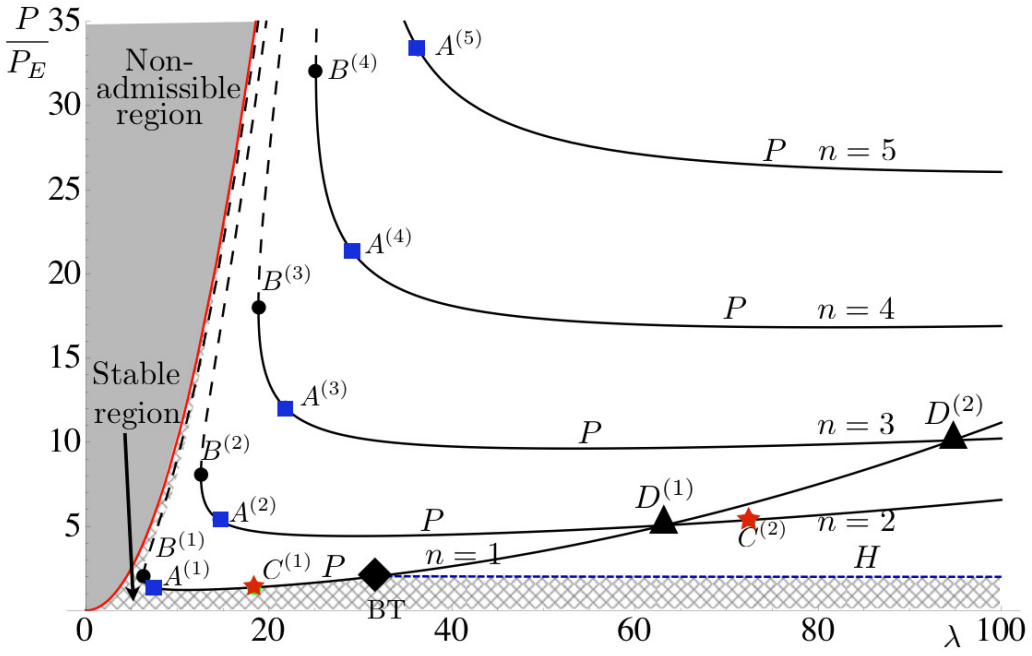

Figure 3.9: Phase diagram of the applied load versus slenderness for $\mu = 0.1$ and $\ell = 1$. Black dashed lines denote $P^+(n)$ and the solid black line denote $P^-(n)$, which are the two roots of $\det(L_2) = 0$ given by Eqn. (3.33) for the different values of n. $n = 1, ..., 5$ is shown. P= Pitchfork, H=Hopf. The black points $B^{(n)}$ denotes $P^+(n) = P^-(n)$; the points $A^{(n)}$ (blue square) and $C^{(n)}$ (red star) mark where the pitchfork bifurcation changes stability. The bifurcation for each n is supercritical between $A^{(n)}$ and $C^{(n)}$ and subcritical otherwise. The points $D^{(n)}$ marked where different n's crosses, i.e. $D^{(1)}$ marks $n = 1$ crosses $n = 2$. The non-admissible shaded grey is bordered by the vertical axis and the red curve $P/P_E = \lambda^2/\pi^2$. The blue dashed line denotes the Hopf bifurcation. The Bogdanov-Takens (BT) point (black diamond) occurs when the curves $\det(L_2) = 0$ and $\text{trace}(L_2) = 0$ intercepts. The hatched region denotes where the fundamental solution is stable.

known as generalized Hopf) bifurcations ($\ell_1 = 0$). Bautin bifurcation arises naturally when a supercritical Hopf transit into a subcritical Hopf [53]. We will show later that the Hopf bifurcation is a subcritical one for all values of λ.

3.6 Recognition problem

3.6.1 Steady-State bifurcation

In this section, we will determine the type of steady state bifurcation along the $\det(L_2) = 0$ branches in the phase space. We will carry out our analysis of (3.27) using Liapunov-Schmidt reduction methods [40]. First, let us decompose $\mathscr{X}$ and $\mathscr{Y}$ as follows

$$\mathscr{X} = kernel(L_2) \oplus (kernel(L_2))^{\perp}, \tag{3.47}$$

$$\mathscr{Y} = range(L_2) \oplus (range(L_2))^{\perp}. \tag{3.48}$$

The one-dimensional kernel of L_2 is spanned by $m_1(x)$, where

$$m_1(x) = \cos(n\pi x/\ell) \begin{pmatrix} \gamma^2 \\ -(1-\beta P_{\pm}) \end{pmatrix} = c(x) \begin{pmatrix} a_1 \\ a_2 \end{pmatrix}, \tag{3.49}$$

where $P_{\pm}$ is a solution to (3.34) and $c(x) = \cos(n\pi x/\ell)$. By Fredholm alternative, we have

$$(range(L_2))^{\perp} = kernel(L_2^*). \tag{3.50}$$

The one-dimensional kernel of L_2^*

$$\begin{pmatrix} -\gamma^2 + \alpha P(1-\beta P) & -(1-\beta P) \\ \alpha K(1-\beta P) & -\gamma^2 \end{pmatrix}, \tag{3.51}$$

is spanned by $n_1(x)$, where

$$n_1(x) = \cos(n\pi x/\ell) \begin{pmatrix} \gamma^2 \\ \alpha K(1-\beta P_\pm) \end{pmatrix} = c(x) \begin{pmatrix} b_1 \\ b_2 \end{pmatrix}. \tag{3.52}$$

We find that L_2 is Fredholm with index 0 since $dim(kernel(L_2)) = codim(range(L_2)) = 1$. Using $m_1(x)$ as a basis for $kernel(L_2)$ and $n_1(x)$ as a basis for $(range(L_2))^\perp$, we can formally calculate the reduced scalar equation $g(u, P)$ where u parametrizes $kernel(L_2)$, i.e. $u\, m_1(x)$. Since our problem has the trivial solution $\theta = \eta = 0$, from which it follows that $g(0, P) \equiv 0$. Thus at the singularity at the origin, we have

$$g = g_u = g_P = g_{PP} = 0. \tag{3.53}$$

In order to find the normal form of the scalar function $g(u, P)$, we need to calculate the different derivatives of g *w.r.t.* u and P. In particular, we find that

$$(d\Phi)_{0,P} = L_2. \tag{3.54}$$

Due to the $\mathbf{Z}_2$ symmetry, at the trivial point [40],

$$(d^2\Phi)_{0,P} = 0 \quad \text{and} \quad \Phi_P = \frac{\partial \Phi}{\partial P} = 0, \tag{3.55}$$

which implies that

$$g_{uu} = 0. \tag{3.56}$$

We would like to calculate g_{uuu} and g_{uP} and they are given by [40]:

$$g_{uuu} = \langle n_1, d^3\Phi(m_1, m_1, m_1)\rangle, \tag{3.57}$$

$$g_{uP} = \langle n_1, d\Phi_P \cdot m_1\rangle. \tag{3.58}$$

The k-th order differential of a mapping Φ at a point $u \in \mathscr{X}$ is given by the following formula,

$$(d^k\Phi)_u(v_1, ..., v_k) = \frac{\partial}{\partial t_1} \cdots \frac{\partial}{\partial t_k} \Phi \left(u + \sum_{i=1}^{k} t_i v_i \right) \Bigg|_{t=0}. \tag{3.59}$$

Using this formula, we find that

$$d\Phi_P \cdot m_1 = d\left(\frac{\partial \Phi}{\partial P}\right) \cdot m_1 = c(x) \begin{pmatrix} \alpha(1 - 2\beta P_\pm)a_1 - \alpha\beta K a_2 \\ \\ \beta a_1 \end{pmatrix}, \tag{3.60}$$

and

$$d^3\Phi(m_1, m_1, m_1) = c^3(x) \begin{pmatrix} 6\alpha\beta K^2 a_1 a_2^2 - 3K(1 - 4\beta P_\pm)a_1^2 a_2 - \alpha P_\pm (1 - 4\beta P_\pm)a_1^3 \\ \\ -6\beta K a_1^2 a_2 + (1 - 4\beta P_\pm)a_1^3 \end{pmatrix}. \tag{3.61}$$

Plugging these expressions into (3.57) and (3.58), we find that

$$\begin{aligned} g_{uP}^{\pm} &= A\left((\alpha(1 - 2\beta P_\pm)a_1 - \alpha\beta K a_2)b_1 + \beta a_1 b_2\right) \\ &= \mp A\gamma^4 \sqrt{\alpha(\alpha - 4\beta(\mu + \gamma^2))} \\ &= \mp A\frac{\beta}{\ell^2}\gamma^4 \sqrt{\lambda^2(\lambda^2 - 4\ell^2(\mu + \gamma^2))}, \end{aligned} \tag{3.62}$$

where $A = \int_0^\ell \cos^2(n\pi/\ell)dx = \ell/2$. If $\lambda^2 \geq \lambda_0^2(n)$, g_{uP} is real. In particular, $g_{uP} = g_{uP}^+ < 0$ when $P = P_+$ and $g_{uP} = g_{uP}^- > 0$ when $P = P_-$. Similarly, we find that

$$\begin{aligned} g_{uuu}^{\pm} &= B \begin{pmatrix} 6\alpha\beta K^2 a_1 a_2^2 - 3K(1 - 4\beta P_\pm)a_1^2 a_2 - \alpha P_\pm (1 - 4\beta P_\pm)a_1^3 \\ \\ -6\beta K a_1^2 a_2 + (1 - 4\beta P_\pm)a_1^3 \end{pmatrix} \cdot \begin{pmatrix} b_1 \\ \\ b_2 \end{pmatrix} \\ &= B\gamma^8 \frac{3\alpha(2\mu + \gamma^2) - 8\beta(\mu + \gamma^2)(3\mu + \gamma^2) \pm 3\gamma^2\sqrt{\alpha(\alpha - 4\beta(\mu + \gamma^2))}}{2\beta(\mu + \gamma^2)} \\ &= B\gamma^8 \frac{3\lambda^2(2\mu + \gamma^2) - 8\ell^2(\mu + \gamma^2)(3\mu + \gamma^2) \pm 3\gamma^2\sqrt{\lambda^2(\lambda^2 - 4\ell^2(\mu + \gamma^2))}}{2\ell^2(\mu + \gamma^2)} \end{aligned} \tag{3.63}$$

where $B = \int_0^\ell \cos^4(n\pi/\ell)dx = 3\ell/8$. If $\lambda^2 \geq \lambda_0^2(n)$, g_{uuu} is always real. The plot of $g_{uP}^{\pm}$ and $g_{uuu}^{\pm}$ is shown in figure 3.10.

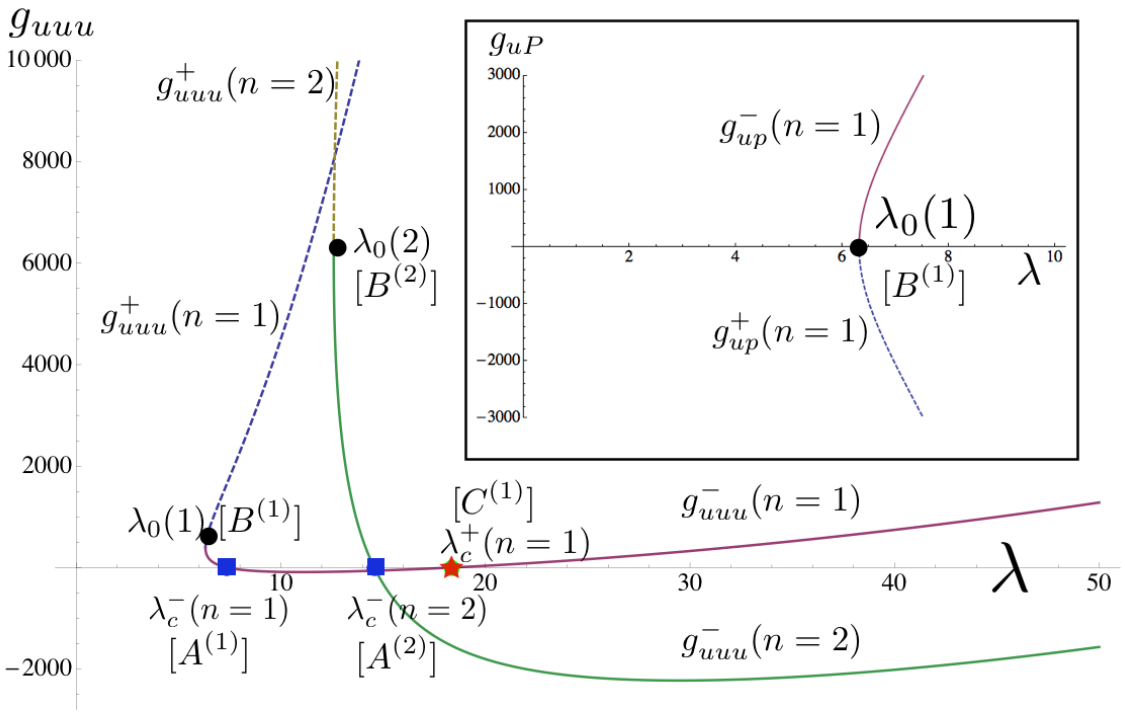

Figure 3.10: Term in the normal form, $g_{uuu}^{\pm}$, given by Eqn. (3.63) as a function of slenderness λ. g_{uuu}^{+} is always positive while the sign of g_{uuu}^{-} depends on λ. g_{uuu}^{-} vanishes when $\lambda = \lambda_c^{\pm}$ The dashed lines denote P^+; the solid lines denote P^-. At $\lambda_0(n)$, $P^+(n) = P^-(n)$. These are the points $B^{(n)}$ as shown with black dots. $\lambda_c^-(n)$ are the points $A^{(n)}$ (shown as blue squares) while $\lambda_c^+(n)$ mark the points $C^{(n)}$. (shown as red star) Inset: $g_{uP}^{\pm}(n=1)$ as a function of λ. $g_{uP}^{+}(n=1) = g_{uP}^{-}(n=1)$ at $\lambda_0(n=1)$. From these two plots, we find that P^+ is always subcritical while P^- is subcritical when $\lambda_0(n) < \lambda < \lambda_c^-(n)$, supercritical when $\lambda_c^-(n) < \lambda < \lambda_c^+(n)$ and subcritical when $\lambda_c^+(n) < \lambda$.

Along the bifurcating branch P_+, we find that $g_{uuu}^{+} > 0$ and $g_{uP}^{+} < 0$ for all values of $\lambda > 0$. Together with (3.53) and (3.56), this means that the normal form along P_+ is

$$g(u, P) \sim u^3 - P_+ u, \tag{3.64}$$

which is a supercritical pitchfork. The bifurcation branch along P^- is more interesting. g^-_{uuu} vanishes when

$$(\lambda_c^{\pm})^2 = \ell^2 \frac{\gamma^4 + 20\mu\gamma^2 + 24\mu^2 \pm \gamma^3\sqrt{\gamma^2 - 24\mu}}{6\mu}. \tag{3.65}$$

We can substitute this value into (3.35) to find P_c. These critical points where the cubic term g^-_{uuu} vanishes are shown as the points $A^{(n)}$ and $C^{(n)}$, $n = 1, 2, ..$ in figure 3.9, where $A^{(n)}$'s denote the smaller root. For small values of P^-, g^-_{uuu} is positive. However, as we increase P^-, g^-_{uuu} decreases until it vanishes at λ_c^-, and g^-_{uuu} becomes negative until the point λ_c^+, beyond which g^-_{uuu} becomes positive again. Therefore, we see that when $\lambda_0(n) < \lambda < \lambda_c^-$, i.e. small slenderness, $g^-_{uuu} > 0$ and $g^-_{uP} > 0$ and so this is a subcritical bifurcation. The normal form is given by

$$g(u, P_-) \sim u^3 + P_- u. \tag{3.66}$$

When $\lambda_c^- < \lambda < \lambda_c^+$, i.e. intermediate slenderness, $g^-_{uuu} < 0$ and $g^-_{uP} > 0$ and so this is a supercritical bifurcation. The normal form changes to

$$g(u, P_-) \sim -u^3 + P_- u. \tag{3.67}$$

Finally, when $\lambda_c^+ < \lambda$, i.e. large slenderness, $g^-_{uuu} > 0$ and $g^-_{uP} > 0$ and we get back a subcritical bifurcation, and the normal form is given by (3.66).

At $\lambda = \lambda_0(n)$ (points $B^{(n)}$'s in figure 3.9) where P_+ and P_- meet, we have a double root ($P_+ = P_-$) and the normal form of the bifurcation is

$$g(u, P_-) \sim u^3 - (P - P_{\pm})^2 u. \tag{3.68}$$

In this special case, g exhibits a nondegenerate cubic symmetry of $\mathbf{Z}_2$-codimension one ($\mathbf{Z}_2$ symmetry). When $\lambda = \lambda_c^-$ or $\lambda = \lambda_c^+$, $g^{\pm}_{uuu}$ vanishes and the normal form

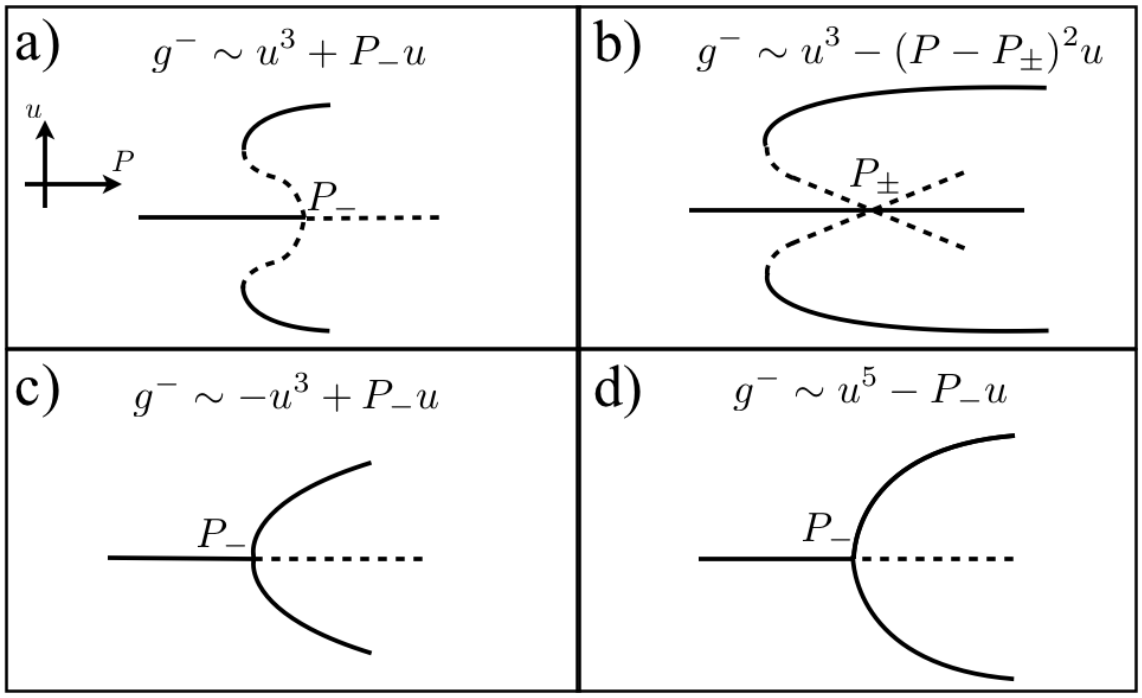

Figure 3.11: Bifurcation diagrams associated with the buckling of the compressible beam on elastic spring support as a function of the applied force P. Vertical axis is u and the horizontal axis is P. $g^+_{uuu} > 0$ and $g^+_{uP} < 0$ holds true for different values of λ. a) When $\lambda_0(n) < \lambda < \lambda^-_c$ or $\lambda^+_c < \lambda$, $g^-_{uuu} > 0$, $g^-_{uP} > 0$ and we get a subcritical pitchfork. b) When $\lambda = \lambda_0(n)$, we have a double root since $P_+ = P_-$. c) If $\lambda^-_c < \lambda < \lambda^+_c$, $g^-_{uuu} < 0$ and $g^-_{uP} > 0$ which is a supercritical bifurcation. d) When $\lambda = \lambda^-_c$ or $\lambda = \lambda^+_c$, $g^\pm_{uuu}$ vanishes and the canonical form is $\pm x^5 - P_- x = 0$.

$g(u, P)$ takes on a canonical form given by

$$\pm x^5 - P_- x = 0, \tag{3.69}$$

provided the fifth-order derivative is nonzero. Thus we see that at small slenderness, the pitchfork bifurcation along the P^- branch is subcritical and it transits into a supercritical bifurcation at intermediate values of slenderness. At large slenderness, the pitchfork bifurcation is subcritical. The pitchfork bifurcation is always subcritical along the P^+ branch. The full bifurcation diagrams for the elastic beam with spring support are shown in figure 3.11.

When we set $\mu = 0$, we find that

$$g^{\pm}_{uuu}(\mu = 0) = B\gamma^8 \frac{3\lambda^2\gamma^2 - 8\ell^2\gamma^4 \pm 3\gamma^2\sqrt{\lambda^2(\lambda^2 - 4\ell^2\gamma^2)}}{2\ell^2\gamma^2}. \tag{3.70}$$

In particular, we find that $g^{\pm}_{uuu}(\mu = 0) = 0$ when

$$\lambda^2_M = \frac{16}{3}\gamma^2\ell^2 = \frac{16n^2\pi^2}{3} \quad \Rightarrow \quad \frac{P^-_M}{P_E} = \frac{4}{3}n^2 \tag{3.71}$$

which agrees with [60].

3.6.2 Hopf bifurcation

In this section, we will determine the type of Hopf bifurcation along the trace$(L_2) = 0$ branches in the phase space. The analysis will follow closely that of [53]. The following change of variables are useful: $\beta P = P\pi^2/(P_E\lambda^2)$, $\alpha\beta K^2 = \lambda^2\mu^2$, $\alpha K = \lambda^2\mu$, $\alpha P = \pi^2 P/P_E$ and we have set $\ell = 1$ in our calculations. Along the Hopf branches in the phase space, we find that trace$(L_2) = 0$ and

$$\det(L_2) = -n^4\pi^4 - 2n^2\pi^2\mu + \frac{1}{2}\left(1 + \sqrt{1 - \frac{8n^2\pi^2}{\lambda^2}}\right)\lambda^2\mu = \omega_0^2. \tag{3.72}$$

We can construct two complex vectors p and q such that

$$L_2 q = i\omega_0 q, \quad L_2^T p = -i\omega_0 p, \quad \langle p, q\rangle = 1, \tag{3.73}$$

where $\langle p, q\rangle = \bar{p}_1 q_1 + \bar{p}_2 q_2$ and the overhead bar denotes complex conjugation. We find that

$$q = \left\{ -\frac{2n^2\pi^2 + 2i\omega_0}{1 + \sqrt{1 - \frac{8n^2\pi^2}{\lambda^2}}}, 1 \right\}^T, \tag{3.74}$$

$$p_1 = \left\{ \frac{2n^2\pi^2 - 2i\omega_0}{\left(1 + \sqrt{1 - \frac{8n^2\pi^2}{\lambda^2}}\right)\lambda^2\mu}, 1 \right\}^T, \tag{3.75}$$

where $\langle p_1, q\rangle = s$ and $p = p_1/\bar{s}$. Next, we will construct the expression

$$H(z,\bar{z}) = \langle p, \Phi(zq + \bar{z}\bar{q})\rangle \tag{3.76}$$

and find the coefficients g_{20}, g_{11}, and g_{21} in the formal Taylor series

$$H(z,\bar{z}) = i\omega_0 + \sum_{j+k\geq 2} \frac{1}{j!k!} g_{jk} z^j \bar{z}^k. \tag{3.77}$$

The first Lyapunov coefficient is given by

$$\ell_1 = \frac{1}{2\omega_0^2} Re(ig_{20}g_{11} + \omega_0 g_{21}). \tag{3.78}$$

If $\ell_1 < 0$ ($\ell_1 > 0$), then the equilibrium at of the Fundamental solution $(\theta, \eta) = (0, 0)$ is stable (unstable). As shown in figure 3.12, the first Lyapunov coefficient along the Hopf branch for $n = 1, 2, 3, \ldots$ is always positive and hence Hopf bifurcation is subcritical and unstable. The appearance of the Hopf bifurcation is somewhat surprising and implies the existence of (θ, η) orbits at the critical values of P and λ. However these orbits are highly delicate and unstable.

3.7 conclusion

In this Chapter we showed that the folding pattern of the bacteria coat can be explained using a simple mechanical model and our simulations were able to explain experimental observations. Our numerical studies show that as the rings shrink when the strain is larger than a critical threshold, the coat first buckles to form a symmetric wavy pattern around the cortex. This pattern then loses stability to delamination to form rucks. Also, these wrinkles do not readily attach back to the cortex, since they arise due to a subcritical (nonlinear) instability, which we modelled as a finite range

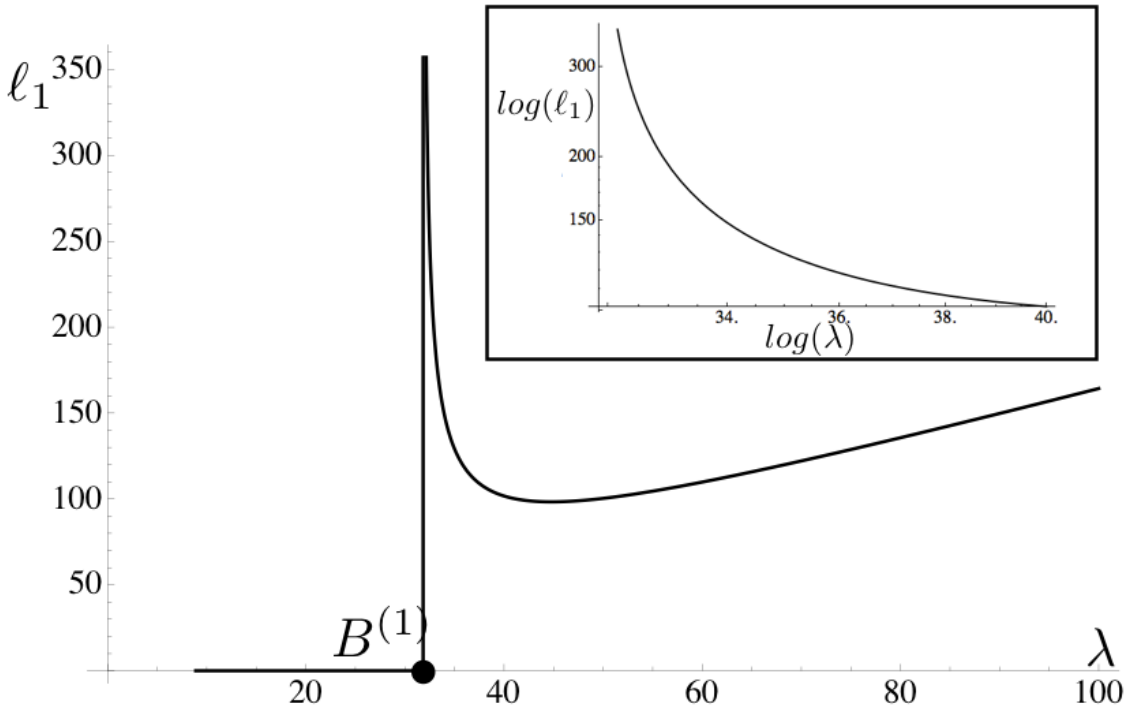

Figure 3.12: Plot of first Lyapunov coefficient as a function of slenderness. The first Lyapunov coefficient along the $n = 1$ Hopf branch for $\mu = 0.1$ and $\ell = 1$ is always positive and hence is a subcritical Hopf bifurcation. Inset: Log-log plot of first Lyapunov coefficient vs. slenderness for values near the $B^{(1)}$.

hookean spring. From these, we propose that the coat takes advantage of mechanical instabilities to fold into a wrinkled pattern during sporulation and accommodate changes in spore volume without compromising structural and biochemical integrity. Furthermore, the degree of spore swelling and coat flexibility are finely tuned such that coat shedding is resisted until unfolding is complete, thereby keeping the coat intact prior to germination. Importantly, we argue that the emergent properties of the assembled coat, such as its elastic modulus and thickness, rather than specific individual molecular components, are responsible for coat flexibility and much of the mechanism of shedding. In this view, a functional coat can be built in a large num-

ber of ways and with diverse protein components. Such freedom in design parameters could facilitate evolutionary adaptation (particularly with respect to material properties) and the emergence of the wide range of molecular compositions and arrangements found among Bacillus spore coats.

For simplicity, we have modelled the bacteria spore coat as a ring instead of the spherinder, i.e., spherical cylinder, which is a huge simplification. Clearly, there are many interesting elastic feature that is lost as we go from a two-dimensional membrane to a one-dimensional ring. In the future, we hope to do a more sophisticated numerical modelling that can reproduce experimental observations. An interesting observations that we noticed in our numerical simulations is the appearance of the wavy patterns when the circular ring buckles. We tried to analyze the bifurcation of the a ring under elastic support but due to the difficulty of the problem, we analyzed the simpler problem of an elastica on a spring support, which is still similar to our numerical model.

We study the stability of an extensible elastic beam on a flexible spring support under the action of a compressive force to illustrate how adhesion and elasticity interact with each other. Our model is based on the general Euler-Bernoulli theory of elastic beam and can be described by two differential equations. The bifurcation analysis of the ODEs was done using the methods of Liapunov-Schmidt. We found that the null space of the linearized differential equations has dimension one and on the basis of a single bifurcation equation, we obtain the bifurcation diagram. There are two types of bifurcation, namely pitchfork and hopf. For the pitchfork bifurcation, at small slenderness, the pitchfork bifurcation along the P^- branch is subcritical and

it transits into a supercritical bifurcation at intermediate values of slenderness. At large slenderness, the pitchfork bifurcation is subcritical. The pitchfork bifurcation is always subcritical along the P^+ branch. The hopf bifurcation is always subcritical and unstable

Chapter 4

Statistical Mechanics of Twisted Ribbons

4.1 Introduction

Advances in experimental techniques the past twenty years have expanded our understanding of biopolymers enormously, which in turn have stimulated progress on the theoretical side. For example, the direct manipulation of single molecules of DNA provided invaluable insights into their structure and mechanical properties [15, 16]. The relevant physics of DNA in many biological context can be described using a coarse-grained treatment, the worm-like chain (WLC) model [63, 64] where the polymer is described as a continuous flexible chain that bends smoothly under the influence of random thermal fluctuations. The WLC model has an effective bending rigidity and the polymer flexibility is determined by a single parameter, the persistence length ℓ_p which measures the tangent-tangent correlations. In addition, the

supercoiling behavior of a DNA has been investigated in the landmark experiments of Strick et al. [96, 97]. By anchoring one end of the DNA to a glass surface and the other to a magnetic bead, they were able to exert torsional control over the DNA thereby studying the statistical mechanics of DNA under fixed tension and linking number. The quantitative analysis of the supercoiling behavior of DNA begun with the seminal work of White and Fuller [106, 35, 36, 107, 108] and new experimental results in the 90s led to further exciting theoretical developments in the field [101, 65, 33, 6, 74, 62].

DNA aside, there has been a lot of recent experimental interest in other systems of biopolymers ranging from actin, microtubules to rod-like viruses. These biopolymers require a more microscopic description that goes beyond the homogenous elastic rods of the WLC model and new models proposed include the railway track model of Everaers-Bundschuh-Kremer (EBK) [32, 57, 39] and more recently the Sadowsky ribbon [85, 94, 37]. In these microscopic models, the interaction between the bend and twist degrees of freedom is inherent, which is fundamentally different from the WLC model where the twist degrees of freedom is accounted by adding extra terms to the free energy. In an earlier report [37], we showed that the tangent-tangent correlation function exhibits an oscillatory decay at any finite temperature, implying an underlying helical structure even in absence of any natural twist at zero temperature. The Sadowsky ribbon is isometric to a flat strip at any temperature and thus bends when twisted. In this work, we will present a detailed description of our theoretical and numerical calculations of the statistical mechanics of the Sadowsky ribbon under the effect of external force and torsion.

4.2 Physical Model

Let us consider a rectangular strip of length L, width w and thickness h. We will assume the strip to be inextensible so that it can store elastic energy exclusively through bending. The elastic energy can be expressed in the usual form [61] given by

$$E = \frac{1}{2}D \int dA\,[(\kappa_1 + \kappa_2)^2 - 2(1-\nu)\kappa_1\kappa_2], \tag{4.1}$$

where $D = \frac{Eh^3}{12(1-\nu^2)}$ is the bending rigidity, E the Young modulus and ν the Poisson ratio of the material. κ_1 and κ_2 are the principal curvatures. Next, let us assume that the plate is developable (zero Gauss curvature). Thus the smaller principal curvature κ_2 is zero everywhere and the elastic energy reduce to the simple form:

$$E = \frac{1}{2}D \int dA\,\kappa_1^2 \tag{4.2}$$

We can rewrite (4.2) in terms of the curvature κ and the torsion τ of the centerline of the ribbon:

$$\begin{aligned} E &= \frac{1}{2}D \int_0^L ds\,\kappa^2 \left(1 + \frac{\tau^2}{\kappa^2}\right)^2 \int_{-\frac{w}{2}}^{\frac{w}{2}} dt\,\frac{\kappa^2}{\kappa^2 + (\tau'\kappa - \tau\kappa')t} \\ &= \frac{1}{2}D \int_0^L ds\,\frac{(\kappa^2+\tau^2)^2}{\tau'\kappa - \tau\kappa'}\,\log\left[\frac{\kappa^2 + \frac{w}{2}(\tau'\kappa - \tau\kappa')}{\kappa^2 - \frac{w}{2}(\tau'\kappa - \tau\kappa')}\right]. \end{aligned} \tag{4.3}$$

Assuming that $L \gg w$, 4.3 simplifies to

$$E = \frac{1}{2}Dw \int_0^L ds\,\frac{(\kappa^2+\tau^2)^2}{\kappa^2}. \tag{4.4}$$

Technical details of the derivation are discussed in the Appendix G. The nonlinear coupling between curvature and torsion in 4.4 implies that an inextensible ribbon can bend without twisting ($\tau = 0$, $\kappa \neq 0$), but cannot twist without bending ($\tau \neq 0 \rightarrow \kappa \neq 0$).

Consider the special case of the Sadowsky ribbon whose base configuration is a helical band whose centerline has curvature κ_0 and torsion τ_0. Calling R and C the radius and the pitch of such a helical reference centerline, κ_0 and torsion τ_0 are given by:

$$\kappa_0 = \frac{R}{C^2 + R^2}, \qquad \tau_0 = \frac{C}{C^2 + R^2},$$

both constant across the system. The coefficient of the first and second fundamental form of the base configuration can be calculated straightforwardly:

$$g^0_{ss} = 1, \qquad g^0_{st} = \frac{\tau_0}{\kappa_0}, \qquad g^0_{tt} = 1 + \frac{\tau_0^2}{\kappa_0^2},$$

$$b^0_{ss} = \kappa_0, \qquad b^0_{st} = b^0_{tt} = 0,$$

from which the spontaneous principal curvature are given by:

$$\kappa^0_1 = \kappa_0 \left(1 + \frac{\tau_0^2}{\kappa_0^2}\right), \qquad \kappa^0_2 = 0.$$

The bending energy ((4.2)), including a spontaneous principle curvature, becomes thus:

$$\begin{aligned} E &= \frac{1}{2} D \int dA \, \left(\kappa_1 - \kappa^0_1\right)^2 \\ &= \frac{1}{2} D \int_0^L ds \int_{-\frac{w}{2}}^{\frac{w}{2}} dt \, f \left[\frac{\kappa}{f}\left(1 + \frac{\tau^2}{\kappa^2}\right) - \kappa^0_1\right]^2. \end{aligned}$$

Now, calling:

$$\psi = \kappa \left(1 + \frac{\tau^2}{\kappa^2}\right), \qquad \varphi = \frac{\tau'\kappa - \tau\kappa'}{\kappa^2},$$

the integral over t becomes:

$$\begin{aligned} &\int_{-\frac{w}{2}}^{\frac{w}{2}} dt \, \frac{\left[\psi - \kappa^0_1(1 + \varphi\, t)\right]^2}{1 + \varphi\, t} \\ &= w\kappa^0_1 \left(\kappa^0_1 - 2\psi\right) + \frac{\psi^2}{\varphi} \log\left[\frac{1 + \frac{w}{2}\varphi}{1 - \frac{w}{2}\varphi}\right], \end{aligned}$$

the second term on the right-hand side is precisely the Wunderlich functional (4.3). Thus, in the limit $w/L \ll 1$ the above expression becomes:

$$w\kappa_1^0\left(\kappa_1^0 - 2\psi\right) + w\psi^2 = w(\psi - \kappa_1^0)^2,$$

from which a generalized expression of the Sadowsky functional for a *naturally helical* developable ribbon can be found in the form:

$$E = \frac{1}{2}Dw\int_0^L ds\,\left(\frac{\kappa^2+\tau^2}{\kappa} - \kappa_1^0\right)^2. \tag{4.5}$$

The above expression implies a continuous set of zero energy configurations. To illustrate this point, we can restrict on the class of deformations that preserve the preferential helical shape. Thus, in place of κ and τ, we can adopt as independent variable the radius r and the pitch c of the deformed ribbon. With this choice the generalized Sadowsky functional becomes simply:

$$E = \frac{1}{2}Dw\int_0^L ds\,\left(\frac{1}{r} - \frac{1}{R}\right)^2 \tag{4.6}$$

which *doesn't depend on the pitch of the helix!*. In other words, in the limit of $w \ll L$, any deformation that varies the pitch of the centerline while leaving unchanged its radius of curvature costs zero elastic energy. To get a better feeling of this somewhat surprising result one can try to construct a paper model of a helical ribbon by rolling a paper strip around a cylinder. If we now try to untwist the paper ribbon by increasing the pitch while keeping the radius of curvature constant, we can experience that such a deformation costs a very little energy (zero if nothing by the elasticity of the strip is taken into account). This special class of geometrical transformations consisting in changing the pitch a helical centerline without changing the radius of curvature is in

fact a type of transformation that preserve both the first and the second fundamental form of the surface.

We study the effect of such microscorpic ribbon under the effect of a force $\boldsymbol{F} = F\boldsymbol{e}_z$ and a torque Ω. The two stresses on the ribbon introduces two additional energy terms [63, 64, 68, 69]:

$$E_f = -\boldsymbol{F} \cdot \int_0^L ds\, \boldsymbol{t}(s) = -F \int_0^L ds\, t_z(s), \tag{4.7}$$

and

$$E_t = -2\pi\Omega Lk, \tag{4.8}$$

where Lk is the linking number. From the theory of elasticity, we know that a macroscopic stretched elastic rod remains straight as we apply increasing torque to the ends, then buckle at a critical value of torque $\Omega_c = 2\sqrt{FAk_BT}$ [58, 68, 69]. This critical value of torque increases with the applied stretching force. Microscopic rods behave similar in that it can bend to relieve stresses. However, more importantly, it is under constant thermal fluctuations which prevents the rod from being straight. Every Fourier mode of its shape is excited according to the equipartition theorem and even small applied torque can result lead to deviation from a straight line. In our simulations, we will vary Ω so that we obtain the desired linking number Lk.

4.3 Ribbon Theory

Let C and A be two space curves in one-to-one correspondence. This means that every point p on C is connected to a point q on A and that no point on either curve is doubly connected. The linking number Lk between two curves A and C can be

represented using Gauss's formula:

$$Lk(A,C) = \frac{1}{4\pi}\int_A\int_C \frac{(d\boldsymbol{r}_A \times d\boldsymbol{r}_C)\cdot(\boldsymbol{r}_A - \boldsymbol{r}_C)}{|\boldsymbol{r}_A - \boldsymbol{r}_C|^3}. \tag{4.9}$$

$Lk(A,C)$ is topological invariant that calculates how much a curve A "links" around another curve C. As a result of Călugăreanu-White-Fuller theorem [36, 35, 107, 108, 24], the linking number $Lk(A,C)$ can be expressed by a sum of local strain field (the twist, Tw) and a global configurational integral (writhe, Wr), namely

$$Lk = Tw + Wr. \tag{4.10}$$

The writhe of a curve C, $Wr(C)$, is given by

$$Wr(C) = \frac{1}{4\pi}\int_C\int_C \frac{(d\boldsymbol{r}_1 \times d\boldsymbol{r}_2)\cdot(\boldsymbol{r}_1 - \boldsymbol{r}_2)}{|\boldsymbol{r}_1 - \boldsymbol{r}_2|^3}, \tag{4.11}$$

which is a non-local formula involving a double integral around the closed curve C. Wr measures the non-planarity of the axis curve.

Tw measures how much the ribbon is twisted about its own axis. We denote the twist of curve A about curve C by $Tw(A,C)$ and in a similar manner, the twist of C about A by $Tw(C,A)$. The twist is a property of two ordered curves and of a one-to-one correspondence between them and cannot be calculated for a single curve in isolation [107, 108]. Let $\boldsymbol{z}_{CA}$ be a vector joining a point in C to its corresponding point on A. This vector is known as the correspondence vector and the surface generated by all the correspondence vectors is known as the correspondence surface. Let $\boldsymbol{t}_C$ be the unit tangent vector to C. Since $\boldsymbol{t}_C$ and $\boldsymbol{z}_{CA}$ are in general not orthogonal, we can define a unit vector $\boldsymbol{v}_{CA}$ that lies in the plane spanned by $\boldsymbol{z}_{CA}$ and $\boldsymbol{t}_C$ and is perpendicular to $\boldsymbol{t}_C$. Then the twist of A about C is

$$Tw(A,C) = \frac{1}{2\pi}\int_C [\boldsymbol{t}_C \times \boldsymbol{v}_{CA}]\cdot d\boldsymbol{v}_{CA}. \tag{4.12}$$

Similarly, we define the twist of C about A as

$$Tw(C,A) = \frac{1}{2\pi}\int_A [\boldsymbol{t}_A \times \boldsymbol{v}_{AC}] \cdot d\boldsymbol{v}_{AC}. \tag{4.13}$$

The form of 4.12 and 4.13 implies that the twist is additive, i.e., the total twist is equal to the sum of the twists of its constituent parts.

The two quantities $Tw(A,C)$ and $Tw(C,A)$ are generally not equal to one another and the order of A and C matters. However, the linking number is independent of the order of the curves as evident from 4.9, so $Lk(A,C) = Lk(C,A)$ and it follows that

$$Tw(A,C) + Wr(C) = Tw(C,A) + Wr(A). \tag{4.14}$$

Thus if the linking number is fixed, then the chain is only allowed to distribute the topologically invariant Lk between the degrees of freedom associated with Tw and Wr.

In general, Lk is defined only for closed loops. Since we have an open chain with both ends held at fixed orientations, we can draw a fixed, imaginary path that connects the two ends at infinity to form a closed contour as shown in 4.1 [65, 68, 69, 75]. Choosing the return contour such that $Lk = 0$ when the rod is straight and unstressed, we can then apply CFW theorem $Lk = Tw + Wr$, where the right hand side is calculated only along the actual chain. Whenever a straight rod becomes bend or twisted, $Lk \neq 0$ and it is supercoiled.

Let us then pick the centerline ($t = 0$) of the ribbon $\boldsymbol{x}(s)$ to be C and one of the edge ($t = w/2$) to be A, which we will call the auxiliary curve. In this case, we find that

$$\boldsymbol{r}'_A = \boldsymbol{R}'(s, \frac{w}{2}) = \boldsymbol{t} + \frac{w}{2}\left(\boldsymbol{b}' + \frac{\tau}{\kappa}\boldsymbol{t}' + \frac{\tau'\kappa - \tau\kappa'}{\kappa^2}\boldsymbol{t}\right). \tag{4.15}$$

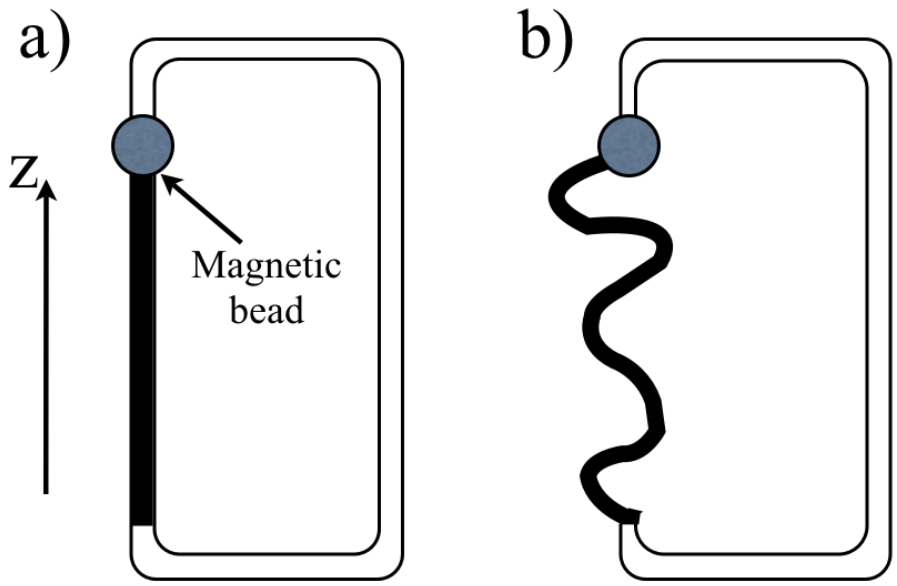

Figure 4.1: a) A flat ribbon with zero linking number Lk. The black portion represents an actual straight ribbon and the white portion represent the imaginary return loop, forming a closed contour. In actual experiment, one end of the DNA is held fixed while a magnetic bead is typically attached to the other end of the DNA to allow for mechanical control. b) Situation where the ribbon becomes distorted. The end of the ribbon that is attached to the magnetic bead may not be flat as in the undistorted configuration in (a), and in order to join the end to the imaginary contour properly may incur an additional twist of at most $\pm 1/2$, which is neglected in the numerics.

Using the Frenet-Serret equations, we find that

$$\boldsymbol{r}'_A = \boldsymbol{t}\left(1 + \frac{w(\tau'\kappa - \tau\kappa')}{2\kappa^2}\right), \tag{4.16}$$

and it follows that

$$\boldsymbol{t}_A = \boldsymbol{t}_C = \boldsymbol{t}. \tag{4.17}$$

Let us pick $\boldsymbol{v}_{AC} = \boldsymbol{b}$, then we find that the twist of C about A is

$$Tw(C, A) = \frac{1}{2\pi}\int_A ds\,[\boldsymbol{t} \times \boldsymbol{b}] \cdot \boldsymbol{b}' = \int_A \frac{ds}{2\pi}\,\tau. \tag{4.18}$$

In a similar fashion, we can calculate the twist of A about C. In this case, using

$\boldsymbol{v}_{CA} = -\boldsymbol{v}_{AC} = -\boldsymbol{b}$, we find that

$$Tw(A, C) = \int_A \frac{ds}{2\pi}\, \tau, \tag{4.19}$$

and hence $Tw(C, A) = Tw(A, C)$. The choice of $t = w/2$ is arbitrary and the preceding calculations work for any t and hence we can conclude that the twist of a developable ribbon is given by total torsion of the ribbon (divided by 2π).

4.4 Numerical Methods

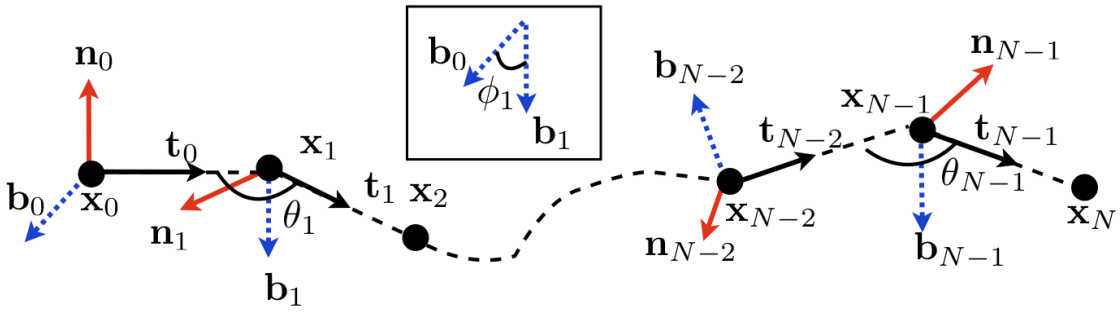

Figure 4.2: A discrete framed curve consisting of $N+1$ vertices $\boldsymbol{x}_0, \boldsymbol{x}_1, ..., \boldsymbol{x}_N$, and an orthogonal Frenet frame $\boldsymbol{F}_i = (\boldsymbol{n}_i, \boldsymbol{b}_i, \boldsymbol{t}_i)$, $i = 1, ..., N$. Angle between $\boldsymbol{t}_{i-1}$ and $\boldsymbol{t}_i$ is θ_i. The distance between adjacent vertices is a, i.e. $|\boldsymbol{x}_{i+1} - \boldsymbol{x}_i| = a$. Inset: The angle between $\boldsymbol{b}_0$ and $\boldsymbol{b}_1$ is ϕ_1.

Let us discretize the ribbon as a chain of total length L with $N+1$ vertices $\boldsymbol{x}_i = \{\boldsymbol{x}_0, \boldsymbol{x}_1, ..., \boldsymbol{x}_N\}$ separated by a fixed length a as shown in 4.2. For each pair of nearest neighbor vertices $\boldsymbol{x}_{i-1}, \boldsymbol{x}_i$, we can introduce a unit tangent vector

$$\boldsymbol{t}_i = \frac{\boldsymbol{x}_i - \boldsymbol{x}_{i-1}}{|\boldsymbol{x}_i - \boldsymbol{x}_{i-1}|}. \tag{4.20}$$

If $\boldsymbol{t}_{i-1}$ and $\boldsymbol{t}_i$ are not parallel, the binormal and normal vector can be given by

$$\boldsymbol{b}_i = \frac{\boldsymbol{t}_{i-1} \times \boldsymbol{t}_i}{|\boldsymbol{t}_{i-1} \times \boldsymbol{t}_i|}, \tag{4.21}$$

and

$$\boldsymbol{n}_i = \boldsymbol{b}_i \times \boldsymbol{t}_i. \tag{4.22}$$

Otherwise, we simply define $\boldsymbol{b}_i = \boldsymbol{b}_{i-1}$ and $\boldsymbol{n}_i = \boldsymbol{n}_{i-1}$. Let us define the discrete bending angle θ_i, $(-\pi < \theta_i \leq \pi)$ by

$$\cos\theta_i = \boldsymbol{t}_i \cdot \boldsymbol{t}_{i-1}, \tag{4.23}$$

and the discrete bond angle ϕ_i, $(-\pi < \phi_i \leq \pi)$ by

$$\cos\phi_i = \boldsymbol{b}_i \cdot \boldsymbol{b}_{i-1}. \tag{4.24}$$

The curvature at vertex i is given by

$$\kappa_i^2 = \frac{|\boldsymbol{t}_i - \boldsymbol{t}_{i-1}|^2}{a^2} = \frac{2(1-\cos\theta_i)}{a^2}, \tag{4.25}$$

and the torsion is

$$\tau_i^2 = \frac{|\boldsymbol{b}_i - \boldsymbol{b}_{i-1}|^2}{a^2} = \frac{2(1-\cos\phi_i)}{a^2}. \tag{4.26}$$

At each vertex, there is an orthonormal discrete Frenet frame $\boldsymbol{F}_i = (\boldsymbol{t}_i, \boldsymbol{n}_i, \boldsymbol{b}_i)$, $i = 1, ..., N$. The Frenet frames $\boldsymbol{F}_i$ are orthogonal 3×3 matrices, whose column vectors are $\boldsymbol{t}_i, \boldsymbol{n}_i$ and $\boldsymbol{b}_i$. We can write down an iterative relation between two adjacent discrete Frenet frame [37, 83]

$$\boldsymbol{F}_i = \boldsymbol{F}_{i-1}\boldsymbol{R}_i \tag{4.27}$$

where

$$\boldsymbol{R}_i = \begin{pmatrix} \cos\theta_i & -\sin\theta_i & 0 \\ \sin\theta_i\cos\phi_i & \cos\theta_i\cos\phi_i & -\sin\phi_i \\ \sin\theta_i\sin\phi_i & \cos\theta_i\sin\phi_i & \cos\phi_i \end{pmatrix}. \tag{4.28}$$

We note that $\boldsymbol{t}_i \cdot \boldsymbol{n}_{i-1} = (R_i)_{21} = \sin\theta_i \cos\phi_i$ and $\boldsymbol{t}_i \cdot \boldsymbol{b}_{i-1} = (R_i)_{31} = \sin\theta_i \sin\phi_i$. If we set $\boldsymbol{F}_0 = (\boldsymbol{e}_z, \boldsymbol{e}_x, \boldsymbol{e}_y)$, then $\boldsymbol{F}_i$ along the discrete chain can be calculated iteratively if we know all the discrete bending θ's and bond angles ϕ's since

$$\boldsymbol{F}_i = \boldsymbol{F}_0 \boldsymbol{R}_1 \cdots \boldsymbol{R}_i. \tag{4.29}$$

In order to test our model, we performed a Monte Carlo simulation using the discretized versions of the various expressions derived in the previous section by making the following discretization:

$$\int ds \to \sum a. \tag{4.30}$$

We find that the energy expressions become

$$\frac{E_{ribbon}}{k_B T} = \frac{Dw}{a k_B T} \sum_{i=1}^{N-1} \frac{[(1-\cos\theta_i) + (1-\cos\phi_i)]^2}{(1-\cos\theta_i)}, \tag{4.31}$$

$$\frac{E_f}{k_B T} = -\frac{Fa}{k_B T} \sum_{i=0}^{N} t_i^z, \tag{4.32}$$

and

$$\frac{E_t}{k_B T} = -\frac{\Omega}{k_B T} Lk = -\frac{\Omega}{k_B T}(Tw + Wr). \tag{4.33}$$

The twist is given by

$$Tw = \frac{1}{2\pi} \sum_{i=1}^{N-1} \arccos(\boldsymbol{b}_{i-1} \cdot \boldsymbol{b}_i)\, \mathrm{sign}(\boldsymbol{b}_{i-1} \cdot \boldsymbol{t}_i), \tag{4.34}$$

where the positive direction of rotation is defined by the right hand rule, i.e. $\mathrm{sign}((\boldsymbol{b}_{i-1} \times \boldsymbol{b}_i) \cdot \boldsymbol{t}_{i-1})$. Since $\boldsymbol{b}_i$ is proportional to $\boldsymbol{t}_{i-1} \times \boldsymbol{t}_i$, we find that $\boldsymbol{b}_{i-1} \times (\boldsymbol{t}_{i-1} \times \boldsymbol{t}_i) = \boldsymbol{t}_{i-1}(\boldsymbol{b}_{i-1} \cdot \boldsymbol{t}_i) - \boldsymbol{t}_i(\boldsymbol{b}_{i-1} \cdot \boldsymbol{t}_{i-1}) = \boldsymbol{t}_{i-1}(\boldsymbol{b}_{i-1} \cdot \boldsymbol{t}_i)$, where we have used the vector triple product identity. Thus, we arrive at $\mathrm{sign}((\boldsymbol{b}_{i-1} \times \boldsymbol{b}_i) \cdot \boldsymbol{t}_{i-1}) = \mathrm{sign}(\boldsymbol{b}_{i-1} \cdot \boldsymbol{t}_i)$. The

writhe can be expressed as a double sum:

$$Wr = \frac{1}{2\pi} \sum_{i=2}^{N-1} \sum_{j<i} \Omega_{ij}, \tag{4.35}$$

where Ω_{ij} is the Gauss integral along the segments $a\boldsymbol{t}_i$, $a\boldsymbol{t}_j$ and is the discrete version of

$$d\Omega(\boldsymbol{r}_1, \boldsymbol{r}_2) = \frac{(d\boldsymbol{r}_1 \times d\boldsymbol{r}_2) \cdot (\boldsymbol{r}_1 - \boldsymbol{r}_2)}{|\boldsymbol{r}_1 - \boldsymbol{r}_2)|^3}. \tag{4.36}$$

From inspecting either 4.11 or 4.36, we see that $\Omega_{ij} = \Omega_{ji}$ and $\Omega_{ii} = \Omega_{i,i+1} = 0$. See Appendix H.2 on how to calculate Ω_{ij}.

We fixed one end of the chain, i.e. $\boldsymbol{F}_0$ while the other end is free to take on arbitrary conformations. This is similar to the approach of Moroz and Nelson [68, 69] where the desired linking number is achieved by tuning the applied torque on the DNA. Let us define three new dimensionless parameters, the normalized temperature, normalized force and normalized torque

$$\Lambda = \frac{ak_BT}{Dw}, \quad f = \frac{Fa^2}{Dw}, \quad \Gamma = \frac{\Omega a}{Dw}. \tag{4.37}$$

Consider a randomly selected discrete chain composing of $N = 100$ segments of length a at temperature Λ, force f and torque Γ and its conformation is updated using pivot moves sequentially along the chain. The starting discrete Frenet frame, $\boldsymbol{F}_0$, is fixed and during the first step, we randomly picked two new angles θ_1 and ϕ_1, and update the positions of the chain using 4.29. This configuration is accepted via a Metropolis algorithm. Then we proceed to the next link and randomly picked two new angles θ_2 and ϕ_2 and repeat the process. This procedure terminates when we reach the end of the chain and this constitutes one Monte Carlo sweep. For our simulations, we performed 10^6 Monte Carlo sweeps per chain, the first half of which

is devoted to equilibration. Since $Dw/k_BT \sim 50$nm and $a \sim 50$nm, we expect $\Lambda \sim 1$. Also, in the WLC experiments, $F \sim 0.01 - 10\,[k_BT/\text{nm}]$, so we expect $f \sim 0.5 - 500$. In our simulations, we used $\Omega \sim -1$ to 1, in order to get the range of Lk that we want.

4.5 Theoretical Methods

The partition function of the Sadowsky ribbon is given by

$$Z_N = \int D[\boldsymbol{t}(s)]D[\boldsymbol{b}(s)] \exp\left(-\frac{Dw}{2k_BT}\int ds(\kappa^2 + 2\tau^2 + \tau^4/\kappa^2)\right). \tag{4.38}$$

The exact calculation of this partition using path integral is hopeless. Fortunately, when we discretize Z_N, we find that the the partition function factorizes into N single node partition, namely $Z_N = z_1^N$ with

$$z_1 = \int \frac{d\Omega}{4\pi} e^{-\frac{1}{2}Ba^2(\kappa^2+2\tau^2+\tau^4/\kappa^2)}, \tag{4.39}$$

and we have defined a new variable $B = Dw/(ak_BT)$. The coupling term between the curvature and torsion makes the analytical calculation much complicated. We shall employ a trick involving Gaussian integral to remove the coupling:

$$e^{\frac{-Ba^2\tau^4}{2\kappa^2}} = \sqrt{\left(\frac{Ba^2\kappa^2}{2\pi}\right)}\int_{-\infty}^{\infty} dy e^{-\frac{1}{2}Ba^2(\kappa^2y^2+2i\tau^2y)}. \tag{4.40}$$

With this substitution, the single node partition function z_1 becomes

$$\begin{aligned} z_1 &= \left(\frac{B}{\pi}\right)^{1/2}\int_{-\infty}^{\infty} dy \int \frac{d\Omega}{4\pi}(1-\cos\theta)^{1/2} e^{-B[\lambda(1-\cos\theta)+\mu(1-\cos\phi)]} \\ &= \left(\frac{B}{4\pi}\right)^{1/2}\int_{-\infty}^{\infty} dy \frac{e^{-B\mu} I_0(B\mu)\gamma(\frac{3}{2}, 2B\lambda)}{(B\lambda)^{3/2}}, \end{aligned} \tag{4.41}$$

where $\lambda = (1 + y^2)$, $\mu = 2(1 + iy)$, I_0 is the modified Bessel function of zeroth order and γ is the incomplete gamma function. We now have the machinery to calculate the single node ensemble average

$$\langle \cdot \rangle = z_1^{-1} \int \frac{d\Omega}{4\pi} (\cdot) e^{-\frac{1}{2} Ba^2(\kappa^2 + 2\tau^2 + \tau^4/\kappa^2)}. \tag{4.42}$$

This expression allows us to calculate the various quantities in $\boldsymbol{R}$, from which we can extract useful quantities such as the persistence lengths and the wave number k

The tangent-tangent and binormal-binormal correlation functions from the iterated transfer matrix, namely [37]

$$\langle \boldsymbol{t}_0 \cdot \boldsymbol{t}_p \rangle = \langle \boldsymbol{R}_1 \boldsymbol{R}_2 \cdots \boldsymbol{R}_p \rangle_{11}, \tag{4.43}$$

and

$$\langle \boldsymbol{b}_0 \cdot \boldsymbol{b}_p \rangle = \langle \boldsymbol{R}_1 \boldsymbol{R}_2 \cdots \boldsymbol{R}_p \rangle_{33}. \tag{4.44}$$

Since the energy (4.31) is a sum over the individual segments, the Boltzmann factor $\exp(-E/k_BT)$ in the partition function is factorable and $\langle \boldsymbol{R}_1 \boldsymbol{R}_2 \cdots \boldsymbol{R}_p \rangle = \langle \boldsymbol{R} \rangle^p$. For sufficiently large separation, the behavior of the correlation functions will be dictated by the largest eigenvalue in the spectrum of $\boldsymbol{R}$. Assuming that the system is invariant for chirality flipping $\langle \sin \phi \rangle = 0$, the transfer matrix $\boldsymbol{R}$ becomes block diagonal. The binormal-binormal correlation function exhibits an exponential decay

$$\langle \boldsymbol{b}_0 \cdot \boldsymbol{b}_p \rangle = \langle \cos \phi \rangle^p = e^{-s/\ell_\tau}, \tag{4.45}$$

where $s = pa$ and the torsional persistence length is given by

$$\ell_\tau = -a(\ln \langle \cos \phi \rangle)^{-1}. \tag{4.46}$$

The tangent-tangent correlation function depends on the eigenvalues of the remaining block 2×2 matrix which has characteristic equation

$$\lambda^2 - b\lambda + c = 0, \tag{4.47}$$

where $b = \langle \cos\theta \rangle + \langle \cos\theta \cos\phi \rangle$ and $c = \langle \cos\theta \rangle \langle \cos\theta \cos\phi \rangle + \langle \sin\theta \rangle \langle \sin\theta \cos\phi \rangle$. The eigenvalues are

$$\lambda_\pm = \frac{b \pm \sqrt{\Delta}}{2}, \tag{4.48}$$

where $\Delta = b^2 - 4c$. It has been shown [37] that $\Delta < 0 \ \forall T > 0$ and therefore the eigenvalues are always complex and

$$\langle \boldsymbol{t}_0 \cdot \boldsymbol{t}_p \rangle = e^{-s/\ell_p} \cos ks, \tag{4.49}$$

with $k = a^{-1} \arctan(\sqrt{-\Delta}/b)$ and $\ell_p = -2a(\ln c)^{-1}$. The fact that the tangent-tangent correlation function is always oscillatory $\forall T > 0$ implies the presence of an underlying helical structure that persists at any finite temperature.

In the low temperature ($\Lambda \ll 1$) limit, the persistence length is given by [37]

$$\ell_p = \left(\frac{75}{64} - \frac{25}{9\pi} \right)^{-1} \frac{Dw}{k_B T} \approx 3.476 \frac{Dw}{k_B T}, \tag{4.50}$$

$$\ell_\tau = \frac{32}{5} \frac{Dw}{k_B T} = 6.4 \frac{Dw}{k_B T}, \tag{4.51}$$

and

$$k = \frac{5}{3} \sqrt{\frac{2}{\pi a} \frac{k_B T}{Dw}} \approx 1.33 \sqrt{\frac{k_B T}{aDw}}. \tag{4.52}$$

As a consequence of the coupling between the curvature and torsion, the persistence length is a factor 3.476 larger than the WLC at the same temperature.

The mean square end to end distance of the Sadowsky ribbon can be calculated as follows:

$$\begin{aligned}
\langle r^2 \rangle &= a^2 \sum_{i,j} \langle \boldsymbol{t}_i \cdot \boldsymbol{t}_j \rangle \\
&= a^2 \frac{1}{a^2} \int_0^{Na} ds \int_0^{Na} ds' \exp(\frac{-|s-s'|}{\ell_p}) \cos k|s-s'| \\
&\approx Na \int_{-\infty}^{\infty} d\Delta s \, \exp(-|\Delta s|/\ell_p) \cos k|\Delta s| \\
&= 2Na \frac{\ell_p}{1+\ell_p^2 k^2} = L \frac{2\ell_p}{1+\ell_p^2 k^2}.
\end{aligned} \tag{4.53}$$

In the low temperature limit, we find that

$$\langle r^2 \rangle \approx L \, \frac{6.95 \frac{Dw}{k_B T}}{1 + 21.368 \frac{Dw}{a k_B T}}. \tag{4.54}$$

The closely related Kuhn length, b^{SR}, is given by

$$b^{SR} = \frac{2\ell_p}{1+\ell_p^2 k^2}. \tag{4.55}$$

which is distinctly different from the WLC, where $b^{WLC} = 2\xi$, where ξ is the persistence length of the WLC. Refer to Appendix F for more information.

Consider the force extension curve of the Sadowsky ribbon under a small applied force in the z-direction. Using F.29, we find that

$$\begin{aligned}
z &\approx \frac{1}{3} \frac{F}{k_B T} \langle r^2 \rangle + O(F^2) \\
&\approx \frac{1}{3} \frac{F}{k_B T} L \frac{2\ell_p}{1+\ell_p^2 k^2},
\end{aligned} \tag{4.56}$$

or alternatively,

$$\frac{Fa}{k_B T} = \frac{3a}{2} \frac{1+\ell_p^2 k^2}{\ell_p} \frac{z}{L}. \tag{4.57}$$

Next, let us consider the force extension curves at large $\boldsymbol{F}$ ($F\ell_p/k_BT \gg 1$). In the continuum model, the Sadowsky ribbon is given by

$$E = \frac{1}{2}Dw\int_0^L \left(\left(\frac{d\boldsymbol{t}}{ds}\right)^2 + 2\left(\frac{d\boldsymbol{b}}{ds}\right)^2 + \frac{\left(\frac{d\boldsymbol{b}}{ds}\right)^4}{\left(\frac{d\boldsymbol{t}}{ds}\right)^2} \right) ds - \boldsymbol{F}\cdot\int_0^L \boldsymbol{t}(s)ds. \tag{4.58}$$

In this limit, we can approximate the tangent vector by

$$\boldsymbol{t}(s) = \begin{pmatrix} t_x(s) \\ t_y(s) \\ \sqrt{1-t_x^2-t_y^2} \end{pmatrix} \approx \begin{pmatrix} t_x(s) \\ t_y(s) \\ 1 \end{pmatrix}. \tag{4.59}$$

In which case the energy can be written as

$$\begin{aligned} E \;\approx\; & \frac{1}{2}\int_0^L \left\{ Dw[(dt_x ds)^2 + (dt_y ds)^2] + F(t_x^2+t_y^2)\right\} ds - FL \\ & + \frac{1}{2}\int_0^L 2Dw[(db_x/ds)^2 + (db_y/ds)^2 + (db_z/ds)^2]ds \\ & + \frac{1}{2}\int_0^L Dw\frac{[(db_x/ds)^2 + (db_y/ds)^2 + (db_z/ds)^2]^2}{[(dt_x/ds)^2 + (dt_y/ds)^2]}ds \end{aligned} \tag{4.60}$$

There is not much we can do at this point due to the coupling between $\boldsymbol{t}$ and $\boldsymbol{b}$. However, if we assume that in this regime, the physics is described by an effective Hamiltonian where $\boldsymbol{t}$ and $\boldsymbol{b}$ are uncoupled but with new renormalized parameters $Dw \to \Phi$ then we can use the same technique for WLC (See steps leading to F.43 in Appendix F) to find:

$$\frac{z}{L} \approx 1 - \frac{1}{2\pi}\int_{-\infty}^{\infty} dq \frac{k_BT}{\Phi q^2 + F} = 1 - \frac{k_BT}{2\sqrt{F\Phi}}. \tag{4.61}$$

The effective parameter Φ can be fitted from simulation.

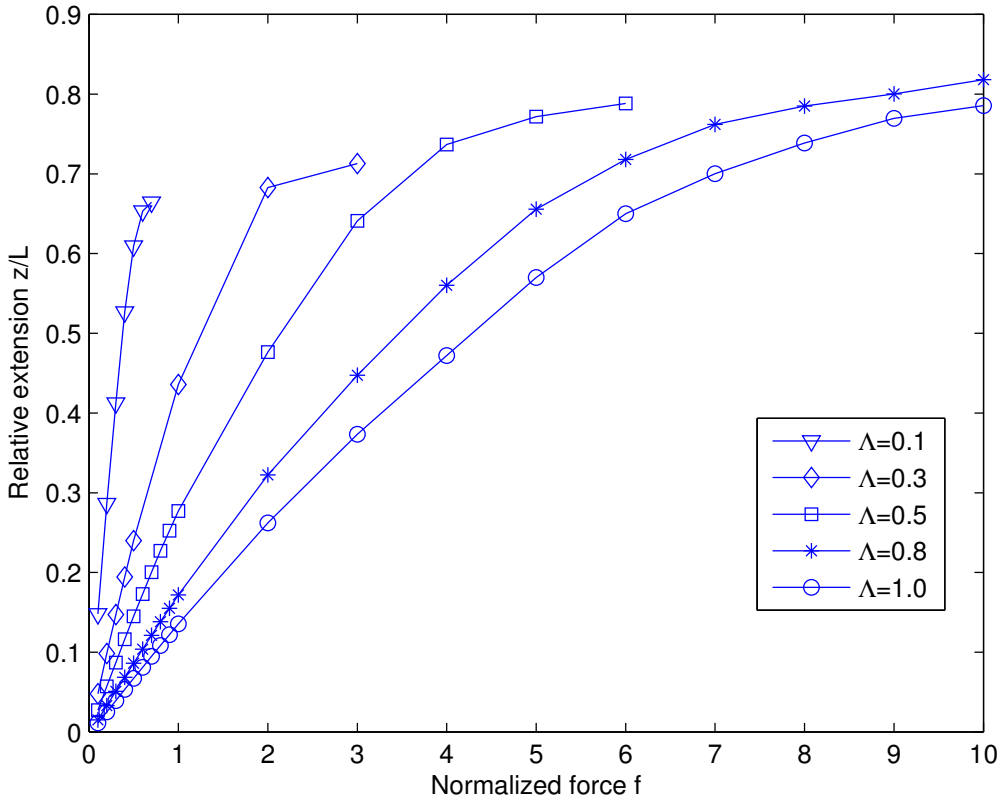

Figure 4.3: Simulated extension of a torque-free ($\Gamma = 0$) ribbon at different normalized temperatures Λ. As the temperature increases, it becomes harder to stretch the ribbon. The relative extension vary linearly with applied force at low applied forces (Curie's law).

4.6 Results and Discussions

Let us first consider the case of the ribbon under an applied force without any external torque. As the temperature Λ increases, it becomes harder to stretch the ribbon, in agreement with the wormlike chain (WLC) model in earlier studies. At low stretching forces, the relative extension vary linearly with the applied force, i.e.

Curie's law:

$$\frac{f}{\Lambda} = \frac{Fa}{k_B T} = 7\frac{z}{L}. \tag{4.62}$$

This is very different from the WLC which behaves like

$$\frac{Fa}{k_B T} = \frac{3}{2}\frac{z}{L}. \tag{4.63}$$

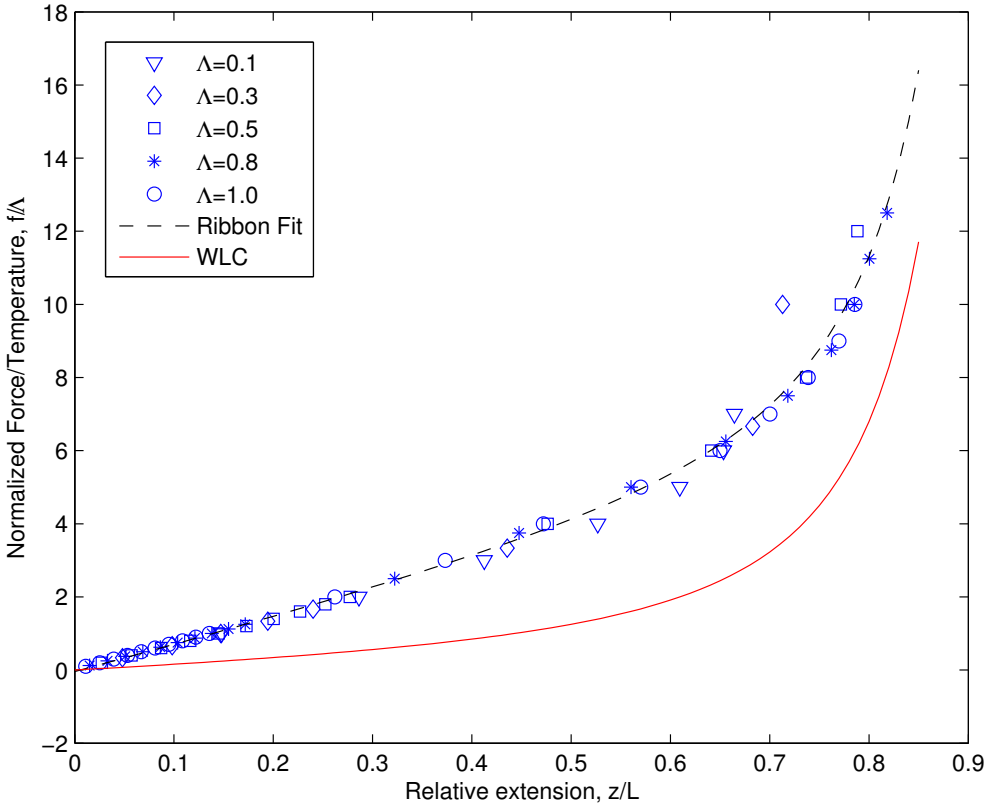

Figure 4.4: Force versus extension curves. The data for different Λ's collapses onto a single curve . The black dotted curve is the best fit to the data. The interpolation formula for the WLC is shown in red.

The Sadowsky ribbon is evidently harder to stretch compared to the WLC. It requires a much greater force in order to realize a given extension. At low extension,

a ribbon behaves as a spring, that is, it obeys a Hooke relation: $F = kz$, and the spring constant depends linearly on the temperature. At high forces, the ribbon prefers to be straight as the nonlinear coupling term τ^4/κ^2 forces τ to approach zero faster than κ. and the ribbons relative extension z/L asymptotes toward 1 in a similar way as the WLC: $z/L \approx 1 - 1/\sqrt{F}$, except at a slower rate. A useful interpolation formula for the WLC, correct to within 10%, was proposed by Bustamante et al. [16, 97] to join these two regimes at intermediary forces:

$$\frac{Fa}{k_B T} = \frac{1}{4}\left[\frac{1}{(1 - z/L)^2} - 1\right] + \frac{z}{L}. \tag{4.64}$$

We can replot 4.3 by dividing the normalized force f by the normalized temperature Λ, and we see that the different curves collapse into one curve as shown in 4.4. The best fit interpolation formula for the Sadowsky ribbon is given by

$$\frac{Fa}{k_B T} = 0.24\frac{1}{(1 - z/L)^2} + 6.87\frac{z}{L} - 0.29. \tag{4.65}$$

Next, we consider the force extension curve of a ribbon under the additional effect of a torque. In this case, we find that the ribbon tend to stay supercoiled and jumbled up for small applied force. However, beyond some critical force, the ribbon starts to disentangle and extend sharply, reminiscent of a first order phase transition. The force extension behavior at high force reverts to the case of the ribbon under no applied torque. The ribbon in the entangled state has very high linking and writhe number with relatively low twist. Once untangled, the ribbon tend to stretch rapidly and the linking and writhe number falls off drastically, while the twist steadily increases. In the stretched state, the bulk of the contribution of the linking number comes predominantly from the twist. This is a phenomenon that we find in everyday

ribbons whereby the writhe of an initial coiled up ribbon is converted into twist as it is being stretched. The summary of the results is shown in 4.5. We also show some characteristic shapes of the ribbon at different f in and the conformations of the ribbons agree with our intuition, and is a good sensibility check.

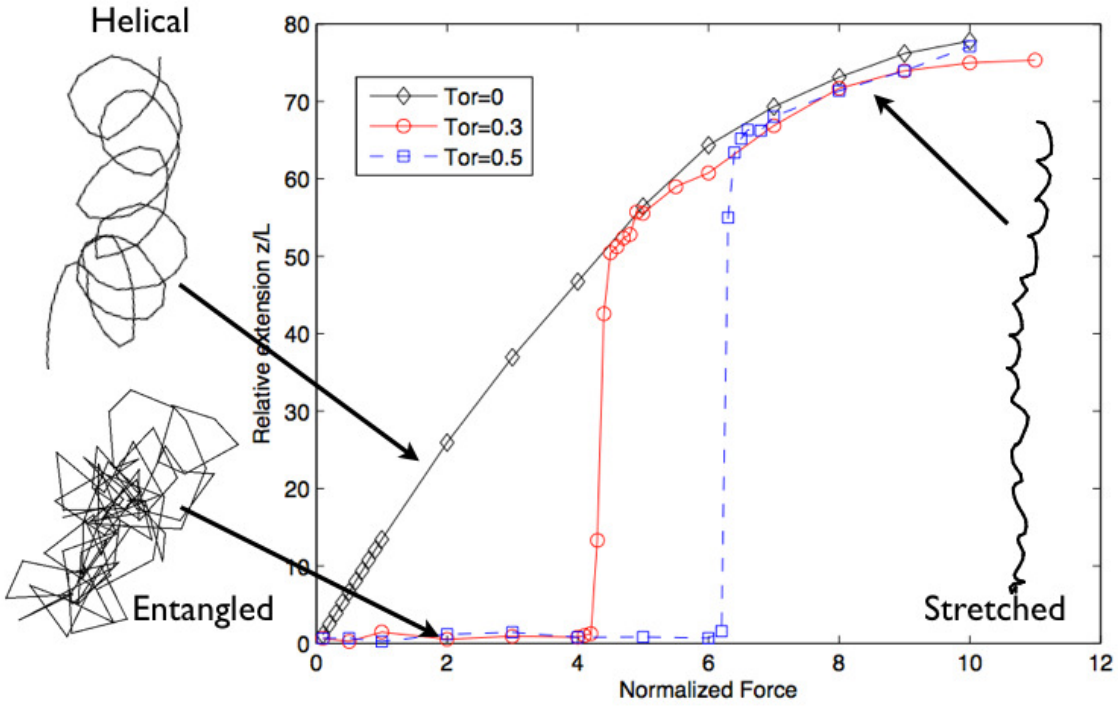

Figure 4.5: Force-Extension curve for a ribbon at $\Lambda = 1$ under different applied torque Γ. At zero torque, the ribbon has an underlying helical structure, which is destroyed in the presence of an applied torque. At small forces, the ribbon under torsion tend to stay as an entangled coil but beyond a critical force, it starts to extend sharply, analogous to a first order transition. At small applied force ($f = 3$), the ribbon is in a highly clustered conformation. As we increase the force, the ribbon becomes more stretched and twisted. At high force ($f = 8$), the ribbon becomes highly twisted. The amount of excess link in the ribbon has depends on the strength of the external torque. The higher the torque, the more "twisted" the ribbon is. Some characteristic ribbon conformations are shown.

Lastly, we consider a ribbon under the effect of a constant force and varying torque. We will impose torsional constraint through a fixed applied torque Γ rather

than directly through a fixed linking number. The result is plotted in 4.6. In our simulations, we ignored the effects of knotting since the segments of the chain were allowed to cross one another during trial moves in the MC run. To check for knot-checking, one would evaluate the Alexander polynomial and reject any trial moves that changes the topology of the chain. Such a test is omitted in this study as it has been found that such an effect is not too significant and topology checking is computationally intensive. [59, 102, 65, 68, 69].

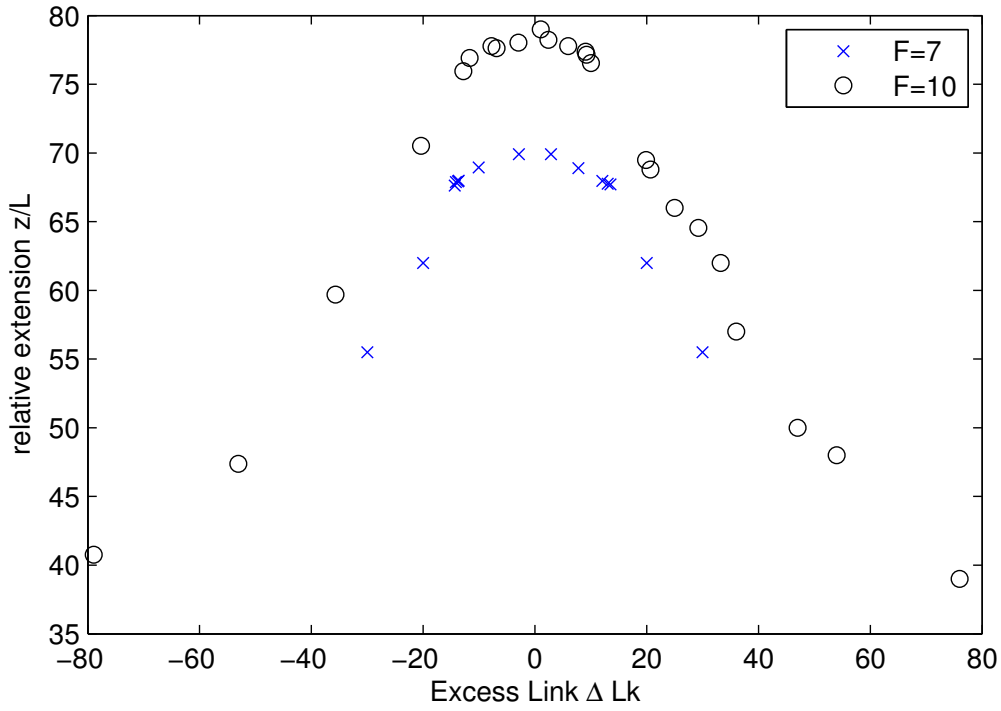

Figure 4.6: Relative extension of ribbon versus excess linking number at different fixed applied force and $\Lambda = 1$.

Physically, we can see that at high enough tension F, the problematic loops and knots will be so rare such that it is negligible since the elastic rod will be very straight. Apart from the restriction of these phantom crossing, it is also unnecessary to consider

the DNA stretching under high applied force since real DNA molecules undergoes structural transformations at high tensions and torques and the WLC/ribbon (no stretching) model breaks down. The graph is generally symmetrical about $\Delta Lk = 0$ since our Sadowsky Hamiltonian 4.4 has no symmetry breaking term unlike the WLC model, where the DNA chirality is introduced explicitly in the twist strain term of coupling strength C. The relative extension z/L increases with force and decreases sharply as excess link ΔLk deviates significantly from zero.

4.7 Conclusion

Our study has shown that at low applied force, the Sadowsky ribbon behaves very much like a spring, that is, it obeys a Hooke relation: $f = k\langle z \rangle$. However, at high applied force, the Sadowsky ribbon prefers to be straight and this stems from the nonlinear coupling term τ^4/κ^2 which forces τ to approach zero faster than κ. In the presence of applied torsion, we find that the ribbon tends to adopt a compact random-coil structure in the low applied force regime, destroying the underlying helical structure. This preference stems from the phenomenon of entropic elasticity: extended chain is entropically unfavourable, as there are fewer possible conformations at longer extensions, with only a single possible conformation (a perfectly straight line) for maximum extension. However, beyond some critical force, the ribbon starts to disentangle and extend sharply, reminiscent of a first order phase transition. Once disentangled, the ribbon tend to stretch rapidly and the linking and writhe number falls off drastically, while the twist steadily increases. In the stretched state, the bulk of the contribution of the linking number comes predominantly from the twist. Fi-

nally, our simulations show that at fixed applied force, an increase in torsion leads to an increment in linking number, resulting in the ribbon becoming more coiled and less extended.

Appendix A

Continuum-Elastic Theory

The elastic energy E_T of a deformed shell may be regarded as the sum of bending and that due to stretching of the middle surface as follows [110, 54]:

$$\begin{aligned} H_T &= H_s + H_b \\ &= \int dA(E_s + E_b) \\ &= \frac{1}{2}\int dA(2\mu\gamma_{ij}^2 + \lambda\gamma_{kk}^2) + \frac{1}{2}\int dA(\kappa(2H - c_0)^2 + 2\kappa_G K), \end{aligned} \tag{A.1}$$

where γ_{ij} is the strain tensor, $\hat{\mu}$ and $\hat{\lambda}$ are the two-dimensional (2D) membrane Lamé coefficients, κ is the bending rigidity, κ_G is the Gaussian rigidity, H and K are the mean and Gaussian curvatures respectively and c_0 is the spontaneous curvature. If R_1 and R_2 are the principal radii of curvature, then $H = (1/R_1 + 1/R_2)/2$ and $K = 1/R_1R_2$.

A.1 Föppl-von Kármán-Donnell equations

Consider an isolated shallow section S_0 (bulge) of the sphere. Cartesian coordinates x and y are chosen for the base plane of the shallow section and z is normal to this plane, the Monge representation. The stress-strain relations and the bending-strain displacements of the shallow shell theory are linear while the membrane strain displacement relations are nonlinear. Let the tangential displacements be given by $u_1 = U$ and $u_2 = V$ and the normal displacement to be W. The components of the membrane strain tensor γ_{ij} are given by [46, 92]

$$\gamma_{xx} = U_{,x} + W/R + \frac{1}{2}W_{,x}^2, \tag{A.2}$$

$$\gamma_{yy} = V_{,y} + W/R + \frac{1}{2}W_{,y}^2, \tag{A.3}$$

$$\gamma_{xy} = \frac{1}{2}(U_{,y} + V_{,x}) + \frac{1}{2}W_{,x}W_{,y}. \tag{A.4}$$

Here and elsewhere in the paper, a comma followed by an additional subscript denotes partial differentiation with respect to the subscript, i.e. $A_{,x} \equiv \partial A/\partial x$. Using tensor notation, we can represent the strain tensor succinctly as

$$\gamma_{ij} = \frac{1}{2}\left(\partial_i u_j + \partial_j u_i + \partial_i W \partial_j W\right) + W\frac{\delta_{ij}}{R}. \tag{A.5}$$

Similarly, the components of the curvature tensor ρ_{ij} are given by

$$\rho_{xx} = \kappa_x = -W_{,xx}, \tag{A.6}$$

$$\rho_{yy} = \kappa_y = -W_{,yy}, \tag{A.7}$$

$$\rho_{xy} = \tau = -W_{,xy}. \tag{A.8}$$

In other words, $\rho_{ij} = -W_{,ij}$. The mean curvature H and the Gauss curvature K are

related to the curvature tensor ρ_{ij} via

$$H = \boldsymbol{\nabla} \cdot \left(\frac{\boldsymbol{\nabla} W}{\sqrt{1 + |\boldsymbol{\nabla} W|^2}} \right) \approx \nabla^2 W = -\mathrm{Tr}\rho_{ij}$$

and

$$K = \frac{\det(\rho_{ij})}{(1 + |\boldsymbol{\nabla} W|^2)^2} \approx \det(\rho_{ij}) = \frac{1}{2}\left((\mathrm{Tr}\rho_{ij})^2 - Tr(\rho_{ij}^2) \right).$$

The area element $dA = \sqrt{g} dx dy$. In the same spirit, we can ignore the factor

$$\sqrt{g} = \sqrt{1 + |\boldsymbol{\nabla} W|^2}$$

in the measure, so $dA \approx dx dy$.

The 2D Young's modulus $Y = Eh$ where E is the Young's modulus and h is the thickness of the shell. When the membrane is made of isotropic material, we can express the two-dimensional Lamé coefficients to the 2D Young's modulus Y and the Poisson ratio ν [110, 82]:

$$\hat{\lambda} = \frac{\nu Y}{1 - \nu^2},$$
$$\hat{\mu} = \frac{Y}{2(1 + \nu)}.$$

Note that the 2D Poisson ratio $\hat{\nu}$,

$$\hat{\nu} = \frac{\hat{\lambda}}{\hat{\lambda} + 2\hat{\nu}} = \nu,$$

thus we will not make the distinction between material Poisson ratio to the membrane Poisson ratio. This way, the membrane stretching term can be rewritten in the more common form:

$$\begin{aligned} E_s &= \frac{Y}{2(1+\nu)} \left(\mathrm{Tr}(\gamma_{ij}^2) + \frac{\nu}{1-\nu} (\mathrm{Tr}\gamma_{ij})^2 \right) \\ &= \frac{Y}{2(1+\nu)} \left((\gamma_{xx}^2 + \gamma_{yy}^2 + 2\gamma_{xy}^2) + \frac{\nu}{1-\nu} (\gamma_{xx} + \gamma_{yy})^2 \right) \\ &= \frac{Y}{2(1-\nu^2)} \left((\gamma_{xx} + \gamma_{yy})^2 - 2(1-\nu)(\gamma_{xx}\gamma_{yy} - \gamma_{xy}^2) \right) \end{aligned} \tag{A.9}$$

The strain tensor C is related to stress tensor σ by the (constitutive) bidimensional Hooke law

$$\gamma_{ij} = \frac{1+\nu}{E}\left(\sigma_{ij} - \frac{\nu}{1+\nu}\sigma_{kk}\delta_{ij}\right), \tag{A.10}$$

or equivalently

$$\sigma_{ij} = \frac{E}{1+\nu}\left(\gamma_{ij} + \frac{\nu}{1-\nu}\gamma_{kk}\delta_{ij}\right). \tag{A.11}$$

Similarly, we can express the bending and Gaussian rigidity in terms of Y and ν:

$$\kappa = \frac{Eh^3}{12(1-\nu^2)},$$

$$\kappa_G = -\frac{Eh^3}{12(1+\nu)}.$$

This allow us to rewrite the bending term as

$$\begin{aligned} E_b &= \frac{Eh^3}{24(1-\nu^2)}\left(H^2 - 2(1-\nu)K\right) \\ &= \kappa\left((\kappa_x+\kappa_y)^2 - 2(1-\nu)(\kappa_x\kappa_y - \tau^2)\right) \end{aligned} \tag{A.12}$$

The slenderness of the shell is characterize by the ratio h/R or equivalently the Föppl-von Kármán-Donnell number γ defined as

$$\gamma = \frac{YR^2}{\kappa}. \tag{A.13}$$

Thin shells tend to form faceted structure while thick shell prefer to remain spherical at its spontaneous mean curvature c_0.

Thus we can see that the elastic energy is a functional of the displacements U, V and W. The Föppl-von Kármán-Donnell (FvKD) shell equations arise as the Euler-Lagrange variations with respect to (*w.r.t.*) U, V and W. The variations with respect

to U and V give

$$\left(\frac{\partial E_s}{\partial \gamma_{xx}}\right)_x + \left(\frac{\partial E_s}{\partial \gamma_{xy}}\right)_y = 0,$$
$$\left(\frac{\partial E_s}{\partial \gamma_{yy}}\right)_y + \left(\frac{\partial E_s}{\partial \gamma_{xy}}\right)_x = 0. \tag{A.14}$$

These two equations imply that we can define a potential F such that

$$\left(\frac{\partial E_s}{\partial \gamma_{xx}}\right) = F_{,yy} = N_{xx}, \tag{A.15}$$
$$\left(\frac{\partial E_s}{\partial \gamma_{yy}}\right) = F_{,xx} = N_{yy}, \tag{A.16}$$
$$-\left(\frac{\partial E_s}{\partial \gamma_{xy}}\right) = F_{,xy} = -N_{xy}. \tag{A.17}$$

The tensor N_{ij} is the tensor of stresses σ_{ij} averaged through the width of the shell, i.e. $N_{ij} = \int_{-h/2}^{h/2} \sigma_{ij} dz$. If the stresses do not vary over the width of the shell, then $h\sigma_{ij} = N_{ij}$. Note that N_{ij} has units of force/length so that F has units of force·length. F is commonly known as the Airy stress function. We can represent N_{ij} succinctly by

$$N_{ij} = h\sigma_{ij} = \epsilon_{ik}\epsilon_{jl}\partial_k\partial_l F, \tag{A.18}$$

where ϵ_{ij} is the alternating tensor. The variation $w.r.t.$ W yield

$$\partial_{xx}\left(\frac{\partial E_b}{\partial \kappa_x}\right) + 2\partial_{xy}\left(\frac{\partial E_b}{\partial \tau}\right) + \partial_{yy}\left(\frac{\partial E_b}{\partial \kappa_y}\right) + \partial_x\left(\frac{\partial E_s}{\partial \gamma_{xx}} W_{,x}\right) +$$
$$\partial_y\left(\frac{\partial E_s}{\partial \gamma_{xy}} W_{,x}\right) + \partial_x\left(\frac{\partial E_s}{\partial \gamma_{xy}} W_{,y}\right) + \partial_y\left(\frac{\partial E_s}{\partial \gamma_{yy}} W_{,y}\right) = 0. \tag{A.19}$$

Using the Airy stress function (A.18), we can simplify (A.19) into

$$\kappa\nabla^4 W + \frac{1}{R}\nabla^2 F - \{F, W\} = 0, \tag{A.20}$$

where

$$\{A, B\} \equiv A_{,xx}B_{,yy} + A_{,yy}B_{,xx} - 2A_{,xy}B_{,xy},$$

∇^4 is the two-dimensional biharmonic operator and ∇^2 is the two-dimensional Laplacian operator. This is the first FvKD equation. We need another equation in order to close our system which have 2 variables, namely, F and W. This comes from compatibility consideration which we require eqn. (A.5) to be equal to eqn. (A.10). Consider the "incompatibility operator" given by

$$\epsilon_{ik}\epsilon_{jl}\partial_k\partial_l,$$

and apply it to (A.5) and (A.10). The tensor identity

$$\epsilon_{ik}\epsilon_{il} = \delta_{kl},$$

will come in useful in subsequent calculations. Contracting eqn. (A.5) with the "incompatibility operator", we get

$$\epsilon_{ik}\epsilon_{jl}\partial_k\partial_l\gamma_{ij} = \frac{1}{Y}\nabla^4 F. \tag{A.21}$$

On the other hand, when we contract eqn. (A.10), we get contributions from 3 terms. The first contribution is

$$\epsilon_{ik}\epsilon_{jl}\partial_k\partial_l\left(\frac{1}{2}(\partial_i u_j + \partial_j u_i)\right) = s(\mathbf{r}), \tag{A.22}$$

where $s(\mathbf{r})$ is the density of disclinations [90]. In the continuum limit, we can ignore this term and set it to zero. The second contribution

$$\epsilon_{ik}\epsilon_{jl}\partial_k\partial_l\left(\frac{1}{2}(\partial_i W\partial_j W)\right) = -\frac{1}{2}\{W, W\} = -\det(\rho) = -K.$$

The last contribution is

$$\epsilon_{ik}\epsilon_{jl}\partial_k\partial_l\left(W\frac{\delta_{ij}}{R}\right) = \frac{1}{R}\nabla^2 W.$$

Putting everything together, we find that

$$\frac{1}{Y}\nabla^4 F = \frac{1}{R}\nabla^2 W - \frac{1}{2}\{W, W\}, \tag{A.23}$$

giving us the second FvKD equation. If we include the effect of a hydrostatic (inward) pressure p, we need to include an additional energy term

$$H_p = p \int dA\, W, \tag{A.24}$$

which on variation, gives the contribution p. In summary, we have shown that the equilibrium equation and the compatibility equation of a spherical shell under hydrostatic pressure are given by the FvKD equations

$$\kappa\nabla^4 W + \frac{1}{R}\nabla^2 F - \{F, W\} = -p, \tag{A.25}$$

and

$$\frac{1}{Y}\nabla^4 F - \frac{1}{R}\nabla^2 W + \frac{1}{2}\{W, W\} = 0. \tag{A.26}$$

In the case $R \to \infty$, we recover the von Kármán plate equations.

We can write the energy as

$$H_T = \int dA \left[\frac{\kappa}{2}(\nabla^2 W)^2 - \frac{1}{2Y}(\nabla^2 F)^2 + F\left(\frac{1}{R}\nabla^2 W - \frac{1}{2}\{W, W\}\right) + pW\right] \tag{A.27}$$

and eqns. (A.25) and (A.26) can be derived as variational equations from

$$\frac{\delta H_T}{\delta W} = 0, \quad \frac{\delta H_T}{\delta F} = 0.$$

A.2 Linear Buckling Analysis

We will use nonlinear shallow shell equations to determine the buckling pressure [46]. This analysis is only valid in the limit where the characteristic buckle wavelengths are small compared to the radius of the shell R. Let us determine the trivial

solution to equations (A.25), (A.26) for arbitrary p. For the trivial solution, the shell remains spherical and is in a constant state of stress. Denoting the trivial solution by superscript 0, we require that

$$W^0 = \text{const.} \quad \text{and} \quad N_x^0 = N_y^0 = -\frac{1}{2}pR. \tag{A.28}$$

Substituting into equations (A.25), (A.26), we find that

$$F^0 = -\frac{1}{4}(x^2 + y^2)pR, \tag{A.29}$$

and

$$W^0 = -(1-\nu)pR^2/(2Eh). \tag{A.30}$$

Let f and w be perturbation to F and W so that

$$F = F^0 + f \quad \text{and} \quad W = W^0 + w. \tag{A.31}$$

Prior to buckling, f and w are zero. The buckling pressure p_b at which bifurcation from the pre-buckling state of stress can be calculated using linear buckling analysis. After substituting, we find that

$$\kappa\nabla^4 w + \frac{1}{R}\nabla^2 f + \frac{1}{2}pR\nabla^2 w = 0, \tag{A.32}$$

and

$$\frac{1}{Eh}\nabla^4 f - \frac{1}{R}\nabla^2 w = 0. \tag{A.33}$$

Consider periodic solutions of the form:

$$w = \cos(k_x x/R)\cos(k_y y/R) \tag{A.34}$$

and

$$f = C\cos(k_x x/R)\cos(k_y y/R). \tag{A.35}$$

After some calculations, it can be shown that

$$p = \frac{2Eh}{R}\left[(k_x^2 + k_y^2)^{-1} + q_0^{-4}(k_x^2 + k_y^2)\right], \tag{A.36}$$

where

$$q_0^4 = 12(1-\nu^2)\left(\frac{R}{h}\right)^2,$$

and

$$C = -EhR(k_x^2 + k_y^2)^{-1}. \tag{A.37}$$

The classical buckling pressure can be found by minimizing p with respect to k_x and k_y. After some algebra, we find that

$$p_b = \frac{4Eh}{Rq_0^2} = \frac{4\sqrt{\kappa Y}}{R^2} = \frac{2E}{\sqrt{3(1-\nu^2)}}\left(\frac{h}{R}\right)^2, \tag{A.38}$$

and that

$$k_x^2 + k_y^2 = q_0^2. \tag{A.39}$$

Another way of estimating the buckling pressure p_b is by balancing the stretching strain energy of the bulge to the bending strain as done in [54]. If the radius of the bulge is r, and the characteristic width of the ridge d, then the characteristic radial displacement ζ of the points on the ridge will be given by $\zeta = dr/R$, where we have assumed $r \ll R$. The stretching strain energy of the rim scales like ζ/R, so that the stretching energy is $E_s \sim h(2\pi rd)(\zeta/R)^2$. Similarly, the curvature in the rim scales like ζ/d^2, and bending energy which is concentrated around the rim can be approximated by $E_b \sim h^3(2\pi rd)(\zeta/d^2)^2$. By differentiating the total energy $E_t = E_b + E_s$ with respect to d, we can determine the width of the strip d that minimizes the energy stored in the rim of the bulge. After some calculation, we find

that $d \sim \sqrt{(hR)}$, which is the geometric mean of the thickness and the radius of the sphere. If we now assume that the deformation is caused by a hydrostatic pressure p, then the work done by the pressure is approximately $W \sim pHr^2$, where H is the depth of the bulge given by $H \sim R(1-\cos(r/R)) \sim r^2/R$. The total elastic energy has a maximum at $H_{max} \sim h^5/(R^2p)^2$. The zero deformation shape of the shell $H = 0$ is a local minimum, so even for finite pressure the spherical shell will not deform. However, for $p > p_b \sim (h/R)^2 \sim \sqrt{(\kappa Y)}/R^2$, the depth of the minimum indentation that will render the spherical shell unstable becomes smaller than the shell thickness h. The above analysis does not change significantly if the spontaneous curvature of the sphere $1/R_0$ is non-zero as shown in [48].

Appendix B

Surface Evolver

B.1 Elastic energy

Let $\mathbf{s}_1 = \mathbf{v}_2 - \mathbf{v}_1$ and $\mathbf{s}_2 = \mathbf{v}_3 - \mathbf{v}_1$ be the unstrained sides of the triangle, and $\mathbf{r}_1 = \mathbf{v}'_2 - \mathbf{v}'_1$ and $\mathbf{r}_2 = \mathbf{v}'_3 - \mathbf{v}'_1$ be the strained sides. Construct column matrices $S = [\mathbf{s}_1\mathbf{s}_2]$ and $R = [\mathbf{r}_1\mathbf{r}_2]$. The deformation gradient matrix D satisfies $DS = R$. The Gram symmetric (2×2) matrix of an unstrained triangle is defined as $Q = S^T S$, and the Gram matrix of a strained triangle is $F = R^T R$. If everything were happening in a plane, then S is a 2×2 matrix with inverse S^{-1} and $D = RS^{-1}$. Therefore $D^T D = (S^{-1})^T R^T R S^{-1}$. Using the cyclic property of the trace of a matrix, namely, $Tr(ABC) = Tr(CAB) = Tr(BCA)$, we find that

$$\begin{aligned} Tr(D^T D) &= Tr((S^{-1})^T R^T R S^{-1}) = Tr(R^T R S^{-1}(S^{-1})^T) \\ &= Tr(R^T R (S^T S)^{-1}) = Tr(FQ^{-1}). \end{aligned} \tag{B.1}$$

This last expression $Tr(FQ^{-1})$ makes sense when mapping from 2D to 3D, since the inverse of S itself never appears and $S^T S$ is a well-defined square matrix. The Cauchy-

Green strain matrix is $C = (D^T D - I)/2$. Let $C_1 = (FQ^{-1} - 1)$. Since the trance of the matrix is a linear map, namely, $Tr(cA) = cTr(A)$ and $Tr(A + B) = Tr(A) + Tr(B)$, we can see immediately that $Tr(C_1) = Tr(C)$ and $Tr(C_1^2) = Tr(C^2)$. Thus for the calculation of elastic strain energy density given by

$$\frac{Y}{2(1+\nu)}\left(Tr(C^2) + \frac{\nu}{(1-\nu)}(TrC)^2\right), \tag{B.2}$$

where only the trace of the strain matrix matters, one can use C_1 as the Cauchy-Green strain matrix in place of the usual C since either definition will give the same answer.

B.2 Triangulation

In Surface Evolver, any non-triangular face will be automatically triangulated by putting a vertex at its center and putting in edges to each of the original vertices. Faces do not have to be planar. Surface Evolver has a built-in function that allow any user defined surface to be further refined (triangulated) whereby each edge is divided in two, and each triangle is divided into four new ones as shown in Figure B.1.

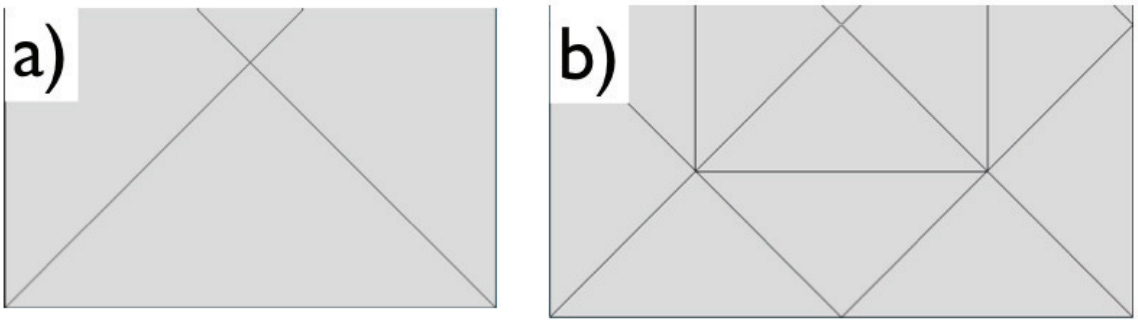

Figure B.1: a) Part of a triangulation. (b) The original triangle is sub-divided into four smaller ones after refinement.

B.3 Energy of thin Shell

The spheres created from different polyhedrons have very different energies since the total energy U_T depends sensitively on the structure of the mesh, which is determined by the number of defects and their relative orientations. Most triangles in a spherical lattice are not equilateral (e.g. when we triangulate a square, we get four congruent right angle triangles instead of four equilateral triangles) and we will define the average length of the edges, $\bar{a}$ to be the lattice spacing a. As we refine the mesh, we get smaller lattice spacing a. We find that as the ratio $R/a \gtrsim 10$ (continuum limit), the total energy of the sphere asymptotes, indicating that the minimal energy surface that we create under surface tension from the original polyhedron starts to approaches that of the perfect sphere. When $R/a \lesssim 1$, there are too few lattice sites on the sphere and hence the triangulation is not smooth. The result for the platonic-spheres are shown in Fig. B.2.

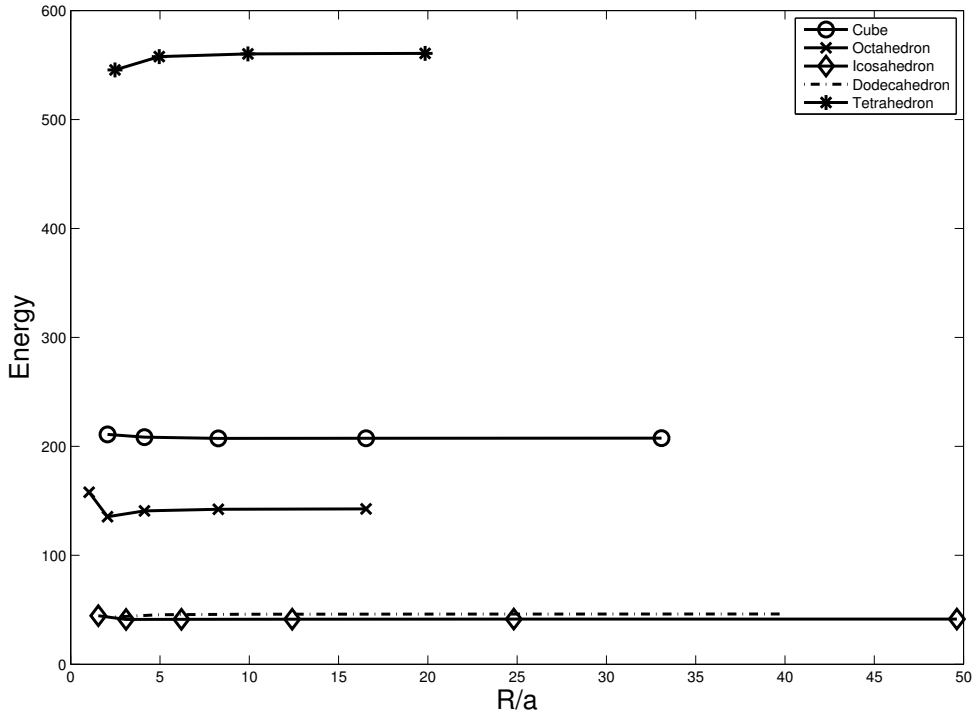

Figure B.2: Plot of Energy vs R/a for the platonic solids for h/R = 0.15.

Appendix C

Mathematical description of Platonic solids

C.1 Onaka's formulation

In this Appendix, I will discuss briefly the analytical equations that describe platonic solids. Although the platonic solids has been known to mathematician since antiquity, surprisingly, simple equations describing their shapes have not been derived in a unified form until recently [77]. Let

$$g(a,b,c) = a(\sin\theta\cos\psi) + b(sin\theta\cos\psi) + c(\cos\theta). \tag{C.1}$$

Then the platonic solids can be described succinctly by the following equations in spherical coordinates (θ, ϕ). For the cube, we have

$$r_{cube}(\theta,\phi) = \frac{1}{[G_0(1,0,0)]^{1/p}}\,, \tag{C.2}$$

where

$$G_0(1,0,0) = |g(1,0,0)|^p + |g(0,1,0)|^p + |g(0,0,1)|^p. \tag{C.3}$$

For the octahedron, we have

$$r_{octa}(\theta,\phi) = \frac{1}{[G_1(\gamma,\gamma,\gamma)]^{1/p}}\,, \tag{C.4}$$

where

$$G_1(\gamma,\gamma,\gamma) = |g(\gamma,\gamma,\gamma)|^p + |g(-\gamma,\gamma,\gamma)|^p + |g(\gamma,-\gamma,\gamma)|^p + |g(\gamma,\gamma,-\gamma)|^p \tag{C.5}$$

and $\gamma = 1/\sqrt{3}$. The dodecahedron is described by

$$r_{dodec}(\theta,\phi) = \frac{1}{[G_2(\delta,\epsilon,0)]^{1/p}}\,, \tag{C.6}$$

where

$$\begin{aligned} G_2(\delta,\epsilon,0) \quad &= |g(\delta,\epsilon,0)|^p + |g(\delta,-\epsilon,0)|^p + |g(0,\delta,\epsilon)|^p \\ &+|g(0,\delta,-\epsilon)|^p + |g(\epsilon,0,\delta)|^p + |g(\epsilon,0,-\delta)|^p \end{aligned}$$

and $\delta = \sqrt{((5-\sqrt{5})/10)}$, $\epsilon = \sqrt{((5+\sqrt{5})/10)}$. The icosahedron is described by

$$r_{ico}(\theta,\phi) = \frac{1}{[G_1(\gamma,\gamma,\gamma) + G_2(\zeta,\eta,0)]^{1/p}}\,, \tag{C.7}$$

where $\zeta = \sqrt{((3-\sqrt{5})/6)}$, $\eta = \sqrt{((3+\sqrt{5})/6)}$. The equation describing a tetrahedron is slightly more complicated since it does not have parallel faces. Let us define a new function $h(a,b,c)$ given by

$$h(a,b,c) = \{|g(a,b,c)| - g(a,b,c)\}/2. \tag{C.8}$$

The tetrahedron can then be described by

$$r_{tetra}(\theta,\phi) = \frac{1}{[H(\gamma,\gamma,\gamma) + (1/p)^{p-2}H(-\gamma,-\gamma,-\gamma)]^{1/p}}\,, \tag{C.9}$$

where

$$H(\gamma,\gamma,\gamma) = \{h(\gamma,\gamma,\gamma)\}^p + \{h(\gamma,-\gamma,-\gamma)\}^p + \{h(-\gamma,\gamma,-\gamma)\}^p + \{h(-\gamma,-\gamma,\gamma)\}^p. \quad \text{(C.10)}$$

This set of five equations given by (C.2) to (C.9) changes from a sphere when $p = 2$ to the respective regular polyhedron when $p \to \infty$.

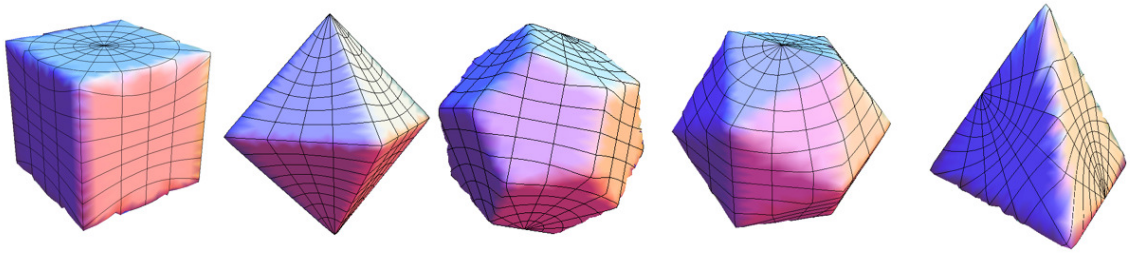

Figure C.1: The Platonic solids plotted using Onaka's formulas using $p = 100$.

Appendix D

Information on Bacterial Spores

D.1 Surface topography and height measurements of bacterial spores

We have used an atomic force microscope to observe changes in surface topography of wild type and mutant spores at low and high relative humidity. Supplementary Figure D.1a and D.1b shows height profiles across a B. Anthracis (Sterne strain) spore and a cotE-gerE mutant of B. Subtilis.

D.2 Identification of coat proteins not required for significant coat stiffness

We do not know which coat protein(s) are required for the high elastic modulus of the coat. To at least partially clarify this question, we took advantage of previous

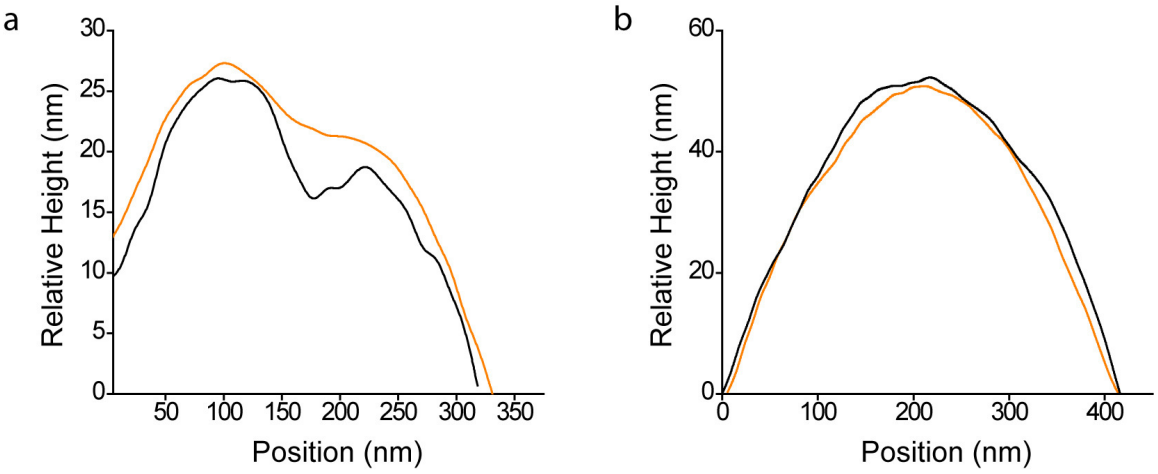

Figure D.1: Height profiles at low (35%, black) and high (95%, orange) relative humidity on wild type B. Anthracis (Sterne strain) (a) and cotE-gerE mutant of B. Subtilis (b). Horizontal and vertical axes are arbitrarily referenced. The average heights of the spores increase at high humidity. To compare local curvatures, profiles obtained at high relative humidity are vertically offset. The profile on B. Anthracis at 95% relative humidity shows that the coat does not unfold completely and maintains wrinkles.

results showing that the B. subtilis cotE mutant spore coat is unfolded, lacks most if not all outer coat proteins and has an only partially intact inner coat [115, 56, 4, 30, 66]. The unfolded state of the cotE mutant coat could be due to a significant decrease in coat stiffness or its adhesion to the cortex. Therefore, analysis of the cotE mutant spore coat elastic modulus might allow us to address the roles of a subset of coat proteins in spore mechanical properties. We found the elastic modulus of the cotE mutant coat to be $\sim$ 6GPa, which is comparable to that of the wild type coat and inconsistent with a significant reduction in stiffness due to the mutation. Therefore, most or all the outer coat proteins are dispensable for a significantly stiff coat. Additionally, we infer that in cotE mutant spores, defects in the inner coat prevent it from folding and/or properly adhering to the cortex.

a

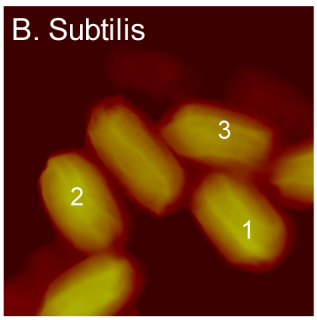

	Low (nm)	High (nm)	Difference (%)
1	725.2	749.7	3.4
2	720	759.1	5.4
3	649.3	670.1	3.2
average	**698.2**	**726.3**	**4.0**

b

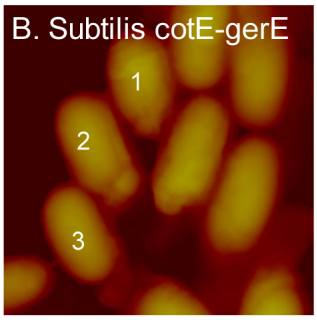

	Low (nm)	High (nm)	Difference (%)
1	707	733	3.7
2	683.5	709.6	3.8
3	667.8	693.9	3.9
average	**686.1**	**712.2**	**3.8**

c

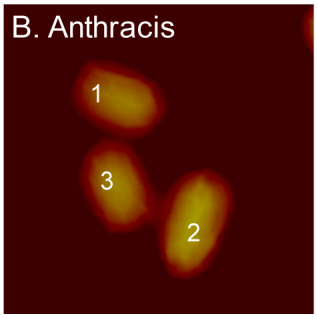

	Low (nm)	High (nm)	Difference (%)
1	786.9	821.4	4.4
2	843.5	915.1	8.5
3	820.3	846.4	3.2
average	**816.9**	**861.0**	**5.4**

Figure D.2: Height measurements on wild type and mutant B. Subtilis, and Sterne strain of B. Anthracis at low (35%) and high humidity (95%). The mutant B. Subtilis spore lacks most of its coat, yet its expansion is comparable to wild type spores.

Appendix E

Mathematical background on Bifurcation

The material presented in this section is taken from [49, 41]

E.1 Implicit Function Theorem

Theorem 1. Suppose X, Y, Z are Banach Spaces and $f(x, \epsilon)$ is a C^1 mapping of an open set U of $X \times Y$ into Z. Suppose there is an $x_0 \in X$ satisfying $f(x_0, 0) = 0$ and the partial derivative $f_x(x_0, 0)$ is an invertible linear map of X onto Z. Then there are open sets $W \subset Y$, and $V \subset U$ with $0 \in W$, and $(x_0, 0) \in V$, and a C^1 mapping g of W into X, such that $x = g(\epsilon)$ for ϵ in W satisfies $f(x, \epsilon) = f(g(\epsilon), \epsilon) = 0$ for $(x, \epsilon) \in V$. In other words, there is a solution of the implicit equation $f(x, \epsilon) = 0$ given by $x = g(\epsilon)$. This solution is unique in some open subset of W.

The implicit function theorem is useful because it tells us that if we know how

to solve a reduced problem, and the linearized operator of the reduced problem is invertible, then the more difficult problem has a solution locally.

E.2 Fredholm Alternative

The Fredholm Alternative Theorem is one of the most important theorem in applied mathematics. It is easier to understand this theorem in finite dimensional vector spaces. Suppose we wish to solve the matrix problem $Ax = b$ where A is an $n \times m$ matrix (not necessarily square). We want to know if there is a solution, and if so, how many solutions are possible.

Theorem 2 (Fredholm Alternative Theorem)**.** The equation $Ax = b$ has a solution if and only if $\langle b, v\rangle = 0$ for every vector v satisfying $A^*v = 0$, where $A^* = A^\dagger$ is the adjoint (or Hermitian) matrix.

A useful follow-up theorem is

Theorem 3. A solution of $Ax = b$ (if it exists) is unique if and only if $x = 0$ is the only solution of $Ax = 0$.

In Hilbert space H, the Fredholm Alternative Theorem takes on the following form.

Theorem 4 (Fredholm Alternative Theorem)**.** If L is a bounded linear differential operator in the H with boundary operator B, the solution of $Lu = f$ and $Bu = g$ exists if and only if $\langle f, v\rangle - J(u, v) = 0$ for every v satisfying $L^*v = 0$ and $B^*v = 0$.

Here $J(u, v)$ represent boundary contributions. If L is in the Sturm-Liouville form, then the boundary contribution is given by

$$J(u, v) = p(x)\left(\frac{du}{dx}v - \frac{dv}{dx}u\right)\Bigg|_a^b.$$

It follows that $Lu = f$, $Bu = g$ can be solved for any f, g if and only if $L^*v = 0$, $B^*v = g$ implies $v = 0$.

E.3 Liapunov-Schmidt reduction method

To get a picture how bifurcation occurs in a more general setting, consider the nonlinear eigenvalue problem

$$Lu + \lambda u + f(u) = 0 \tag{E.1}$$

subjected to homogenous separated boundary conditions. It is apparent that small solutions of the nonlinear eigenvalue problem exist. However, the implicit function theorem cannot be invoked for the problem as formulated. The Liapunov-Schmidt reduction method provide a way to reformulate nonlinear problem to overcome this difficulty. Suppose we let $\lambda = \lambda_0 + \mu$ and $u = \epsilon\phi + \epsilon v$, where $\langle v, \phi\rangle = 0$. In terms of these new variables, the equation (E.1) becomes

$$Lv + \lambda_0 v = -\mu\epsilon(\phi + v) - f(\epsilon\phi + \epsilon v).$$

This equation is solvable if and only if its right hand side is orthogonal to ϕ, so we project its right hand side onto the range of the operator $L + \lambda_0$ by writing

$$\begin{aligned} Lv + \lambda_0 v &= -\mu\epsilon(\phi + v) - f(\epsilon(\phi + v)) + \langle \mu\epsilon(\phi + v) + f(\epsilon(\phi + v)), \phi\rangle\phi \\ &= -\mu\epsilon v - f(\epsilon(\phi + v)) + \langle f(\epsilon(\phi + v)), \phi\rangle\phi. \end{aligned} \tag{E.2}$$

However, for this to be the same problem, we must also require

$$\langle \mu\epsilon(\phi + v) + f(\epsilon(\phi + v)), \phi \rangle = \mu\epsilon + \langle f(\epsilon(\phi + v)), \phi \rangle = 0. \tag{E.3}$$

We collect (E.1) and (E.3) into the system for v and μ

$$\begin{pmatrix} Lv + \lambda_0 v \\ \mu \\ \langle v, \phi \rangle \end{pmatrix} = \begin{pmatrix} -\mu\epsilon v - f(\epsilon(\phi + v)) + \langle f(\epsilon(\phi + v)), \phi \rangle \phi \\ \frac{1}{\epsilon}\langle f(\epsilon(\phi + v)), \phi \rangle \\ 0 \end{pmatrix}. \tag{E.4}$$

The right hand side of (E.4) is fully nonlinear, i.e., it has no linear terms when $\epsilon = 0$, and a solution of this problem is $v = 0$, $\mu = 0$ when $\epsilon = 0$. Furthermore, the linear operator is invertible, so that the implicit function theorem can be invoked, namely, there exist a unique solution $v = v(\epsilon)$, $\mu = \mu(\epsilon)$ for all ϵ sufficiently small. The perturbation calculation given above is a way to explicitly determine this solution.

We will present a slightly more formal treatment now. For a more thorough treatment, please refer to [41], p290. Let $\mathbb{X}$ and $\mathbb{Y}$ be Banach spaces. A bounded linear operator $L : \mathbb{X} \to \mathbb{Y}$ is called Fredholm if 1) the Kernel of L is finite-dimensional space of $\mathbb{X}$ and 2) Range L os a closed subspace of $\mathbb{Y}$ of finite codimension. The index of a Fredholm operator is

$$i(L) = dim\, ker\, L - codim\, range\, L.$$

For example, if W is a linear subspace of a finite-dimensional vector space V, then the codimension of W in V is the difference between the dimensions:

$$codim W = dim(V) - dim(W).$$

If $L : \mathbb{X} \to \mathbb{Y}$ is Fredholm, then there exist closed subspaces M and N of $\mathbb{X}$ and $\mathbb{Y}$ such that

$$\mathbb{X} = Ker\, L \oplus M, \tag{E.5}$$

$$\mathbb{Y} = N \oplus range\, L. \tag{E.6}$$

Note that $M = (Ker\, L)^{\perp}$ and $N = (range\, L)^{\perp}$. By the Fredholm alternative, we have

$$(range\, L)^{\perp} = ker\, L^{*}. \tag{E.7}$$

Let

$$\Phi : \mathbb{X} \times \mathbb{R}^{k+1} \to \mathbb{Y}, \quad \Phi(0,0) = 0 \tag{E.8}$$

be a smooth mapping between Banach space and $\mathbb{R}^{k+1}$ is the parameter space, which also include the bifurcation parameter. We want to use Liapunov-Schmidt reduction to solve the equation

$$\Phi(u, \lambda) = 0 \tag{E.9}$$

Let L be the differential of Φ at the origin,

$$Lu = \lim_{h \to 0} \frac{\Phi(hu) - \Phi(0,0)}{h},$$

and we will assume L is Fredholm of index zero. The Liapunov-Schmidt reduction method involves five steps:

1. Decompose $\mathbb{X}$ and $\mathbb{Y}$ according to (E.5) and (E.6).

2. Split (E.6) into a pair of equivalent equations:

$$E\Phi(u, \lambda) = 0,$$

$$(I - E)\Phi(u, \lambda) = 0. \tag{E.10}$$

where $E : \mathbb{Y} \to range\, L$ is the projection associated to the splitting defined in (E.6).

3. Use (E.5) to write $u = v + w$, where $v \in ker\, L$ and $w \in M$. Apply the implicit function theorem to solve (2) for w as a function of v and λ. This leads to a function

$$W : ker\, L \times \mathbb{R}^{k+1} \to M$$

such that

$$E\Phi(u + W(v, \lambda), \lambda) \equiv 0.$$

4. Define $\phi : ker\, L \times \mathbb{R}^{k+1} \to N$ by

$$\phi(v, \lambda) = (I - E)\Phi(u + W(v, \lambda), \lambda).$$

5. Choose a basis $v_1, \ldots, v_n$ for $ker\, L$ and a basis $v_1^*, \ldots, v_n^*$ for $(rangeL)^\perp$. Define $g : \mathbb{R}^n \times \mathbb{R}^{k+1} \to \mathbb{R}^n$ by

$$g_i(x, \lambda) = \langle v_i^*, \phi(x_1 v_1 + \cdots x_n v_n, \lambda)\rangle. \tag{E.11}$$

Since L is Fredholm with index zero, we have

$$dim\, ker\, L = dim(range\, L)^\perp$$

and both dimensions are finite. Thus the bases for $ker\, L$ and $(range\, L)^\perp$ contain the same number of vectors.

The important result from Liapunov-Schmidt reduction is that if the linearization of $\Phi(u, \lambda) = 0$ is a Fredholm operator of index zero, then the solutions of (E.9) are

(locally) in one-to-one correspondence with the solutions of the finite system defined by (E.11).

Appendix F

Review of DNA models

F.1 Random Walk Model

Consider a N-step random walk in 3D [34, 5]. The probability of the walker at a distance $\boldsymbol{r}$ after N steps is given by

$$P_N(\boldsymbol{r}) = \frac{g_N(\boldsymbol{r})}{g_N^{tot}} = \frac{1}{(2\pi N a^2/3)^{3/2}} \exp\left(-\frac{3r^2}{2Na^2}\right), \tag{F.1}$$

where $g_N(\boldsymbol{r})$ is the tool number of walks of N steps terminating at the position $\boldsymbol{r}$, a is the size of each step and g_N^{tot} is the total number of walks of length N. The partition function of a random walker is

$$\begin{aligned} Z &= \sum_{states} \exp(-E_n/k_BT) = \sum_E g(E)\exp(-E/k_BT) \\ &= \sum_E \exp(\ln g(E) - E/k_BT) = \sum_E \exp(-G(E)/k_BT), \end{aligned} \tag{F.2}$$

where $g(E)$ is the degeneracy of states with energy E and $G = E - TS$ is the free energy, $S = k_B \ln g(E)$ is the entropy. For a floppy polymer, $E \equiv 0$ and we find that

$$G = -TS = const. + \frac{1}{2}\frac{3k_BT}{Na^2}r^2 = const. + \frac{1}{2}kr^2. \tag{F.3}$$

When we apply a force $\boldsymbol{F}$ to the random walk model, we need to include an additional energy term given by

$$E = -\boldsymbol{F} \cdot \boldsymbol{r}. \tag{F.4}$$

In this case, we find that the partition function becomes

$$\begin{aligned} Z_N &= \sum_E g(E) \exp(-E/k_B T) \\ &= const. \int d^3 r \exp(-kr^2/2k_B T) \exp(\boldsymbol{F} \cdot \boldsymbol{r}/k_B T) \\ &= const. \exp(F^2/2k(k_B T)). \end{aligned} \tag{F.5}$$

In this case we find that the

$$\langle \boldsymbol{r} \rangle = k_B T \frac{\partial}{\partial \boldsymbol{F}} \ln Z = \frac{\boldsymbol{F}}{k} = \frac{1}{3} \frac{La}{k_B T} \boldsymbol{F}. \tag{F.6}$$

F.2 Freely Joint Chain

A simple extension to the random walker model is the freely joint chain (FJC) [73]. This model defines the state of the polymer by its tangent $\boldsymbol{t}_i, i = 0, ..., N-1$, namely

$$\boldsymbol{r} = a \sum_i \boldsymbol{t}_i. \tag{F.7}$$

The partition function of a freely joint chain is

$$\begin{aligned} Z(\boldsymbol{F}) &= \int \frac{d\Omega_0}{4\pi} \cdots \int \frac{d\Omega_{N-1}}{4\pi} \exp\left(Fa \sum_i \cos\theta_i / k_B T \right) \\ &= \prod_{i=0}^{N-1} \left[\frac{1}{4\pi} \int_0^{2\pi} d\phi_i \int_0^{\pi} d\theta_i \sin\theta_i \exp(Fa \cos\theta_i / k_B T) \right] \\ &= \left(\frac{k_B T}{Fa} \sinh(Fa/k_B T) \right)^N. \end{aligned} \tag{F.8}$$

We can calculate the extension z which is given by

$$\begin{aligned} z &= a\sum_i \cos\theta_i = k_BT\frac{\partial}{\partial F}\ln Z \\ &= Na\left[\coth(Fa/k_BT) - k_BT/Fa\right]. \end{aligned} \tag{F.9}$$

When F is small, we find that ($\coth x - 1/x \approx x/3$ for small x)

$$\frac{z}{L} \approx \frac{1}{3}\frac{Fa}{k_BT}. \tag{F.10}$$

When F is large, we find that ($\coth x - 1/x \approx 1 - 1/x$ for large x)

$$\frac{z}{L} \approx 1 - \frac{k_BT}{Fa}. \tag{F.11}$$

The end to end distance is given by

$$\langle r^2\rangle = a^2\langle(\sum_j \boldsymbol{t}_j)^2\rangle = a^2\sum_{i,j}\langle \boldsymbol{t}_i\cdot\boldsymbol{t}_j\rangle. \tag{F.12}$$

For a floppy polymer, the tangents are uncorrelated and hence

$$\langle \boldsymbol{t}_i\cdot\boldsymbol{t}_j\rangle = \delta_{ij}, \tag{F.13}$$

and we find that

$$\langle r^2\rangle = Na^2 = La. \tag{F.14}$$

F.3 Worm-Like Chain Model

In the Kratky-Porod or Worm-Like Chain Model [73, 63], the tangents are coupled, namely

$$E[\boldsymbol{t}(s)] = \frac{1}{2}A\int_0^L \left(\frac{d\boldsymbol{t}(s)}{ds}\right)^2 ds = \frac{1}{2}A\int_0^L \kappa^2 ds, \tag{F.15}$$

where $\kappa(s)$ is the curvature of the chain at arclength s. We can discretize the curvature as

$$\kappa_i^2 = \frac{|\boldsymbol{t}_i - \boldsymbol{t}_{i-1}|^2}{a^2} = const. - 2a^{-2}\,\boldsymbol{t}_i \cdot \boldsymbol{t}_{i-1} \tag{F.16}$$

and so

$$E[\{\boldsymbol{t}_i\}] = -(Aa^{-2}a)\sum_i \boldsymbol{t}_i \cdot \boldsymbol{t}_{i-1} = -A'\sum_{i=1}^{N-1}\cos\theta_i, \tag{F.17}$$

where $A' = Aa^{-1}$ and we have dropped an unimportant constant from the energy. The exact zero partition function for the WLC is

$$\begin{aligned} Z_N &= \int \frac{d\Omega_0}{4\pi}\prod_{i=1}^{N-1}\int \frac{d\Omega_i}{4\pi}\exp(-E_i/k_BT) \\ &= \prod_{i=1}^{N-1}\int_0^{2\pi}\frac{d\phi_i}{4\pi}\int_0^{\pi} d\theta_i \sin\theta_i \exp(-A'\cos\theta_i/k_BT) \\ &= \left[\frac{\sinh\alpha}{\alpha}\right]^{N-1}, \end{aligned} \tag{F.18}$$

where $\alpha = A'/k_BT$. The tangent-tangent correlation function is

$$\begin{aligned} C(p) &= \langle \boldsymbol{t}_0 \cdot \boldsymbol{t}_p\rangle = 3\langle t_0^z t_p^z\rangle \\ &= 3\left(\int D[\Omega_i]\, t_0^z t_p^z \exp(-E/k_BT)\right)/Z_N \\ &= 3\left(\prod_{i=0}^{N-1}\int \frac{d\Omega_i}{4\pi}\,\cos\psi_0\cos\psi_p\exp(-\alpha\cos\theta_i)\right)/Z_N \\ &= 3\int\frac{d\Omega_0}{4\pi}\cos\psi_0 \times \int\frac{d\Omega_1}{4\pi}\cdots\int\frac{d\Omega_{p-1}}{4\pi}\exp(-\alpha\sum_{i=1}^{p-1}\cos\theta_i) \\ &\qquad \times\int\frac{d\Omega_p}{4\pi}\cos\psi_p\exp(-\alpha\cos\theta_p)/\left[\frac{\sinh\alpha}{\alpha}\right]^p, \end{aligned} \tag{F.19}$$

where ψ is the angle relative to the fixed lab frame. This differs from the angles in the measure $D[\Omega_i] = \prod_i d\Omega_i/4\pi = \prod_i d\cos\theta_i d\phi/4\pi$ which are the polar angles relative

to the polar axis defined by $\boldsymbol{t}_{i-1}$. In the $\boldsymbol{t}_{p-1}$ coordinate systems, we have

$$\boldsymbol{t}_p = \begin{pmatrix} \sin\theta_p \cos\phi_p \\ \sin\theta_p \sin\phi_p \\ \cos\theta_p \end{pmatrix}, \quad \hat{\boldsymbol{z}} = \begin{pmatrix} \sin\psi_{p-1} \\ 0 \\ \cos\psi_{p-1} \end{pmatrix}. \tag{F.20}$$

We have chosen the $\Phi_{p-1} = 0$ since we are only interested in the plane defined by $\boldsymbol{t}_{p-1}$ and $\hat{\boldsymbol{z}}$. So we find that

$$\cos\psi_p = \hat{\boldsymbol{z}} \cdot \boldsymbol{t}_p = \cos\theta_p \cos\psi_{p-1} + \sin\theta_p \cos\phi_p \sin\psi_{p-1}. \tag{F.21}$$

Inserting this into (F.19), we find that

$$C(p) = C(p-1)\left(\coth\alpha - 1/\alpha\right). \tag{F.22}$$

The term involving $\sin\psi_{p-1}$ vanishes since

$$\int_0^{2\pi} d\phi_p \cos\phi_p = 0.$$

By iteration, we find that

$$C(p) = \left(\coth\alpha - 1/\alpha\right)^p C(0). \tag{F.23}$$

Since $C(0) = \langle \boldsymbol{t}_0 \cdot \boldsymbol{t}_0 \rangle = 1$, we find that

$$C(p) = \exp(-ap/\xi) \tag{F.24}$$

where we have defined the persistence length to be

$$\xi(T) = \frac{-a}{\ln\left(\coth\alpha - 1/\alpha\right)}. \tag{F.25}$$

Therefore we see that the tangent-tangent correlation $C(p)$ exhibits exponential decay with persistence length ξ. The persistence length is finite $\forall T > 0$ so we see that there

is no phase transition in the WLC model. The persistence length is very useful in describing elastic properties of semiflexible polymers and measures the length along the chain over which the tangent vectors of the chain become de-correlated. When $\alpha \gg 1$ (small temperature k_BT or large A limit), we find that ($\ln(1+x) \approx x - x^2/2 + \cdots$ for small x):

$$\xi \approx \frac{-a}{\ln(1-1/\alpha)} = a\alpha = \frac{A}{k_BT}. \tag{F.26}$$

The mean square end to end distance of a WLC can be calculated as follows:

$$\begin{aligned} \langle r^2 \rangle &= a^2 \frac{1}{a^2} \int_0^{Na} ds \int_0^{Na} ds' \exp(-|s-s'|/\xi) \\ &\approx Na \int_{-\infty}^{\infty} d\Delta s \, \exp(-|\Delta s|/\xi) \\ &= 2Na\xi = 2L\xi. \end{aligned} \tag{F.27}$$

Comparing with eqn. (F.14) of FJC model, we see that for the WLC, the Kuhn length [34] is

$$a(T) = 2\xi(T) = \frac{2A}{k_BT}. \tag{F.28}$$

Consider the force extension curve at small forces with the simplifying assumption that the force is along the z-direction. We find that

$$\begin{aligned} z &= \langle \boldsymbol{r} \rangle_F \cdot \hat{\boldsymbol{z}} = a\hat{\boldsymbol{z}} \cdot \sum_i \langle \boldsymbol{t}_i \rangle_F \\ &= a \langle \sum_i t_i^z (1 + \frac{Fa}{k_BT} \sum_j t_j^z + \cdots) \rangle_{F=0} \\ &\approx \frac{Fa^2}{k_BT} \sum_{i,j} \langle t_i^z t_j^z \rangle_{F=0} \\ &= \frac{1}{3} \frac{F}{k_BT} \langle r^2 \rangle + O(F^2). \end{aligned} \tag{F.29}$$

The notation $\langle \cdot \rangle_F$ denotes the weighted average with respect to partition function Z with the inclusion of a force term in the free energy. We have made use of the fact

that for small F,

$$\exp(Fa\sum_i t_i^z/k_BT) \approx 1 + \frac{Fa}{k_BT}\sum_j t_j^z + \cdots \tag{F.30}$$

and when the applied force is zero,

$$\langle t_i^z t_j^z\rangle_{F=0} = \frac{1}{3}\langle \boldsymbol{t}_i \cdot \boldsymbol{t}_j\rangle_{F=0}, \tag{F.31}$$

due to rotational symmetry. Thus we find that for a WLC,

$$z = \frac{1}{3}\frac{2L\xi(T)}{k_BT}F = \frac{1}{3}\frac{La}{k_BT}F. \tag{F.32}$$

Next, let us consider the force extension curves at large $\boldsymbol{F}$ ($F\xi/k_BT \gg 1$). In the continuum model, the WLC is given by

$$E = \frac{1}{2}A\int_0^L \left(\frac{d\boldsymbol{t}}{ds}\right)^2 ds - \boldsymbol{F}\cdot\int_0^L \boldsymbol{t}(s)ds. \tag{F.33}$$

In this limit, we can approximate the tangent vector by

$$\boldsymbol{t}(s) = \begin{pmatrix} t_x(s) \\ t_y(s) \\ \sqrt{1-t_x^2-t_y^2} \end{pmatrix} \approx \begin{pmatrix} t_x(s) \\ t_y(s) \\ 1 \end{pmatrix}. \tag{F.34}$$

In which case the energy can be written as

$$E \approx \frac{1}{2}\int_0^L \left\{A[(dt_x/ds)^2 + (dt_y/ds)^2] + F(t_x^2+t_y^2)\right\} ds - FL. \tag{F.35}$$

Let us make the following Fourier transformation:

$$t_x(s) = \frac{1}{L}\sum_q \exp(iqs)\hat{t}_x(q). \tag{F.36}$$

Assume periodic boundary conditions so $t_x(s+L) = t_x(s)$ so we get

$$q = \frac{2\pi}{L}m$$

Since $t_x(s)$ is real, we find that

$$\hat{t}_x^*(q) = \hat{t}_x(-q). \tag{F.37}$$

Similar expressions hold for $t_y(s)$. Using the identity

$$\frac{1}{L}\int_0^L \exp(i(q+k)s)ds = \delta_{q+k,0},$$

the energy can be expressed in Fourier modes:

$$E \approx \frac{1}{2L}\sum_q (Aq^2+F)(|\hat{t}_x(q)|^2 + |\hat{t}_y(q)|^2). \tag{F.38}$$

The partition function Z is

$$Z = \int D[\hat{\boldsymbol{t}}(q)] \exp\left(-\frac{1}{2Lk_BT}\sum_q (Aq^2+F)(|\hat{t}_x(q)|^2 + |\hat{t}_y(q)|^2)\right). \tag{F.39}$$

The path integral is defined as

$$\int D[\hat{\boldsymbol{t}}(q)] = \prod_{\mu=x,y}\prod_{q\geq 0}\int_{-\infty}^{\infty} d(Re\hat{t}_\mu(q)) \int_{-\infty}^{\infty} d(Im\hat{t}_\mu(q)),$$

where the wavenumber q is over the positive real space due to eqn. (F.37). A straightforward calculation reveals that

$$\langle \hat{t}_\mu(q)\hat{t}_\nu(k)\rangle = L\frac{k_BT}{Aq^2+F}\delta_{\mu,\nu}\delta_{q+k,0}. \tag{F.40}$$

Using this result, we can show that

$$\begin{aligned}\langle t_\mu(s)t_\nu(s)\rangle &= \frac{1}{L^2}\sum_{q,k}\exp(i(q+k)s)\langle \hat{t}_\mu(q)\hat{t}_\nu(k)\rangle \\ &= \frac{1}{L}\sum_q \frac{k_BT}{Aq^2+F}.\end{aligned} \tag{F.41}$$

The "order parameter"

$$z = \langle \hat{\boldsymbol{z}}\cdot\sum_i \boldsymbol{t}_i\rangle = L\langle t_z\rangle \approx L\left(1-\frac{1}{2}\langle t_x^2(s)\rangle - \frac{1}{2}\langle t_y^2(s)\rangle\right), \tag{F.42}$$

and therefore

$$\frac{z}{L} \approx 1 - \frac{1}{2\pi}\int_{-\infty}^{\infty} dq \frac{k_B T}{Aq^2 + F} = 1 - \frac{k_B T}{2\sqrt{FA}}. \tag{F.43}$$

Appendix G

Sadowsky Functional

In order to derive Sadowsky's result, we need now to express the geometrical quantities in (4.2) (i.e. the area form dA and the principal curvature κ_1) in terms of the centerline. To do this we can choose the following parameterization for the strip:

$$\boldsymbol{R}(s,t) = \boldsymbol{r}(s) + t\left[\boldsymbol{b}(s) + \frac{\tau(s)}{\kappa(s)}\,\boldsymbol{t}(s)\right], \tag{G.1}$$

where $\boldsymbol{r}$ represents the centerline, κ and τ are its curvature and torsion respectively, $\boldsymbol{t}$ and $\boldsymbol{b}$ are the tangent and binormal vectors respectively and $s \in [0, L]$ and $t \in \left[-\frac{w}{2}, \frac{w}{2}\right]$. Moreover we have that $\tau/\kappa = \cot\psi$, where ψ is the angle formed by the generator of this developable surface with the tangent direction. We recall here that $\boldsymbol{t} = \boldsymbol{r}'$ where the prime indicate the derivative with respect to s and that the vectors $\boldsymbol{t}$, $\boldsymbol{n}$ and $\boldsymbol{b}$ satisfy the following cross-product relations:

$$\boldsymbol{t} = \boldsymbol{n} \times \boldsymbol{b}, \qquad \boldsymbol{n} = \boldsymbol{b} \times \boldsymbol{t}, \qquad \boldsymbol{b} = \boldsymbol{t} \times \boldsymbol{n}, \tag{G.2}$$

as well as the Frenet-Serret formulas:

$$\boldsymbol{t}' = \kappa\boldsymbol{n}, \qquad \boldsymbol{n}' = -\kappa\boldsymbol{t} + \tau\boldsymbol{b}, \qquad \boldsymbol{b}' = -\tau\boldsymbol{n}. \tag{G.3}$$

Next, let us the tensors g_{ij} and b_{ij} of the first and second fundamental form of the surface. As a starting point we calculate the tangent vectors $\boldsymbol{g}_i = \partial_i \boldsymbol{R}$ associated with the coordinates s and t. Making use of (G.3), we have then:

$$\boldsymbol{g}_s = \boldsymbol{r}' + t\left[\frac{\tau'\kappa - \tau\kappa'}{\kappa^2}\,\boldsymbol{t} + \frac{\tau}{\kappa}\,\boldsymbol{t}' + \boldsymbol{b}'\right] = f(s,t)\,\boldsymbol{t}, \tag{G.4}$$

where we have called:

$$f(s,t) = 1 + \frac{\tau'\kappa - \tau\kappa'}{\kappa^2}\,t. \tag{G.5}$$

Analogously, we find that

$$\boldsymbol{g}_t = \boldsymbol{b} + \frac{\tau}{\kappa}\,\boldsymbol{t}. \tag{G.6}$$

Thus the coefficients of the tensor of the first fundamental form, $g_{ij} = \boldsymbol{g}_i \cdot \boldsymbol{g}_j$ are given by:

$$g_{ss} = f^2, \qquad g_{st} = \frac{\tau}{\kappa},\, f \qquad g_{tt} = 1 + \frac{\tau^2}{\kappa^2}, \tag{G.7}$$

from which the area form is immediately given by:

$$dA = \sqrt{g}\,ds\,dt = \sqrt{\det I}\,ds\,dt = f\,ds\,dt. \tag{G.8}$$

Next we show that the normal vector $\boldsymbol{N}$ of the strip coincides with the normal vector $\boldsymbol{n}$ of the centerline. Taking the cross-product between the two tangent vectors and using Eqs. (G.2) yields:

$$\boldsymbol{g}_t \times \boldsymbol{g}_s = \left(\boldsymbol{b} + \frac{\tau}{\kappa}\,\boldsymbol{t}\right) \times f\,\boldsymbol{t} = f\boldsymbol{b} \times \boldsymbol{t} = f\boldsymbol{n}. \tag{G.9}$$

Thus:

$$\boldsymbol{N} = \frac{\boldsymbol{g}_t \times \boldsymbol{g}_s}{|\boldsymbol{g}_t \times \boldsymbol{g}_s|} = \boldsymbol{n}. \tag{G.10}$$

With the normal vector in hand, we can now calculate the elements of the tensor of the second fundamental form $b_{ij} = -\boldsymbol{g}_i \cdot \partial_j \boldsymbol{N} = -\boldsymbol{g}_i \cdot \partial_j \boldsymbol{n}$. These are evidently:

$$b_{ss} = \kappa\, f, \qquad b_{st} = b_{tt} = 0. \tag{G.11}$$

It follows immediately that det $II = 0$ and $\kappa_G = \det\, II/\det\, I = 0$, as expected. Knowing g_{ij} and b_{ij} we can calculate the principal curvature κ_1:

$$\kappa_1 = 2H = g^{ij} b_{ij} = g^{ss} b_{ss} = \frac{\kappa}{f}\left(1 + \frac{\tau^2}{\kappa^2}\right). \tag{G.12}$$

Upon replacing κ_1 and dA in (4.2) we obtain:

$$\begin{aligned} E &= \frac{1}{2} D \int_0^L ds\, \kappa^2 \left(1 + \frac{\tau^2}{\kappa^2}\right)^2 \int_{-\frac{w}{2}}^{\frac{w}{2}} dt\, \frac{\kappa^2}{\kappa^2 + (\tau'\kappa - \tau\kappa')t} \\ &= \frac{1}{2} D \int_0^L ds\, \frac{(\kappa^2 + \tau^2)^2}{\tau'\kappa - \tau\kappa'} \log\left[\frac{\kappa^2 + \frac{w}{2}(\tau'\kappa - \tau\kappa')}{\kappa^2 - \frac{w}{2}(\tau'\kappa - \tau\kappa')}\right]. \end{aligned} \tag{G.13}$$

The latter is the expression found by Wunderlich for a generic developable strip [111]. Now, the term $w(\tau'\kappa - \tau\kappa')$ appearing in the logarithm has order of magnitude $(w/L)\kappa^2$ (assuming $\kappa \sim \tau$). Thus when $w/L \ll 1$, using $\log(x + \epsilon y) = \log x + \epsilon\, y/x + o(\epsilon^2)$, we find:

$$\log\left[\frac{\kappa^2 + \frac{w}{2}(\tau'\kappa - \tau\kappa')}{\kappa^2 - \frac{w}{2}(\tau'\kappa - \tau\kappa')}\right] \approx \frac{w(\tau'\kappa - \tau\kappa')}{\kappa^2}, \tag{G.14}$$

upon substituting in 4.3 gives finally the famous Sadowsky's result [85]:

$$E = \frac{1}{2} Dw \int_0^L ds\, \frac{(\kappa^2 + \tau^2)^2}{\kappa^2}. \tag{G.15}$$

Appendix H

Twist and Writhe

When we look at a closed circular DNA in some direction we can distinguish two possible types of crossings between its strands, as illustrated in Figure H.1 [50]. The twist crossings result from helical winding of one strand around the other. The writhe crossings are caused by self-intersections of the DNA axis. The total number of crossings of each type is even. The twist crossings (1) are formed by helical winding of one strand about the other. Twist is the rate of rotation of the ribbon around its axis, a local property of the ribbon while writhe is a measure of non-planarity of the ribbon's axis curve, a global property. Work by Călugăreanu, White and Brock Fuller led to the Călugăreanu-White-Fuller theorem that

$$Lk = Wr + Tw. \tag{H.1}$$

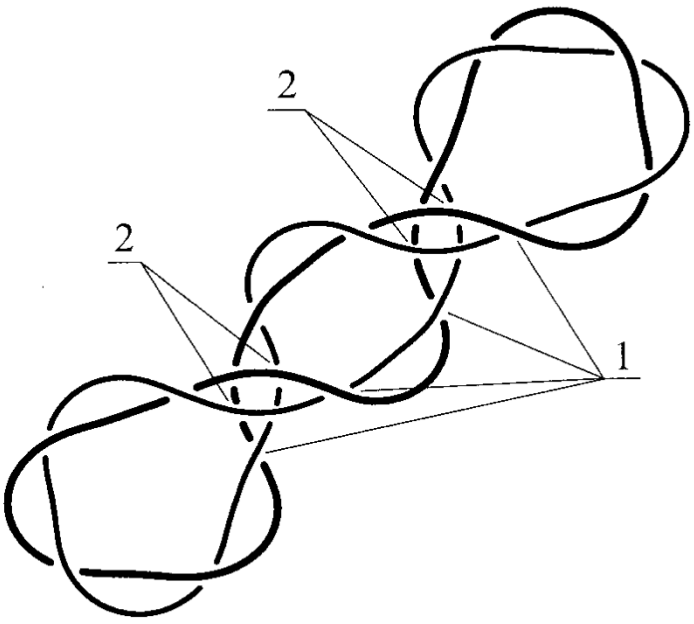

Figure H.1: Crossings of the strands in a two-dimensional projection of a closed circular DNA. The twist crossings (1) are formed by helical winding of one strand about the other. The writhe crossings (2) are caused by self-intersections of the DNA axis.

H.1 Twist

For example, let C be a right handed helix of constant radius R and pitch $2\pi P$ parameterized by

$$\boldsymbol{x}_C(s) = \{R\cos(s/\ell), R\sin(s/\ell), Ps/\ell\}, \tag{H.2}$$

where $\ell = \sqrt{(R^2 + P^2)}$ and $0 \leq s \leq L = 2\pi n\ell$. Let the curve A be a straight line given by

$$\boldsymbol{x}_A(s) = \{0, 0, Ps/\ell\}. \tag{H.3}$$

We adopt the correspondence $\boldsymbol{x}_A(s) \rightarrow \boldsymbol{x}_C(s)$ and hence the correspondence vector $\boldsymbol{z}_{AC}(s)$ is the difference of the two vectors given by

$$\boldsymbol{z}_{AC}(s) = \{R\cos(s/\ell), R\sin(s/\ell), 0\}. \tag{H.4}$$

Since $\boldsymbol{z}_{AC}(s)$ is perpendicular to the curve A, we find that

$$\boldsymbol{v}_{AC}(s) = \{\cos(s/\ell), \sin(s/\ell), 0\}. \tag{H.5}$$

From this, a straightforward calculation reveals that the twist of C about A is

$$Tw(C, A) = n. \tag{H.6}$$

A similar calculation shows that the twist of A about C is

$$Tw(C, A) = \frac{nP}{\ell}. \tag{H.7}$$

A diagrammatic illustration of the importance of the ordering in the calculation of twist is presented in H.2.

H.2 Numerical implementation of Writhe

The writhe of a discrete curve is given by

$$Wr = \frac{1}{2\pi} \sum_{i=2}^{N-1} \sum_{j<i} \Omega_{ij} \tag{H.8}$$

where Ω_{ij} is the Gauss integral along the segments $a\boldsymbol{t}_i$, $a\boldsymbol{t}_j$

The Gauss integral can be calculated using a geometrical approach. Let points 1 and 2 be the front and end of the first segment $\boldsymbol{r}_{12} = a\boldsymbol{t}_i$ and points 3 and 4 be the start and end of the second segment $\boldsymbol{r}_{34} = a\boldsymbol{t}_j$ respectively. The magnitude of Ω_{ij} is the solid angle formed by all those view directions in which the vectors $\boldsymbol{r}_{12}$ and $\boldsymbol{r}_{34}$ apparently cross. It can be shown that $|\Omega_{ij}|$ is given by the area of the quadrangle on a unit sphere with the apexes formed by the intersections of the sphere with the

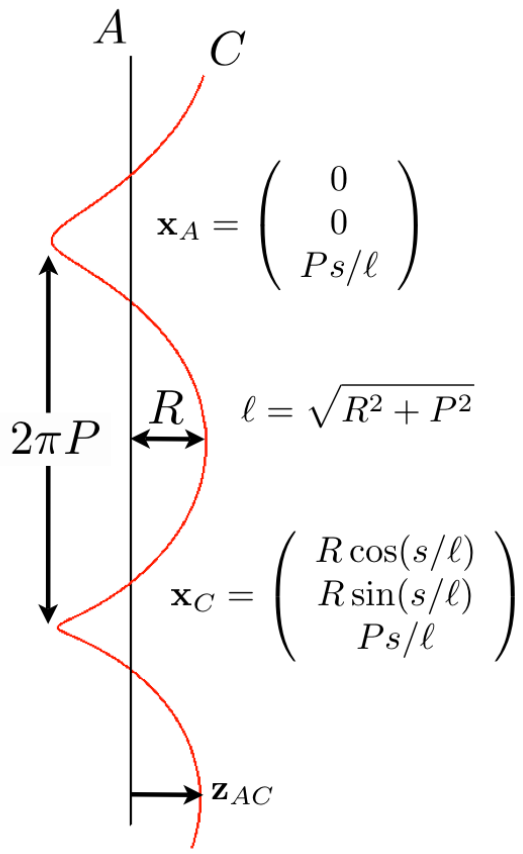

Figure H.2: Curve A is a straight line and curve C is a right-handed circular helix of radius R and pitch $2\pi P$. The correspondence vector $\boldsymbol{z}_{AC}$ is directed as shown from the straight axis to the helix. In this case, $Tw(C, A) = n$ while $Tw(A, C) = nP/\ell$ where $\ell = \sqrt{R^2 + P^2}$, so the two quantities are different.

rays originating at the center of the sphere and parallel to the lines (31), (41), (42), and (32) [50]. The area of the quadrangle on a unit sphere is

$$|\Omega_{ij}| = \alpha_1 + \alpha_2 + \alpha_3 + \alpha_4 - 2\pi, \tag{H.9}$$

where $\alpha_1, .., \alpha_4$ are the angles of the quadrangle. Let

$$\boldsymbol{n}_1 = \frac{\boldsymbol{r}_{13} \times \boldsymbol{r}_{14}}{|\boldsymbol{r}_{13} \times \boldsymbol{r}_{14}|}, \quad \boldsymbol{n}_2 = \frac{\boldsymbol{r}_{14} \times \boldsymbol{r}_{24}}{|\boldsymbol{r}_{14} \times \boldsymbol{r}_{24}|}, \tag{H.10}$$

$$\boldsymbol{n}_3 = \frac{\boldsymbol{r}_{24} \times \boldsymbol{r}_{23}}{|\boldsymbol{r}_{24} \times \boldsymbol{r}_{23}|}, \quad \boldsymbol{n}_4 = \frac{\boldsymbol{r}_{23} \times \boldsymbol{r}_{13}}{|\boldsymbol{r}_{23} \times \boldsymbol{r}_{13}|}, \tag{H.11}$$

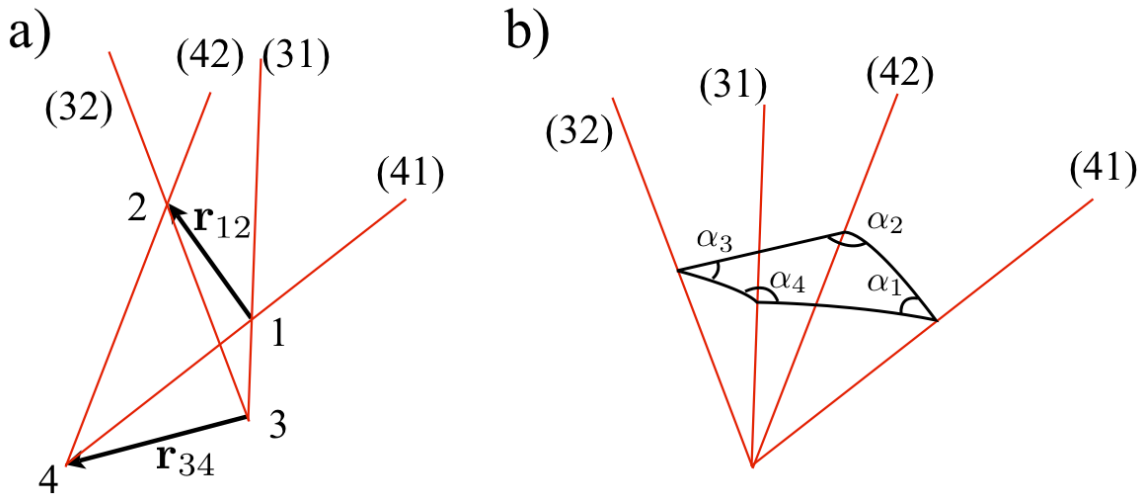

Figure H.3: a) Points 1 and 2 are the front and end of the first segment $\boldsymbol{r}_i$ and points 3 and 4 are the start and end of the second segment $\boldsymbol{r}_j$ respectively. We can draw four line segments (32), (42), (31), and (41). b) $|\Omega_{ij}|$ is the solid angle on a unit sphere bounded by the four planes: (134), (124), (234), and (123).

be the four unit vectors normal to the planes bounding the solid angle $|\Omega_{ij}|$. For example, $\boldsymbol{n}_1$ is normal to the plane (134), $\boldsymbol{n}_2$ is normal to the plane (124) and so on. Taking into account of their orientation, we find that

$$\alpha_1 = \arccos(-\boldsymbol{n}_1 \cdot \boldsymbol{n}_2) = \frac{\pi}{2} + \arcsin(\boldsymbol{n}_1 \cdot \boldsymbol{n}_2). \tag{H.12}$$

Similar relations hold for α_2, α_3, and α_4. Putting everything together, we find that

$$|\Omega_{ij}| = \arcsin(\boldsymbol{n}_1 \cdot \boldsymbol{n}_2) + \arcsin(\boldsymbol{n}_2 \cdot \boldsymbol{n}_3) + \arcsin(\boldsymbol{n}_3 \cdot \boldsymbol{n}_4) + \arcsin(\boldsymbol{n}_4 \cdot \boldsymbol{n}_1). \tag{H.13}$$

The sign of Ω_{ij} can be found in the following way: Ω_{ij} is positive if the two segment $\boldsymbol{r}_i$ and $\boldsymbol{r}_j$ form a right-handed crossing and negative otherwise. Hence, in all, the Gauss integral

$$\Omega_{ij} = |\Omega_{ij}| \operatorname{sign}((\boldsymbol{r}_j \times \boldsymbol{r}_i) \cdot \boldsymbol{r}_{13}) \tag{H.14}$$

Bibliography

[1] M. Abkarian, A. Subramaniam, S. H. Kim, R. Larsen, S. M. Yang, and H. Stone. Dissolution Arrest and Stability of Particle-Covered Bubbles. *Phys. Rev. Lett.*, 99(18):188301, October 2007.

[2] S. S. Antman and G. Rosenfeld. Global behavior of buckled states of nonlinearly elastic rods. *SIAM*, 20(3):513–566, 1978.

[3] Stuart S Antman and John F Pierce. The intricate global structure of bucked states of compressible columns. *SIAM*, 50(2):395–419, 1990.

[4] T. Bauer, S. Little, A. G. Stver, and A. Driks. Functional regions of the bacillus subtilis spore coat morphogenetic protein cote. *J. Bacteriol.*, 181:7043–7051, 1999.

[5] H. Berg. *Random Walks in Biology.* Princeton University Press, NJ, 1983.

[6] C. Bouchiat and M. Mézard. Elasticity model of a supercoiled dna molecule. *PRL*, 80(7):1556–1559, 1998.

[7] M. Bowick, A. Cacciuto, D. R. Nelson, and A. Travesset. Crystalline order on a sphere and the generalized thomson problem. *Phys. Rev. Lett.*, 89(18):185502, Oct 2002.

[8] Mark J. Bowick, Angelo Cacciuto, David R. Nelson, and Alex Travesset. Crystalline particle packings on a sphere with long-range power-law potentials. *Phys. Rev. B*, 73(2):024115, Jan 2006.

[9] Mark J. Bowick, David R. Nelson, and Homin Shin. Interstitial fractionalization and spherical crystallography. *Phys. Chem. Chem. Phys.*, 9:6304–6312, 2007.

[10] Mark J. Bowick, David R. Nelson, and Alex Travesset. Interacting topological defects on frozen topographies. *Phys. Rev. B*, 62(13):8738–8751, Oct 2000.

[11] D. E. Bradley and J. G. Franklin. Electron microscope survey of the surface configuration of spores of the genus bacillus. *J Bacteriol*, 76:618–630, 1958.

[12] D. E. Bradley and D. J. Williams. An electron microscope study of the spores of some species of the genus bacillus using carbon replicas. *J. Gen. Microbiol.*, 17:75–79, 1957.

[13] K. Brakke. The surface evolver. *Exp. Math.*, 1:141–145, 1992.

[14] F.H. Busse. Patterns of convection in spherical shells. *J.Fluid Mech.*, 72(1):67–85, 1975.

[15] Carlos Bustamant, Zev Bryant, and Steven B. Smith. Ten years of tension: single-molecule dna mechanic. *Nature*, 421:423–426, 2003.

[16] C. J. Bustamante, J. F. Marko, E. D. Siggia, and S. Smith. *Science*, 265:1599–1600, 1994.

[17] D. L. Casper and A. Klug. Physical principles in the construction of regular viruses. *Cold Spring Harb Symp Quant. Bio.*, 27:1–24, 1962.

[18] E. Cerda and L. Mahadevan. Geometry and physics of wrinkling. *prl*, 90:074302, 2003.

[19] V. G. Chada, Sanstad, E. A., R. Wang, and A. Driks. Morphogenesis of bacillus spore surfaces. *J. Bacteriol.*, 185:6255–6261, 2003.

[20] P. M. Chaikin and T. C. Lubensky. *Principles of condensed matter physics*. Cambridge University Press, Cambridge, 2003.

[21] Tanya L. Chantawansri, August W. Bosse, Alexander Hexemer, Hector D. Ceniceros, Carlos J. García-Cervera, Edward J. Kramer, and Glenn H. Fredrickson. Self-consistent field theory simulations of block copolymer assembly on a sphere. *Phys. Rev. E*, 75(3):031802, Mar 2007.

[22] G. Chen, A. Driks, K. Tawfiq, M. Mallozzi, and S. Patil. Bacillus anthracis and bacillus subtilis spore surface properties as analyzed by transport analysis. *Colloids and Surfaces B: Biointerfaces*, 76:512–518, 2010.

[23] John David Crawford. Introduction to bifurcation theory. *Reviews of Modern Physics*, 63:991–1037, 1991.

[24] M. R. Dennis and J. H. Hannay. Geometry of călugăreanus theorem. *Proc. R. Soc. A*, 461:3245–3254, 2005.

[25] A. Driks. The dynamic spore. *pnas*, 100:3007–3009, 2003.

[26] A. Driks and M. Mallozzi. *Bacillus anthracis and Anthrax*. John Wiley & Sons, 2009.

[27] Adam Driks. Bacillus subtilis spore coat. *Microbiology and Molecular Biology Reviews*, 63(1):1–20, Mar 1999.

[28] R. Elbaum, S. Gorb, and P. Fratzl. Structures in the cell wall that enable hygroscopic movement of wheat awns. *Journal of Structural Biology*, 164:101–107, 2008.

[29] D. McPherson et al. Characterization of the bacillus subtilis spore coat morphogenetic protein coto. *J. Bacteriol.*, 187:8278–8290, 2005.

[30] H. Kim et al. The bacillus subtilis spore coat protein interaction network. *Mol. Microbiol*, 59:487–502, 2006.

[31] S. Ghosh et al. Characterization of spores of bacillus subtilis that lack most coat layers. *J. Bacteriol.*, 190:6741–6748, 2008.

[32] R. Everaers, R. Bundschuh, and K. Kremer. *Europhys. Lett.*, 29:263, 1995.

[33] B. Fain, J. Rudnick, and S. Östlund. Conformations of linear dna. *Phys. Rev. E*, 55:7364–7368, 1997.

[34] P. J. FLory. *Principles of Polymer Chemistry*. Cornell University Press, Ithaca, NY, 1953.

[35] F. B. Fuller. The writhing number of a space curve. *PNAS*, 68:815–819, 1971.

[36] F. B. Fuller. Decomposition of the linking number of a closed ribbon: A problem from molecular biology. *PNAS*, 75(8):3557–3561, 1978.

[37] L. Giomi and L. Mahadevan. Statistical mechanics of developable ribbons. *PRL*, 104:238104, 2010.

[38] Luca Giomi and Mark Bowick. Crystalline order on riemannian manifolds with variable gaussian curvature and boundary. *Phys. Rev. B*, 76(5):054106, Aug 2007.

[39] R. Golestanian and T.B. Liverpool. Statistical mechanics of semiflexible ribbon polymers. *Phys. Rev. E*, 62(4):5488–5499, 2000.

[40] M Golubitsky and D G Schaeffer. *Singularities and Groups in Bifurcation Theory*, volume 1. Springer-Verlag, New York, 1985.

[41] M. Golubitsky and D. G. Schaeffer. *Singularities and Groups in Bifurcation Theory Vol 1*. Springer-Verlag, 1985.

[42] S. Goshen, D. Mukamel, and S. Shtrikman. Application of the landau theory of phase transitions to liquids-liquid crystals transitions. *Solid State Communications*, 9(10):649 – 652, 1971.

[43] A. O. Henriques and C. P Moran. Structure, assembly and function of the spore surface layers. *Ann. Rev. Microbiol.*, 61:555–588, 2007.

[44] S. C. Holt and E. R. Leadbetter. Comparative ultrastructure of selected aerobic spore-forming bacteria: a freeze-etching study. *Bacteriol. Rev.*, 33:346–378, 1969.

[45] B. Hopkinson and G. T. Williams. The Elastic Hysteresis of Steel. *Royal Society of London Proceedings Series A*, 87:502–511, December 1912.

[46] J. W. Hutchinson. Imperfection sensitivity of externally pressurized spherical shells. *Journal of Applied Mechanics*, pages 49–55, March 1967.

[47] E. Katifori, S. Alben, E. Cerda, D. R. Nelson, and J. Dumials. Foldable structures and the natural design of pollen grains. *PNAS*, 107(17):7635–7639, 2010.

[48] Eleni Katifori. *Vortices, rings and pollen grains: Elasticity and statistical physics in soft matter*. PhD thesis, Harvard University, 2008.

[49] James P. Keener. *Principles of Applied Mathematics*. Westview Press, Cambridge, MA, USA, 1999.

[50] K. Klenin and J. Langowski. Computation of writhe in modeling of supercoiled dna. *Biopolymers*, 54:307–317, 2000.

[51] Tamotsu Kohyama and Gerhard Gompper. Defect scars on flexible surfaces with crystalline order. *Phys. Rev. Lett.*, 98(19):198101, May 2007.

[52] J. M. Kolinski, P. Aussillous, and L. Mahadevan. Shape and motion of a ruck in a rug. *prl*, 103:174302, 2009.

[53] Yuri A. Kuznetsov. *Elements of Applied Bifurcation Theory*. Springer-Verlag, New York, 3 edition, 2004.

[54] L. D. Landau, L. P. Pitaevskii, E. M. Lifshitz, and A. M. Kosevich. *Theory of elasticity*. Pergamon, NY, 3rd edition, 1986.

[55] J. Lidmar, L. Mirny, and D. R. Nelson. Virus shapes and buckling transitions in spherical shells. *Phys. Rev. E*, 68(5), November 2003.

[56] S. Little and A. Driks. Functional analysis of the bacillus subtilis morphogenetic spore coat protein cote. *Mol. Microbiol.*, 42:1107–1120, 2001.

[57] T.B. Liverpool, R. Golestanian, and K. Kremer. Statistical mechanics of double-stranded semiflexible polymers. *Phys. Rev. Lett.*, 80(2):405–408, 1998.

[58] A. E. H. Love. *A Treatise on the Mathematical Theory of Elasticity*. Dover, New York, 4th edition, 1944.

[59] A. V. Lukashin M. D. Frank-Kamenetskii and A. V. Vologodskii. *Nature*, 258:398–402, 1975.

[60] A. Magnusson, M. Ristinmaa, and C. Ljung. Behaviour of the extensible elastica solution. *Int. J. Solids and Structures*, 38:8441–8457, 2001.

[61] E. H. Mansfield. *The bending and stretching of plates*. Cambridge University Press, Cambridge, UK, 2nd edition, 1989.

[62] J. F. Marko. Torque and dynamics of linking number relaxation in stretched supercoiled dna. *Phys. Rev. E*, 76:021926, 2007.

[63] J. F. Marko and E. D. Siggia. *Macromolecules*, 28:8759–8770, 1995.

[64] J. F. Marko and E. D. Siggia. *Phys. Rev. E*, 52(3):2912–2938, 1995.

[65] J. F. Marko and A. Vologodskii. Extension of torsionally stressed dna by external force. *Biophys. J.*, 73:123–132, 1997.

[66] M. U. Mera and T. J. Beveridge. Mechanism of silicate binding to the bacterial cell wall in bacillus subtilis. *J. Bacteriol.*, 175:1936–1945, 1993.

[67] Albert Messiah. *Quantum Mechanics*. Dover Publications, New York, 1962.

[68] J. D. Moroz and P. Nelson. Torsional directed walks, entropic elasticity, and dna twist stiffness. *PNAS*, 94:14418–14422, 1997.

[69] J. D. Moroz and P. Nelson. Entropic elasticity of twist-storing polymers. *Macromolecules*, 31(18):6333–6347, 1998.

[70] D. R. Nelson. *Defects and geometry in condensed matter physics*. Cambridge University Press, Cambridge, 2002.

[71] D. R. Nelson, T. Piran, and S. Weinberg. *Statistical mehanics of membranes and surfaces*. World-Scientific, Singapore, 2nd edition, 2004.

[72] David R. Nelson and John Toner. Bond-orientational order, dislocation loops, and melting of solids and smectic-*a* liquid crystals. *Phys. Rev. B*, 24:363–387, Jul 1981.

[73] P. Nelson. *Biological Physics*. W. H. Freeman, NY, 2004.

[74] S. Neukirch. Extracting dna twist rigidity from experimental supercoiling data. *PRL*, 93(19):198107, 2004.

[75] S. Neukirch and E. L. Starostin. Writhe formulas and antipodal points in plectonemic dna configurations. *Phys. Rev. E*, 78:041912, 2008.

[76] Alan C. Newell, Patrick D. Shipman, and Zhiying Sun. Phyllotaxis: Cooperation and competition between mechanical and biochemical processes. *Journal of Theoretical Biology*, 251(3):421 – 439, 2008.

[77] Susumu Onaka. Simple equations giving shapes of various convex polyhedra: the regular polyhedra and polyhedra composed of crystallographically low-index planes. *Philosophical Magazine Letters*, 86(3):175–183, March 2006.

[78] H. Pleiner. Shape deformations of spherical vesicles under radial pressure. *Phys. Rev. A*, 42(10):6060–6067, November 2009.

[79] M. Plomp, T. Leighton, K. E. Wheeler, and A. J. Malkin. The high-resolution architecture and structural dynamics of bacillus spores. *Biophys. J.*, 88:603–608, 2004.

[80] M. Plomp, T. J. Leighton, K. E. Wheeler, M. E. Pitesky, and A. J. Malkin. Bacillus atrophaeus outer spore coat assembly and ultrastructure. *Langmuir*, 21:10710–10716, 2005.

[81] C. Quilliet, C. Zoldesi, C. Riera, A. van Blaaderen, and A. Imhof. Anisotropic colloids through non-trivial buckling. *The European Physical Journal E: Soft Matter and Biological Physics*, 27:13–20, 2008.

[82] C. Quilliet, C. Zoldesi, C. Riera, A. van Blaaderen, and A. Imhof. Anisotropic colloids through non-trivial buckling. *Euro. J. Phys.*, 27(1), 2009.

[83] J. R. Quine, T. A. Cross, M. S. Chapman, and R. Bertram. *Bull. Math. Biol.*, 66:1705–1730, 2004.

[84] V. Reddy, P. Natarajan, B. Okerberg, K. Li, K. Damodaran, M. K. Brooks, and J. Johnson. Virus particle explorer (viper), a website for virus capsid structures and their computational analyses. *J. Virol.*, 75:11943, 2001.

[85] M. Sadowsky. *Sitzungsber. Preuss. Akad. Wiss. Phys. Math. Kl.*, 22:412, 1930.

[86] L. Y. Santo and R. H. Doi. Ultrastructural analysis during germination and outgrowth of bacillus subtilis spores. *J. Bacteriol.*, 120:475–481, 1974.

[87] D. H. Sattinger. Bifurcation from rotationally invariant states. *J. Math. Phys.*, 19:1720, 1978.

[88] James P. Sethna, Karin Dahmen, Sivan Kartha, James A. Krumhansl, Bruce W. Roberts, and Joel D. Shore. Hysteresis and hierarchies: Dynamics of disorder-driven first-order phase transformations. *prl*, 70(21):3347–3350, May 1993.

[89] P. Setlow. Spore germination. *Curr. Opin. Microbiol.*, 6:550–556, 2003.

[90] H. S. Seung and David R. Nelson. Defects in flexible membranes with crystalline order. *Phys. Rev. A*, 38(2):1005–1018, Jul 1988.

[91] P. D. Shipman and A. C. Newell. Phyllotactic patterns on plants. *Phys. Rev. Lett.*, 92(16):168102, Apr 2004.

[92] Patrick Daniel Shipman. *Plant Patterns*. PhD thesis, University of Arizona, 2004.

[93] A. Šiber. Buckling transition in icosahedral shells subjected to volume conservation constraint and pressure: Relations to virus maturation. *Phys. Rev. E*, 73(6), June 2006.

[94] E. L. Starostin and G. H. M. van der Heijden. Tension-induced multistability in inextensible helical ribbons. *PRL*, 101:084301, 2008.

[95] Paul J. Steinhardt, David R. Nelson, and Marco Ronchetti. Bond-orientational order in liquids and glasses. *Phys. Rev. B*, 28(2):784–805, Jul 1983.

[96] T. R. Strick, J.-F. Allemand, D. Bensimon, A. Bensimon, and V. Croquette. The elasticity of a single supercoiled dna molecule. *Science*, 271:1835–1837, 1996.

[97] T. R. Strick, J.-F. Allemand, D. Bensimon, and V. Croquette. Behavior of supercoiled dna. *Biophys. J.*, 74:2016–2028, 1998.

[98] Bjorn A. Traaga, Adam Driks, Patrick Stragierc, Wilbert Bitterd, Gregory Broussarde, Graham Hatfulle, Frances Chuf, Kristin N. Adamsf, Lalita Ramakrishnanf, and Richard Losicka. Do mycobacteria produce endospores? *pnas*, 107:878–881, 2010.

[99] N. Tsapis, E. R. Dufresne, S. S. Sinha, C. S. Riera, J. W. Hutchinson, L. Mahadevan, and D. A. Weitz. Onset of buckling in drying droplets of colloidal suspensions. *prl*, 94:018302, 2005.

[100] A. Vaziri and L. Mahadevan. Localized and extended deformations of elastic shells. *PNAS*, 105(23):913–7918, Jun 2008.

[101] A. V. Vologodskii. Dna extension under the action of an external force. *Macromolecules*, 27:5623–5625, 1994.

[102] A. V. Vologodskii, V. V. Anshelevich, A. V. Lukashin, and M. D. Frank-Kamenetskii. *Nature*, 280:294–298, 1979.

[103] R. H. Vreeland, W. D. Rosenzweig, and D. W. Powers. Isolation of a 250 million-year-old halotolerant bacterium from a primary salt crystal. *Nature*, 407:897–900, 2000.

[104] Rong Wang, Soumya N. Krishnamurthy, Jae-Sun Jeong, Adam Driks, Manav Mehta, and Bruce A. Gingras. Fingerprinting species and strains of bacilli spores by distinctive coat surface morphology. *Langmuir*, 23(20):10230–10234, 2007.

[105] A. J. Westphal, P. B. Price, T. J. Leighton, and K. E. Wheeler. Kinetics of size changes of individual bacillus thuringiensis spores in response to changes in relative humidity. *pnas*, 100:3461–3466, 2003.

[106] J. H. White. Self-linking and the gauss integral in higher dimensions. *Amer. J. Math.*, 91:693–728, 1969.

[107] J. H. White and W. R. Bauer. Calculation of the twist and the writhe for representative models of dna. *J. Mol. Biol.*, 189:329–341, 1986.

[108] J. H. White and W. R. Bauer. Applications of the twist difference to dna structural analysis. *PNAS*, 85:772–776, 1988.

[109] M. Widom, J. Lidmar, and D. R. Nelson. Soft modes near the buckling transition of icosahedral shells. *Phys. Rev. E*, 76(3), September 2007.

[110] T. Witten. Stress focusing in elastic sheets. *Rev. Mod. Phys.*, 79(2):643–675, April 2007.

[111] W. Wunderlich. *Monatsh. Math.*, 66:276, 1962.

[112] M. Yanagisawa, M. Imai, and T. Taniguchi. Shape Deformation of Ternary Vesicles Coupled with Phase Separation. *Phys. Rev. Lett.*, 100(14), April 2008.

[113] Zheng Yang, I. Bahar, and Michael Widom. Vibrational dynamics of icosahedrally symmetric biomolecular assemblies compared with predictions based on continuum elasticity. *Biophysical journal*, 96(11):4438–4448, Jun 2009.

[114] L. Zhang and A. Eisenberg. Multiple morphologies of "crew-cut" aggregates of polystyrene-b-poly(acrylic acid) block copolymers. *Science*, 268:1728, 1995.

[115] L. Zheng, W. P. Donovan, P. C. Fitz-James, and R. Losick. Gene encoding a morphogenic protein required in the assembly of the outer coat of the bacillus subtilis endospore. *Genes Dev.*, 2:1047–1054, 1988.

[116] C. I. Zoldesi and A. Imhof. Synthesis of Monodisperse Colloidal Spheres, Capsules, and Microballoons by Emulsion Templating. *Advanced Materials*, 17(7):924–928, April 2005.

[117] C. I. Zoldesi, C. A. van Walree, and A. Imhof. Deformable Hollow Hybrid Silica/Siloxane Colloids by Emulsion Templating. *Langmuir*, 22(9):4343–4352, April 2006.